NORTHWESTERN UNIVERSITY

Metal/Ceramic Composites via Infiltration of an Interconnected Wood-Derived Ceramic

A DISSERTATION

SUBMITTED TO THE GRADUATE SCHOOL
IN PARTIAL FULFILLMENT OF THE REQUIREMENTS

for the degree

DOCTOR OF PHILOSOPHY

Field of Materials Science and Engineering

By

Thomas E. Wilkes

EVANSTON, ILLINOIS

June 2008

Abstract

Metal/Ceramic Composites via Infiltration of an Interconnected Wood-Derived Ceramic

Thomas E. Wilkes

The use of composites is increasing as they afford scientists and engineers the ability to combine the advantageous properties of each constituent phase, e.g. metal ductility and ceramic stiffness. With respect to materials design, biomimetics is garnering increasing attention due to the complex, yet efficient, natural microstructures. One such biomimetic, or in this case 'bio-derived,' curiosity is wood-derived ceramic, which is made by either replicating or converting wood into a ceramic. The resulting porous and anisotropic material retains the precursor microstructure. The wide variety of precursors can yield materials with a range of pore sizes and distribution of pores.

The purpose of this work was to study the processing, microstructure, and properties of aluminum/silicon carbide composites. The composites were made by infiltrating molten aluminum into porous wood-derived SiC, which was produced by the reactive melt-infiltration of silicon into pyrolyzed wood. The composite microstructure consisted of interconnected SiC surrounding Al-alloy 'fibers.' The strength, modulus, and toughness were measured in both longitudinal and transverse orientations. The Al → SiC load transfer was investigated with high-energy X-ray diffraction in combination with *in-situ* compressive loading. The properties in flexure were found to decrease with increasing temperature. Despite the complex microstructure, predictions of the composite flexural modulus and longitudinal fracture toughness were obtained using simple models: Halpin-

Tsai bounds and the Ashby *et al.* model of the effect of ductile particle-reinforcements on the toughness of brittle materials (Ashby *et al.* 1989), respectively.

In addition, the Al/SiC research inspired the investigation of carbon-reinforced copper composites. The goal was to explore the feasibility of making a high-thermal conductivity composite by infiltrating copper into wood-derived carbon. Results indicated that Cu/C composites could be made with pressurized infiltration, but the predicted thermal conductivity was low due to the amorphous wood-derived carbon.

Approved by:

_____

Professor Katherine T. Faber
Department of Materials Science and Engineering
Robert R. McCormick School of Engineering and Applied Science
Northwestern University
Evanston, Illinois

June 2008

Acknowledgments

First, I would like to thank my advisor, Prof. Katherine T. Faber for her guidance and support, without which the past five years would have instead been ten. Likewise, thanks are also due to my other committee members: Profs. David C. Dunand, Thomas O. Mason and Richard M. Lueptow. Our conversations and your suggestions have been immensely helpful throughout my graduate student career. I am also grateful for the financial support from the Department of Defense through a National Defense Science and Engineering Graduate Fellowship, Northwestern University's Walter P. Murphy Fellowship and the National Science Foundation through grants DMR-0244258 and DMR-0710630.

Many aspects of this work were completed with the help of others, and I thank you all for your collaboration: Marcus Young and John DeFouw of the Dunand Research Group (many hours of help with the melt-infiltration equipment and letting me use the furnaces in the first place), Bryan Harder (APS beam-time and analyzing the data we collected), Bryan and Marcus (many helpful conversations that made sense of the load partitioning results), Marko (mechanical tester extraordinaire), Ranier Sepúlveda (mechanical tests in Evanston and microscopy in Sevilla), Dr. Kathleen A. Stair (sample preparation and microscopy), Prof. Stuart R. Stock (X-ray μCT beam time, data reconstruction and analysis), James Wilson (μCT image segmentation and IDL reconstruction), Profs. Javier Llorca and Ygnacio Pastor (helping with hundreds of mechanical tests over 7 great weeks in España), Prototype Casting Inc. for the A356, and Peggy Adamson for ensuring that I handed in the right forms at the right time to actually reach this point.

To the members of the Faber Research Group past and present (Chris Weyant, Vikram Kaul, Kristen Pappacena, Bryan Harder, Michelle Seitz, Harold Hsiung, Noah Shanti, Zun Chen, and Matt Johnson): thank you for your research suggestions, sitting through countless group meetings and practice talks, movie nights, and good times in Evanston, Indianapolis, Baltimore, Cincinnati and Detroit. I would also like to thank my friends both near and far, but in particular: Christina Freyman for both the science and non-science related conversations and, of course, surgery day; and Kristen Meldi for the countless conversations that were, and always will be, a welcome distraction from everyday life.

Finally and most importantly, to my parents, brother, and the rest of my family: it is because of you that I was able to reach this point. Your love, support and guidance have had the most profound influence on my life, and I am forever indebted to you all. I can only hope that this dissertation, which I dedicate to you, makes you proud.

tew

Laziness is not an option.

- K.T.F.

Table of Contents

List of Figures

List of Tables

1. Introduction

1.1. Motivation

As the performance demands of advanced materials increase, scientists and engineers are tasked with devising new materials and processing methods that result in improved material properties. All the while, increasing concerns regarding energy efficiency and material and production costs act to limit the viable options. One technique, combining two or more materials into a composite, is now main-stream and becoming more common in both high- and low-tech applications such as commercial aircraft fuselages (Hunt *et al.* 2005) and pipelines (Beckwith *et al.* 2006). Composite materials afford materials designers the ability to tailor properties by choosing the appropriate morphology, volume fraction, and orientation of each constituent (Clyne *et al.* 1993).

Research focused on man-made composites increased in the 1950s and 60s, although composites such as concrete and carbon-reinforced rubber had long been in use (Rodriguez 1996; Scala 1996). Low-weight/high-modulus materials were in demand not only for the aerospace industry but also for electronics and sports applications. This drove researchers to define and investigate "heterophase materials" and draw links between their microstructures and physical properties (Holliday 1963). Advances in processing methods themselves have also been made. Procedures once thought to be impossible, such as the infiltration of a ceramic preform with a molten metal (White *et al.* 1962), are now used in mass production processes (Chawla 1998).

As demand for advanced materials continues to grow, nature is becoming a source of inspiration for researchers striving to create efficient and effective microstructures.

Natural composite materials, such as bone, sea shells and wood, have developed into complex microstructures that, considering their relatively simple constituent materials, exhibit extraordinary mechanical behavior (Dinwoodie 1989; Heuer *et al.* 1992). The use of biomimetic materials is wide-ranging; for example, a man-made material, such as a porous nickel-titanium bone implant (Greiner *et al.* 2005), can be joined with the natural bone material. Biomimicry can also be used to engineer a material for purposes unrelated to the natural counterpart (Bond *et al.* 1995). For example, the unique cross-lamellar calcium carbonate microstructure of sea shells, which results in enhanced toughness and flaw tolerance, has been formed using mullite (Kaul *et al.* 2005), a material used at high-temperatures because of its retained strength and creep resistance.

The spotlight of advanced biomimetic and bio-derived materials research has only recently shone on the structure of wood (Ota *et al.* 1995; Byrne *et al.* 1997a; Greil 2001). Since the mid-1990s, wood-derived ceramic materials have gained considerable interest due to the wide variety of possible microstructures and ceramic materials that can be created. Also, the processing procedures are relatively energy-efficient when compared to traditional ceramic sintering processes and it is possible to produce near-net-shape parts. The porous ceramic materials have been considered for use in a wide range of applications including catalyst supports, heat exchangers, light-weight structural supports and the reinforcement phase in composite materials (de Arellano-López *et al.* 2004; Sieber 2005).

1.2. Objectives

Research concerning wood-derived porous ceramics is now relatively abundant; however, their application as a composite reinforcement and investigations of the composite processing-microstructure-property relationships are limited. Previous studies of wood-derived composite materials have been confined to studies of silicon/silicon carbide ceramic-matrix composites (Qiao *et al.* 2002; Presas *et al.* 2005).

The objective of this thesis was to expand upon these limited studies and to study the use of wood-derived ceramics in metal/ceramic composites (MCCs). To this end, the processing, microstructure, and properties of aluminum/silicon carbide (Al/SiC) composites were investigated. Processing techniques were developed to incorporate the aluminum and porous SiC, and the microstructures of the materials at various processing stages were studied with microscopy and other analytical techniques. The properties of the Al/SiC MCCs were studied in compression and bending at both room- and elevated-temperatures. The Al/SiC study also inspired inquiry into another composite system: carbon-reinforced copper. The feasibility of incorporating wood-derived carbon and copper was investigated through wetting and infiltration experiments, and microscopy was used to characterize the resulting microstructures.

1.3. Thesis Organization

The second chapter discusses the background material relevant to the research. Information concerning composites, three-dimensional ceramic materials, wood, and carbon is described along with a summary of the current state of wood-derived ceramic

research. The focus of the third and fourth chapters is the Al/SiC composites. Chapter three gives an account of the composite processing procedures and the microstructure of the wood, carbon, SiC and composites. Chapter four presents the experimental methods and resulting measurements of the mechanical properties of the composites. The processing and results of the Cu/C experiments are detailed in the fifth chapter, and the last chapter summarizes the thesis and gives suggestions for future work.

2. Background

This chapter discusses definitions, concepts and techniques that will aid in the understanding of the experimental methods and results in the remaining chapters of the thesis. The two main themes of the thesis, composites and wood, are discussed in detail. After defining a composite material, information about common morphologies, classifications and processing techniques are discussed. This segues into background information about the processing of porous ceramic preforms, the structure of wood and how wood is processed into ceramic materials.

2.1. Composites

2.1.1. Introduction

In general, man-made composites are considered materials composed of two or more physically and/or chemically distinct phases, and they have properties not demonstrated by the isolated constituents (Chawla 1998). A commonly-referenced composite material is adobe brick, which consists of clay reinforced with straw. By including the straw, the bricks can be more-effectively dried and cracks are more evenly distributed; both of which strengthen the material. Concrete is another common composite and, in its basic form, consists of a mixture of cement and aggregates. The cement acts as a binder while the aggregates, typically coarse stone, act to carry compressive loads. Both of these are examples of composite materials that have been used for centuries: adobe dates back to at least 800 BCE, and concrete was used by both the Greeks and Romans dating back to about 100 to 800 BCE. In addition to adobe and concrete, more recent examples of composite

materials include linoleum (linseed oil, wood dust, burlap) and rubber reinforced with carbon black, which strengthens the material (Holliday 1966).

2.1.2. Morphology

The properties of composite materials are affected by not only the properties of the individual components but also by the composite microstructure. In their modern embodiment, composite materials are typically categorized according to either the matrix or reinforcement material (Chawla 1998). By convention, the matrix is taken to be the more compliant phase and acts as a binder for the stiffer/stronger reinforcement phase. Ceramics, metals, and polymers are the three main classes of matrix materials; corresponding to the nomenclature of polymer-, metal- and ceramic-matrix composites. Most widely-used reinforcements are in the form of continuous fibers, discontinuous fibers or particulates; and these categories corresponding to terms referring to composites such as those shown in Figure 2.1: continuous fiber-, discontinuous fiber- (often whiskers), and particle-reinforced composites (Clyne *et al.* 1993).

There are advantages and disadvantages associated with each of these reinforcement types. Particles are cheap, available in many forms (spheres, flakes, polygons, etc.), and particle-reinforced composites are usually isotropic although settling during processing can lead to microstructure gradients. Whiskers have a greater aspect ratio (length/diameter = 50 to 10,000) than particulate reinforcements ($l/d \approx 1$) and are typically single-crystals. The lack of crystalline imperfections results in near-theoretical strengths. The main disadvantage of using whiskers is their non-uniform dimensions and

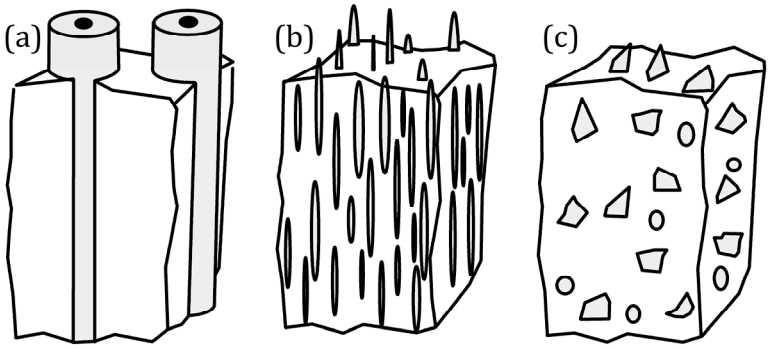

Figure 2.1. Metal matrix composite morphologies consisting of a continuous metal matrix reinforced with (a) continuous fibers, (b) discontinuous whiskers and (c) particles (after Clyne *et al.* 1993).

properties and achieving an even dispersion within a matrix. Fibers, which have even greater aspect ratios, can sometimes approach theoretical strengths and are available in many forms (metal, ceramic and polymer).

Metal/ceramic composites (MCCs) are most often metal-matrix composites (MMCs) with a continuous metal phase surrounding a discrete ceramic reinforcement. Magnesium, titanium, copper and aluminum are common matrix materials. Magnesium and its alloys are light-weight but limited by their low melting temperatures and high reactivity with oxide materials. Titanium and its alloys are attractive due to their high melting points and high strength/weight ratio and are typically used in aerospace applications. Processing of titanium-matrix composites is complicated by the high melting point and its high affinity for oxygen, nitrogen and hydrogen. Copper is typically used in applications requiring a high electrical or thermal conductivity. As opposed to magnesium and titanium, where reinforcements serve mainly to improve mechanical properties, reinforcements are added to copper to also decrease the coefficient of thermal expansion of the material.

Aluminum and aluminum alloys are the most widely used matrix material for MMCs. Aluminum is attractive due to its low cost, low density, high toughness and strength, and resistance to corrosion. Alloys are typically used to improve mechanical properties, improve the wetting of reinforcements and decrease unwanted chemical reactions with reinforcements. Particles, whiskers and fibers are all used to reinforce metal matrices. Some common reinforcement materials are alumina (Al_2O_3), SiC, and carbon. The ceramic reinforcements act to stiffen and strengthen the matrix and improve properties at elevated

temperatures. The matrix serves to hold the reinforcement together, distribute applied load, and protect the reinforcement from corrosion.

The wide array of available matrices and reinforcements results in an almost unlimited number of possible composite materials. Even within one matrix-reinforcement combination, several morphologies (Figure 2.2) are possible (Newnham *et al.* 1978). The schematics in Figure 2.2 depict microstructures based on the connectivity of two phases and are designated using two numbers that indicate in how many dimensions (zero through three) the dark and light phases, respectively, are continuous. A particle-reinforced composite is an example of a '3-0' composite, and a '3-1' composite is an example of a uniaxial continuous fiber-reinforced composite.

Interpenetrating phase composites (IPCs), represented by the '3-3' schematics, represent a relatively new topic of interest in materials science. Each phase in an IPC is continuous throughout the composite, which contrasts the typical composite structure with a continuous matrix surrounding a discreet and isolated reinforcement phase (Clarke 1992). The interest in IPCs is largely due to the possibility of superior properties compared to non-IPC. Finite-element modeling indicates that elastic, strength, and thermal expansion properties could benefit from the interpenetrating microstructure; especially in the case of composites with two considerably different constituents (Wegner *et al.* 2000a). On the other hand, experimental results have shown varied levels of agreement with the modeling but indicated that one advantage may be that each phase contributes its most advantageous property (Wegner *et al.* 2000b, 2001).

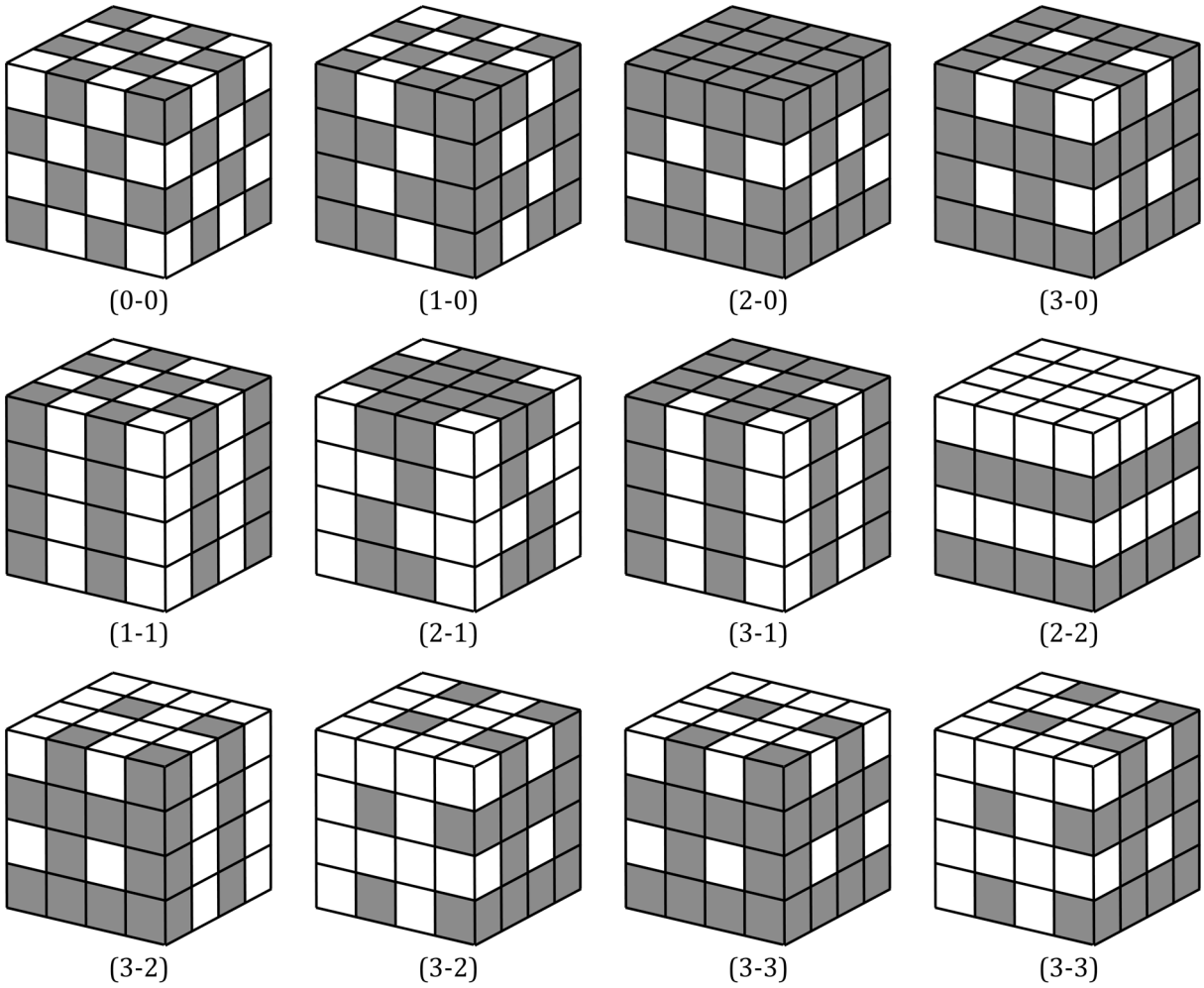

Figure 2.2. Schematics depicting possible two-component composite morphologies based on the interconnectivity of the dark and light phases (after Newnham *et al.* 1978).

2.1.3. Processing

Most metal/ceramic composite processing techniques fall into two groups: solid- and liquid-state processes. This section will briefly describe powder metallurgy, a solid-state process, before emphasizing liquid-state processes and then focusing specifically on infiltration techniques, which were the main processes used in this work.

Solid-State Processing

Powder metallurgy (PM) is one of the more common solid-state processing techniques and involves pressing a blend of matrix and reinforcement powders into a dense component (Schwartz 1997). Specifically, fine powders are combined and pressed using cold isostatic compaction. This yields an ≈ 80% dense part that is degassed to remove absorbed or adsorbed water. Hot isostatic pressing is then used to produce a composite with ≈ 2% porosity. Finally, the pressed material is deformed by extrusion or rolling to strengthen the composite, disperse reinforcement agglomerates and break up any oxide that may have existed on the surface of the original metal powders.

There are several limitations associated with the PM technique including the high processing and materials costs. Furthermore, the resulting composites are often anisotropic due to the final deformation, and the oxide remnants can serve as weak points in the component. It is also difficult to make near-net-shape parts in anything other than basic shapes due to the final processing step. More detailed information on PM and other solid-state processing techniques can be found in the literature (Clyne *et al.* 1993; Schwartz 1997; Chawla 1998).

Liquid-State Processing

The advantages of using liquid-state processes are the faster processing times, lower cost and the ability to manufacture near-net-shape parts. Disadvantages include limitations on the amount of ceramic reinforcement that can be used and reactions that may occur between the metal and ceramic. Compared with solid-state processes, reactivity between the metal and ceramic is more pronounced and can affect the final composite microstructure and properties. In some cases, a reaction can create a beneficial interface between the metal and ceramic that acts to strengthen the bond between the two materials. In most cases though, the interfacial phase is brittle and deleterious to mechanical properties. A common example is the reaction of liquid aluminum and SiC to form aluminum carbide (Al_4C_3),

$$4Al + 3SiC \rightarrow Al_4C_3 + 3Si \tag{2.1}$$

which is a brittle intermetallic compound. Also, the silicon reaction product added to the metal decreases ductility and the melting point, which can alter the composite microstructure and mechanical properties. Table 2.1 lists some other common composite systems and any reaction products that may result during liquid-state processing.

Table 2.1. Common composite components and the possible interfacial reaction products (Chawla 1998).

Reinforcement	Metal	Reaction Product
SiC	Ti alloy	TiC, Ti_5Si_3
	Al alloy	Al_4C_3
Al_2O_3	Mg alloy	MgO, $MgAl_2O_4$
C	Al alloy	Al_4C_3
B	Al alloy	AlB_2
Al_2O_3+ZrO_2	Al alloy	$ZrAl_3$
W	Cu	None
C	Cu	None
Al_2O_3	Al	None

Stir-casting, also called dispersion processing, is the most basic liquid-processing technique and involves introducing the ceramic phase (usually particles) into the molten metal. Several techniques can be used to incorporate particles into the metal and range in complexity from simply using mechanical agitation to zero gravity processing in an ultrahigh vacuum at high temperatures. Obviously, stir-casting is attractive because it can be cheap and simple, but reinforcement volume fractions are limited to 10-20% and the resulting composites can contain an inhomogeneous distribution of ceramic particles as a result of agglomeration, settling and particle rejection along solidification fronts.

In-situ reaction processes can, however, be used to create a homogeneous microstructure. The ceramic phase in *in-situ* processes is formed by reaction of the liquid metal with another compound such as carbon or air to form a carbide or oxide phase, respectively. Titanium matrix composites can be reinforced with titanium boride and/or

carbide by the *in*-situ reaction of liquid titanium with carbon or boron carbide particles (Lu *et al.* 2001),

$$\mathrm{Ti} + \mathrm{C} \rightarrow \mathrm{TiC} \tag{2.2}$$

$$5\mathrm{Ti} + \mathrm{B_4C} \rightarrow 4\mathrm{TiB} + \mathrm{TiC} \tag{2.3}$$

Directed metal oxidation, DIMOX™, a process developed by the Lanxide Corporation, can be used to make near-net-shape Al_2O_3-reinforced aluminum (Newkirk *et al.* 1986; Schiroky *et al.* 1997) according to the reaction

$$2\mathrm{Al} + \frac{3}{2}\mathrm{O_2} \rightarrow \mathrm{Al_2O_3} \tag{2.4}$$

The Lanxide™ processes have also been used to manufacture aluminum nitride/aluminum composites by reacting the liquid aluminum with nitrogen (Creber *et al.* 1988). The advantages of *in-situ* processes are the homogeneous microstructures, the ability to control the microstructure by altering processing parameters such as the temperature, and the capability to produce near-net-shape parts.

Infiltration processing offers advantages over both solid-state processes and other liquid-state processes. The materials for infiltration are low-cost compared to the powders or foil used in solid-state processes, less degradation of the ceramic occurs and complex near-net-shape materials can be made quickly using tools that are already used for traditional casting techniques. As opposed to other liquid-state processes such as *in-situ* processing, which are limited to specific metal/ceramic systems, infiltration processing is versatile but at a disadvantage due to the typically longer contact time between molten metal and ceramic.

Liquid infiltration processes involve introducing the liquid metal to the ceramic, which is usually held in a mold pre-formed into the desired final shape. The preform can be ceramic material of any morphology, so long as open porosity pathways exist for metal infiltration. Infiltration processes differ according to the manner in which the metal enters the ceramic preform; spontaneous-, mechanical- and gas pressure infiltration are three common processes. The specific technique used depends on the wetting and capillary properties of the metal and ceramic materials and the preform microstructure.

The wettability, i.e. the ability of a liquid to spread on a solid surface, can be described by the surface tensions, γ_{SV}, γ_{SL} and γ_{LV}, of the solid/vapor, solid/liquid, and liquid/vapor interfaces, respectively, and the Young-Dupré equation:

$$\gamma_{SL} - \gamma_{SV} = -\gamma_{LV}\cos(\theta) \tag{2.5}$$

where θ is the wetting angle between a drop of liquid metal and the solid ceramic, as shown in Figure 2.3. When $\theta < 90°$, capillary forces act to drawn the liquid into the pore space, i.e. spontaneous wetting occurs, but only partial wetting occurs when $\theta > 90°$.

In non-spontaneous (non-wetting) scenarios, the work of immersion per unit area, W_i,

$$W_i = \gamma_{SL} - \gamma_{SV} \tag{2.6}$$

is positive, and external work is required to initiate infiltration (Mortensen *et al.* 1992). For liquid infiltration processes, a minimum pressure, P_0, supplied either mechanically or by pressurized gas, is applied to the system to overcome capillary forces acting to impede infiltration,

$$P_0 = S_f W_i \tag{2.7}$$

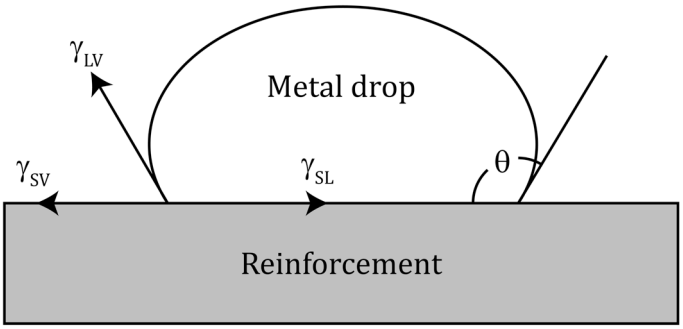

Figure 2.3. Schematic drawing of the interaction of a liquid drop with a solid surface. Wetting is characterized by the Young-Dupré equation, which relates the solid/vapor, liquid/vapor, and solid/liquid surface tensions (γ_{SV}, γ_{LV} and γ_{SL}, respectively) to the wetting angle, θ.

where S_f, which depends on the preform microstructure, is defined as the surface area of interface per unit volume of infiltrated metal.

Spontaneous infiltration does not occur in most metal/ceramic composite systems: Al/Al_2O_3, Al/SiC and Cu/C are all cases where work is required to create liquid/solid interfacial area. Although most infiltration processes use pressure, there are other methods that can be used to promote wetting. Increasing the temperature can decrease the contact angle (Han *et al.* 1993), but this will increase the reactivity between the metal and ceramic, which could increase the amount of interfacial phases. Processing in a different atmosphere or using an alloy can improve wetting: a nitrogen atmosphere and an Al-Mg alloy are known to promote wetting between aluminum and SiC (Zulfia *et al.* 2002). As another example, the contact angle of molten copper on both amorphous and graphitic carbon has been measured in the range 135° to 157° (Silvain *et al.* 2000). However, copper readily wets carbides (Ramqvist 1965) and copper alloys containing carbide-forming elements such as iron and chromium have been shown to wet carbon fibers (Liu *et al.* 1989). Ceramic reinforcements can also be coated with a material known to induce spontaneous infiltration (Rajan *et al.* 1998).

The advantages of spontaneous, or pressureless, infiltration over pressurized infiltration are the lower capital cost and decreased safety concerns associated with pressurized systems. Applying pressure, typically via squeeze casting or gas-pressure, to the system is attractive because there is no need to alter the constituent materials. The rapid application of pressure and subsequent cooling limits the time for metal-ceramic reactions to occur. Also, applying sufficient pressure eliminates residual porosity and

results in dense composites with few limitations on the choice of metal and ceramic phases (Mortensen *et al.* 1993).

The general procedure for pressurized infiltration processes is the same for mechanically or gas-pressurized systems. First, a preform is placed into a mold. Second, the mold is usually evacuated to ensure that no air is entrapped within the final composite. After the mold is heated and the metal melted, pressure is applied and maintained, and the infiltrated composite is finally solidified. Squeeze-casting refers to infiltration processes that use a mechanically-driven piston to apply the pressure (typically up to 100 MPa) to the molten metal. In gas-pressure infiltration, shown schematically in Figure 2.4, an inert gas is used to apply pressures, which are typically up to 10 MPa. The lower pressures used in gas-pressure systems are a disadvantage because they can result in slower infiltration and residual porosity, but the lack of a piston allows more complex preforms and the ability to have the preform entirely within the pressure vessel. Upon pressurization in this case, the mold is in a state of hydrostatic pressure, which allows the use of different mold materials that can improve the processing efficiency.

Calculating the threshold pressure, P_0, requires taking into account the nature of the reinforcement and resulting porosity, the liquid metal, the solid/liquid interface and the experimental conditions. Theoretical and experimental research regarding particle preforms, especially packed SiC preforms infiltrated with Al are extensive, and a brief overview is presented here. In the case of a particle preform, the factors that affect infiltration are the average particle diameter, size distribution, shape, and volume fraction of reinforcement; the surface tension and viscosity of the liquid metal; the contact angle

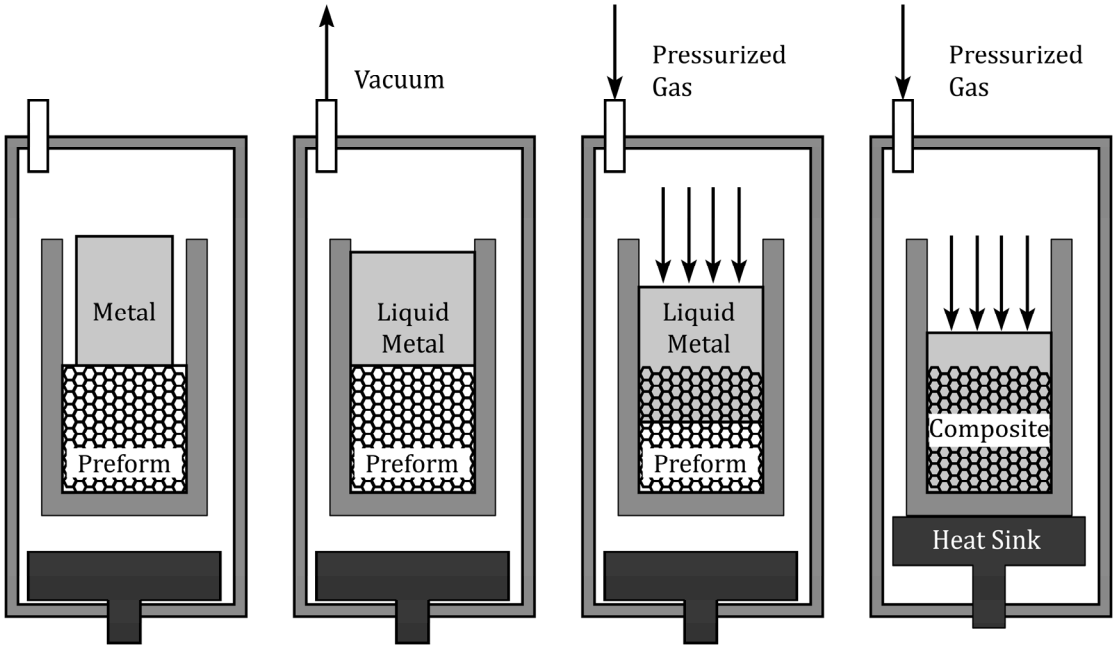

Figure 2.4. Schematic depicting the gas-pressure infiltration process (after Mortensen 2000). From left to right: first, the preform and metal billet are situated in the infiltration furnace. Second, a vacuum is pulled and the temperature is raised to melt the metal. Third, pressurized gas is introduced and forces the metal into the porous preform. Finally, the composite is cooled under pressure.

and reactivity of the solid/liquid interface; and the experimentally-applied pressure, temperature and atmosphere (Garcia-Cordovilla *et al.* 1999). For spherical particles, the term S_f from Equation 2.7 becomes

$$S_f = \frac{6V_p}{d(1-V_p)} \tag{2.8}$$

where d is the diameter and V_p is the volume fraction of particles. After experimentally measuring and plotting the extent of infiltration versus different applied pressures, Garcia-Cordovilla *et al.* used Equations 2.5, 2.7 and 2.8 to develop an expression for P_0 (MPa) as a function of mean particle size and volume fraction,

$$P_0 = 16.15\frac{V_p}{d(1-V_p)} - 0.09 \tag{2.9}$$

The slope of this curve is proportional to the ratio of the permeability of the porous preform, K, to the liquid metal viscosity, μ. This quantity can be related to the average velocity, v, of the infiltration front via D'Arcy's equation

$$v = -\frac{K}{\mu}\frac{\partial P}{\partial x} \tag{2.10}$$

While Equation 2.9 was calculated for Al/SiC, the fit was also reasonable for other particulate systems (Garcia-Cordovilla et al. 1999), and it was also found to be in excellent agreement with experimentally measured values of P_0 for the infiltration of aluminum into a fibrous Al_2O_3 preforms (Mortensen *et al.* 1990).

While similarly in-depth examinations of other preform morphologies are limited, fluid flow through honeycomb materials, which are of particular interest for this study, has been

extensively studied. Solving the Navier-Stokes equation for the case of a group of straight, circular pores results in the Hagen-Poiseuille equation

$$q = \frac{-\pi n d^4}{128\mu}\frac{\partial P}{\partial x} \tag{2.11}$$

where n is the number of pores per unit area, d is the pore diameter and q is the flow rate per unit area, which also equates to D'Arcy's law (Equation 2.10) (Scheidegger 1974). For cylindrical pores, the term S_f from Equation 2.7 becomes

$$S_f = \frac{4}{d} \tag{2.12}$$

and Equations 2.5, 2.7 and 2.12 can be simplified to solve for P_0,

$$P_0 = \frac{-4\gamma_{LV}\cos(\theta)}{d} \tag{2.13}$$

which is equivalent to the Washburn equation (Washburn 1921).

2.1.4. Solidification

The final process occurring after infiltration of the ceramic preform is solidification of the metal phase. The presence of the ceramic reinforcement will affect the nucleation and growth of the solid metal phase. The majority of studies devoted to the effect of reinforcements on metal solidification have involved continuous fiber- or particle-reinforced composites. An overview of the more relevant experimental findings is presented as connections can be drawn from the results of these studies to composites with other morphologies, such as honeycombs.

A major effect of the ceramic phase is the possibility of grain refinement, which occurs when the reinforcement promotes nucleation or restricts the metal. For example, grain refinement was observed in hypereutectic Al-Si alloys (> 12 wt% Si) with carbon, SiC, or Al_2O_3 reinforcements due to the preferential nucleation of Si on the ceramic. The result is a metal microstructure with a greater number of primary Si crystals per unit volume compared to the unreinforced metal. In addition to the effects of preferential nucleation, refinement within a honeycomb material is also expected to occur due to the restricted space within the pores.

Once nucleation occurs, solidification of the metal can also be affected by the reinforcement. In some composites, namely particle-reinforced, movable reinforcements can be either consumed or rejected by the solidification front depending on many factors including particle size, metal/ceramic wettability, the cooling rate and temperature gradient. Rejection by the solidifying metal will lead to particle macrosegregation in the regions of the composite that solidify last. This effect is not observed in situations with fixed reinforcements (fibers, honeycomb, etc.), but the cooling rate and temperature gradient through the composite can affect the dendritic structure of metal alloys (McCartney *et al.* 1981).

2.1.5. Properties

In terms of MMCs, the ceramic reinforcement is incorporated to improve the strength, stiffness, fatigue properties and elevated-temperature performance of the metal matrix. Ceramic reinforcements are also used to tailor the coefficient of thermal expansion of

metals used in the electronics industry. On the other hand, the main contribution of a metal phase incorporated into a ceramic is the increased resistance to crack growth.

Elastic Behavior

The Voigt-Reuss equations, usually called the rules of mixtures (ROM), are the typical means by which the elastic behavior of a composite material is calculated. The upper and lower bounds correspond to states of isostrain and isostress, respectively, and are calculated as follows for a two-phase composite. In an isostrain state (Voigt model), the modulus, which corresponds to the longitudinal modulus, E_{11}, in a fiber-reinforced composite, is

$$E_{11} = E_m V_m + E_c V_c \tag{2.14}$$

where E and V denote the modulus and volume fraction, respectively, of the metal (m) and ceramic (c). In an isostress state (Reuss model), which corresponds to the transverse orientation in a fiber-reinforced composite, the modulus, E_{22}=E_{33}, is

$$E_{22} = E_{33} = \frac{E_m E_c}{V_m E_c + V_c E_m} \tag{2.15}$$

Another set of elastic bounds are the empirically-developed Halpin-Tsai equations (Halpin *et al.* 1976; Chawla 1998), which have the form

$$\frac{E}{E_m} = \frac{1 + \xi \eta V_f}{1 - \eta V_f} \tag{2.16}$$

where

$$\eta = \frac{E_f / E_m - 1}{E_f / E_m + \xi} \tag{2.17}$$

where E, E_f, and E_m are the composite, reinforcement, and matrix moduli (E_{11} or E_{22}), V_f is the reinforcement volume fraction, and ξ is an empirical factor that depends on the reinforcement geometry and distribution and the loading conditions. Once ξ is known for a particular geometry and loading condition, the Halpin-Tsai expressions can be used to predict the properties for a wide range of reinforcement volume fractions (Halpin *et al.* 1992; Daniel *et al.* 1994). In the case of transverse loading, the empirical nature of the Halpin-Tsai expressions is advantageous because, unlike the Reuss isostress assumption, ξ accounts for any non-uniform stress state caused by variations in the local reinforcement volume fraction. It should also be noted that, in the case of $\xi \rightarrow \infty$, Equation 2.16 reduces to Equation 2.14, and in the case $\xi \rightarrow 0$, Equation 2.16 reduces to Equation 2.15.

Fracture Toughness

It is well-known that the incorporation of a metal phase improves the toughness of brittle materials (Sigl *et al.* 1988; Ashby *et al.* 1989; Bannister *et al.* 1992). When constrained by a ceramic phase, metal inclusions stretch plastically in the wake of a crack, as shown in Figure 2.5. The energy absorbed during stretching contributes to the toughness of the composite. Other factors contributing to the composite toughness are residual stresses, crack shielding and decohesion at the metal/ceramic interface. The

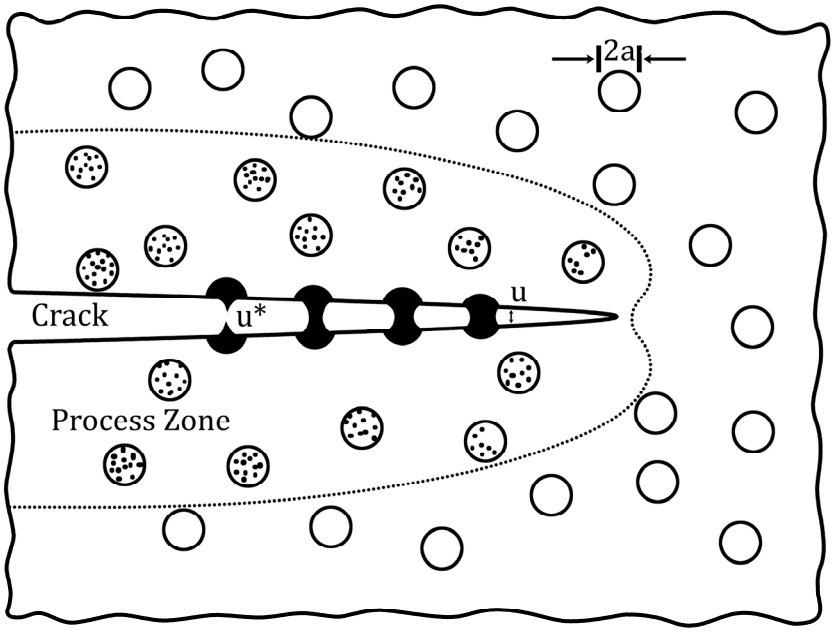

Figure 2.5. Schematic representation of ductile particles stretching in the wake of a crack propagating through a ductile-particle reinforced brittle material (after Ashby *et al.* 1989).

contribution from residual stress is due to the metal/ceramic thermal expansion mismatch which creates tensile and compressive stress states in the metal and ceramic, respectively, that can affect the crack opening force. Crack shielding occurs due to plastic strain within the metal in a process zone.

The degree of constraint experienced by the metal, and hence the amount of decohesion upon crack propagation, has been shown to have a strong effect on the contribution of metal inclusions to the toughness of a metal/ceramic composite (Ashby *et al.* 1989). Weakly bonded metal will simply pull free with almost no toughness contribution, but a constrained inclusion will plastically deform. This was shown experimentally by Ashby *et.al.* (1989), who subjected lead wires constrained within glass capillaries to tensile testing. Although the normalized maximum stress decreased as the amount of decohesion increased, the average elongation increased, which resulted in a greater toughness contribution.

The contribution of a constrained metal particle to the critical energy release rate, G_c, is

$$\Delta G_c = V_f \int_0^{u^*} \sigma(u) du \tag{2.18}$$

where V_f is the volume fraction of metal, u* is the crack-opening displacement (COD) at failure of the ductile inclusion, and σ(u) is a function describing the stress carried by an inclusion at a given COD, u. The integral in Equation 2.18 is equal to the work required to stretch the inclusion, W,

$$W = C\sigma_y a_0 \tag{2.19}$$

where σ_y is the yield stress of the metal, a_0 is the inclusion radius, and C is an experimentally-determined constant that depends on the level of constraint of the metal and was found to be

$$C = 2.5\frac{u^*}{a_0} \tag{2.20}$$

Combining Equations 2.18 through 2.20 yields a solution for the energy contribution,

$$\Delta G_c = CV_f \sigma_y a_0 \tag{2.21}$$

which is related to the contribution to the fracture toughness,

$$\Delta K_{IC} = \sqrt{CV_f E \sigma_y a_0} \tag{2.22}$$

where E is the elastic modulus of the metal. This is a relatively simple, yet effective equation that predicts the greater contributions from high modulus, high strength inclusions. It also suggests that larger inclusions will result in a greater toughness.

Thermal Conductivity

With respect to unidirectional composites, the longitudinal and transverse conductivities are often calculated using the ROM bounds, Equations 2.14 and 2.15. The Halpin-Tsai model, Equations 2.16 and 2.17, are also used with the thermal conductivity, k, in place of E for each constituent, with $\xi = \infty$ for the upper bound and $\xi = 1$ for the lower bound (Chawla 1998). In metal/ceramic composites, the interface can affect the conductivity, and more complex models (see Halpin 1992 and Chawla 1998) have been developed to account for imperfect thermal contact at the metal/ceramic interface.

Coefficient of Thermal Expansion

The upper bound for the coefficient of thermal expansion (CTE) of a continuous fiber-reinforced composite, according to both Schapery and Chamis, is

$$\alpha_{cl} = \frac{\alpha_m E_m V_m + \alpha_f E_f V_f}{E_m V_m + E_f V_f} \tag{2.23}$$

where α, E and V are the CTE, modulus and volume fraction of the matrix (m) and fiber (f), respectively (Chawla 1998). In the transverse direction, the CTE is

$$\alpha_{ct} = (1+\nu_m)\alpha_m V_m + (1+\nu_f)\alpha_f V_f - \alpha_{cl}\bar{\nu} \tag{2.24a}$$

$$\bar{\nu} = \nu_f V_f + \nu_m V_m \tag{2.24b}$$

according to Schapery and

$$\alpha_{ct} = \alpha_f \sqrt{V_f} + \alpha_m (1-\sqrt{V_f})\left(1 + \frac{\nu_m V_f E_f}{E_f V_f + E_m V_m}\right) \tag{2.25}$$

according to Chamis, where ν is the Poisson's ratio of the fiber or matrix. These expressions assume a perfect mechanical bond between the matrix and fiber, perfectly aligned continuous fibers and that the constituent properties are independent of temperature.

As with the thermal conductivity, there are also more complex transverse models (see Halpin 1992 and Chawla 1998). The difficulty involved in predicting the CTE has to do with constraint of the phase with the larger CTE. If the fiber has a CTE less than that of the matrix, longitudinal expansion will be constrained. On the other hand, if the fiber has a CTE greater than that of the matrix, the fiber will be constrained in the transverse direction.

2.2. Contiguous Ceramic Preforms

2.2.1. Introduction

While there is great versatility with infiltration processing, one of the more complicated steps is preparing the ceramic preform. Particulate preforms can be made by simply packing the material into a mold, but binders are typically used to ensure that particles, whiskers or fibers remain stationary during handling and infiltration. The volume fraction of ceramic can be varied by using combinations of different particle sizes or combinations of particles with whiskers or continuous fibers. Ceramic volumes of 40-60% are common, but it is possible to get as low as 5% or as high as 90% with randomly-oriented non-equiaxed reinforcements or sintered and equiaxed powder particles, respectively (Mortensen 2000).

Recently, metal/ceramic composite research has foregone many of the complications associated with preform preparation by utilizing three-dimensionally contiguous open-porosity ceramic structures. Three main processing routes (Figure 2.6) can be used to create a wide variety of ceramic materials with a wide range of porosities and pore sizes (Colombo 2006; Studart *et al.* 2006). A wide range of structures including foams, honeycombs and interconnected fiber meshes can be made by using sacrificial templates, direct foaming or template replication. A brief description of these three processing methods follows.

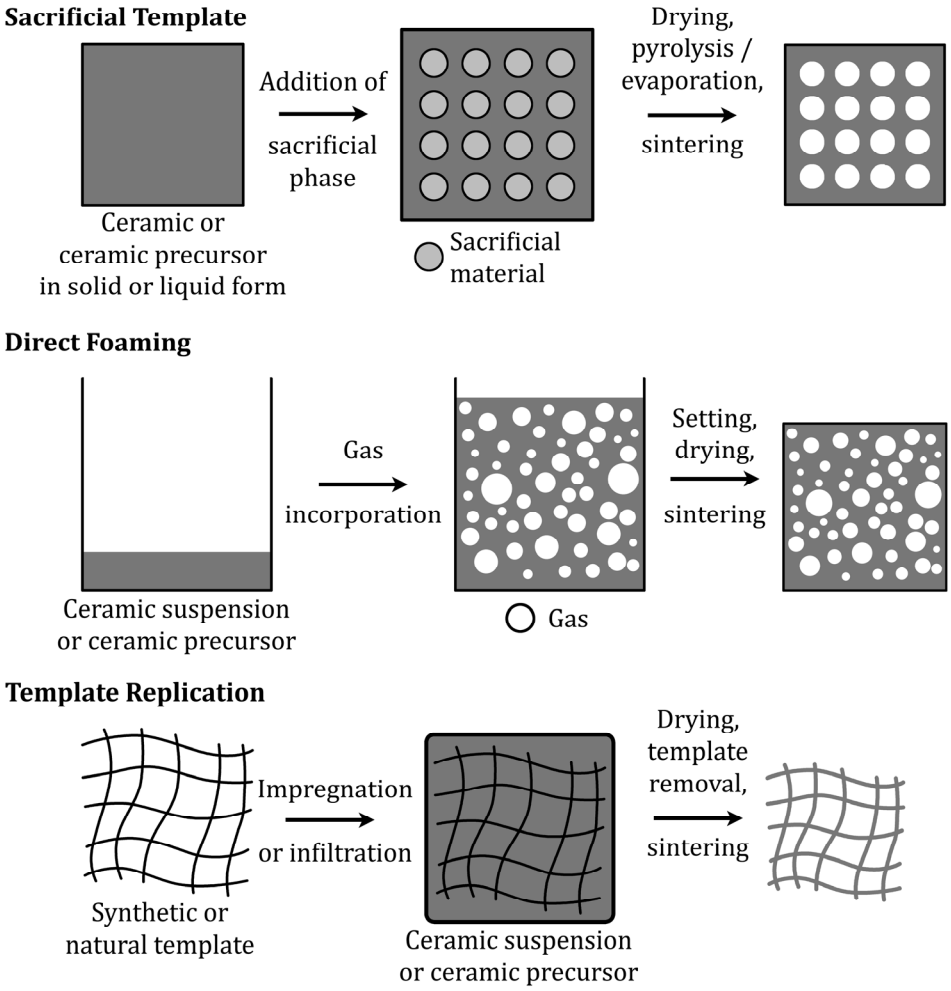

Figure 2.6. Schematic representation of three macroporous ceramic processing routes: (top) sacrificial templating, (middle) direct foaming and (bottom) template replication (after Studart *et al.* 2006).

2.2.2. Processing

Sacrificial Template

The porosity in this technique is created by decomposing a fugitive phase. The pore size, shape and volume fraction are controlled by the initial morphology and amount of filler, which is combined with a ceramic or pre-ceramic material. After initial drying, the fugitive phase is removed by one of several methods including high-temperature burn out or chemical etching. Finally, the material is sintered to create the final porous structure. Typical filler materials include starch, polymer beads and silica. The resulting ceramic structure is the negative of the starting fugitive filler, as shown in Figure 2.6 (Studart *et al.* 2006).

Using sacrificial templates is relatively simple and versatile due to the wide range of possible fugitive phases that can be used and the wide range of ceramics that can be manufactured. The main disadvantage is the care needed to minimize damage to the ceramic when using high temperatures or strong acids to remove the filler material. Also, in regards to using the porous material as a metal-infiltration preform, the amount and spatial distribution of the fugitive phase must result in open porosity.

Direct Foaming

A vapor phase is used as the source of porosity in direct foaming techniques. After incorporation of stable gas bubbles, the ceramic slurry or suspension is set and usually sintered. The porosity in the final ceramic is proportional to the amount of introduced gas, and the amount and size of final porosity depend on the stability of the system while

setting occurs. The gas bubbles can be introduced via mechanical agitation, direct injection of a gas or as the product of a chemical reaction. The gas-ceramic mixture is stabilized by using either surfactants or particles to deter Ostwald ripening and coalescence of the bubbles (Colombo 2006).

Direct foaming can result in porosity volume percents between 40 and > 95% with pore sizes ranging from 10 μm to 1200 μm depending on the specific foaming method and stabilization techniques used. In addition to these wide ranges, direct foaming can be used to make a variety of ceramic materials, but the pore morphology is limited to interconnected spheres.

Template Replication

Synthetic or natural templates, such as polymer foams or coral, can be impregnated or infiltrated to create a replica of the starting material. As with the sacrificial template technique, the original template is then removed and the structure is sintered. As opposed to the sacrificial template-formed ceramics, the replication technique results in a structure resembling the starting material (Studart *et al.* 2006). The advantages and disadvantages are similar to those associated with using fugitive fillers as cracking can occur upon removal of the template. Also, especially in the case of foam templates, the resulting ceramic struts are often hollow, resulting in weaker materials; although it is possible to reinfiltrate the material to solidify the struts (Jun *et al.* 2006).

2.3. Wood

2.3.1. Introduction

Wood is composed of several constituent materials fashioned into a complex composite microstructure. Understanding the composition and structure of wood is important to understanding how it can be processed into a ceramic, can be used as a preform for melt-infiltration, and can affect the mechanical and thermal properties of the resulting metal/ceramic composite.

2.3.2. Microstructure

Wood is a honeycomb-like anisotropic material with cells aligned both parallel and perpendicular to the long axis of the tree (Dinwoodie 1989; Gibson *et al.* 1997). While the solid cell walls provide the strength to support the tree, the purpose of the pore space is to either conduct or store water and food throughout the tree. Cells that provide support (tracheids and fibers) or conduction (tracheids and vessels) are oriented in the longitudinal or axial direction, parallel to the long axis of the tree, as shown in Figure 2.7. Storage cells (parenchyma) occur in groups called rays and are radially-oriented.

In general, woods are classified into two main groups: hardwood (angiosperms) or softwood (gymnosperms) (Wheeler 2001). Vessels and fibers are exclusively found in hardwoods, but tracheids and rays are found in both wood types. Representative hardwood and softwood microstructures are shown in Figure 2.8. The diameters of vessels, the largest cells, are typically 25-300 μm while fibers, tracheids and parenchyma are between 10 μm and 40 μm in diameter, and tracheids are usually larger than either

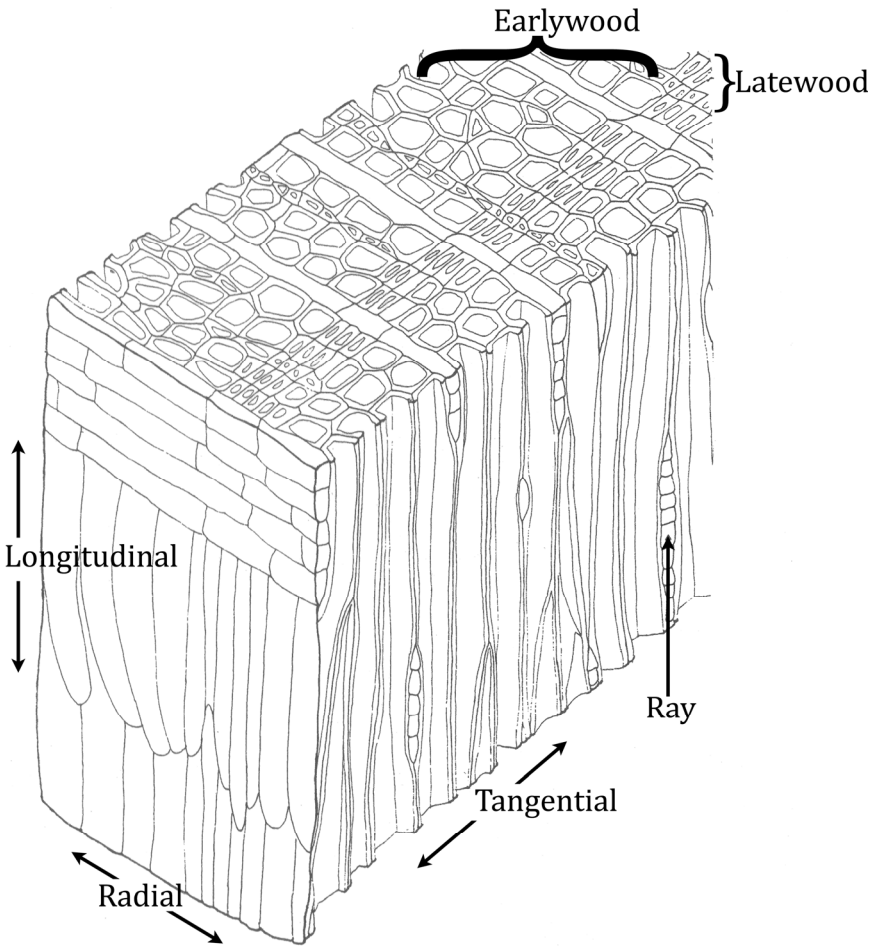

Figure 2.7. Three-dimensional view of wood showing the longitudinal, radial and transverse directions along with typical microstructural features: early wood, late wood, and rays (after Wainwright 1976).

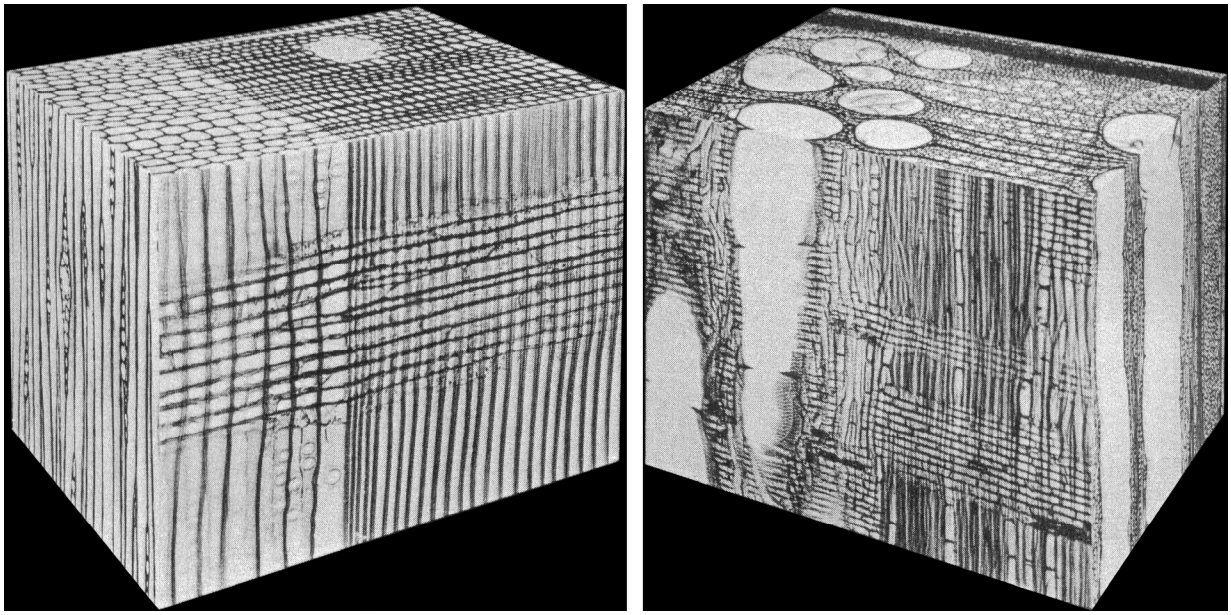

Figure 2.8. Three-dimensional view of the structures of (left) softwood and (right) hardwood (Dinwoodie 1989).

fibers or parenchyma. Variations in wood microstructures are due to different ratios of large- to small-diameter cells and the spatial distribution of the cells. Trees in temperate regions, such as the tropics, have wood with a more uniform microstructure. Trees that experience seasonal growth form defined growth rings, which are the concentric circles often visible to the naked-eye in transverse wood sections.

Two types of wood, early- and late wood, are present in each growth ring and serve to promote conduction and support, respectively (Wheeler 2001). In softwoods, the transition from early- to late wood is manifested by the gradual decrease in tracheid diameter and increase in cell wall thickness. In some hardwoods, the early wood contains a majority of the vessels while the late wood contains a smaller number of small-diameter vessels and a greater proportion of fibers. In other hardwoods, the difference between early wood and late wood is less distinguishable. These two hardwood types are classified as ring- and diffuse porous, respectively, and the micrographs of oak and birch wood shown in Figure 2.9 depict the differences between the two microstructures. The ring- and diffuse porous classifications are the extremes of a spectrum, and many hardwoods fall in the middle. Poplar, shown in Figure 2.10, is an example of these semi-ring porous woods.

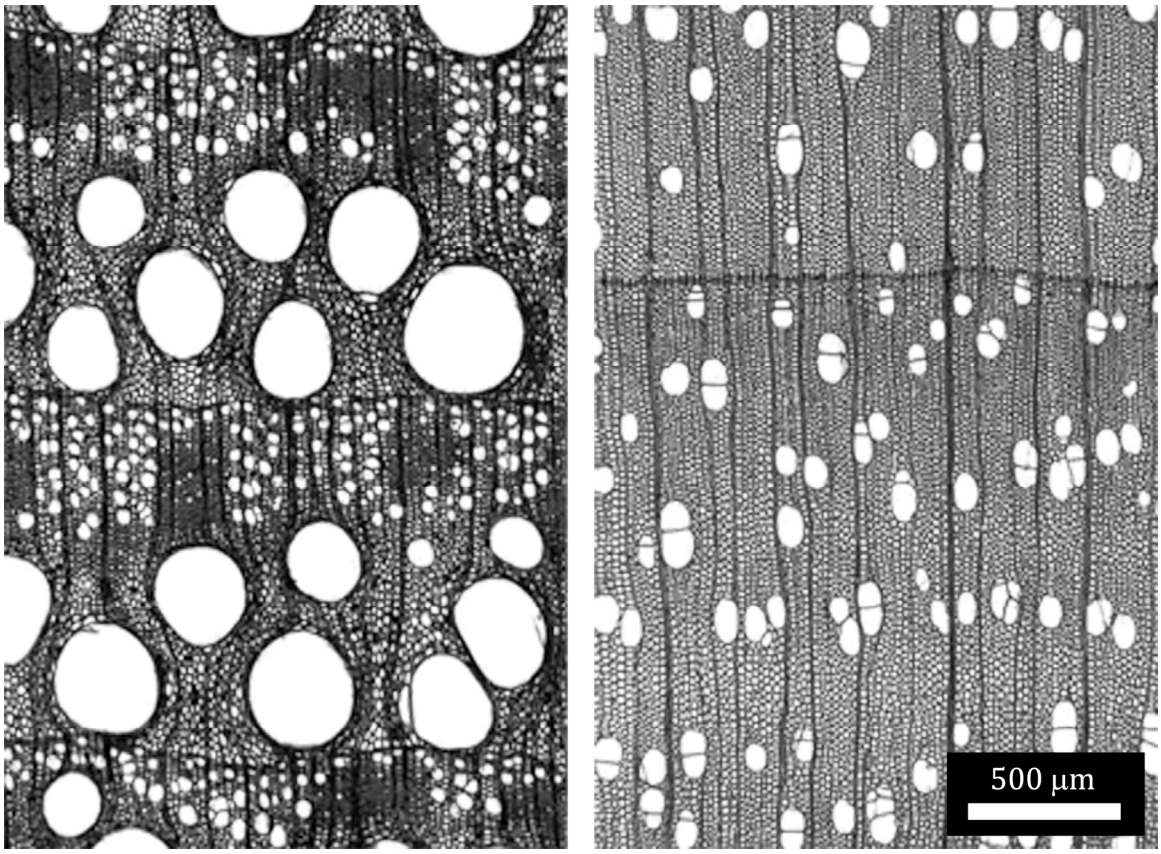

Figure 2.9. Optical micrographs of (left) oak (*Quercus petraea Liebl.*), a ring porous hardwood, and (right) birch (*Betula alba*), a diffuse porous hardwood (Schoch *et al.* 2004).

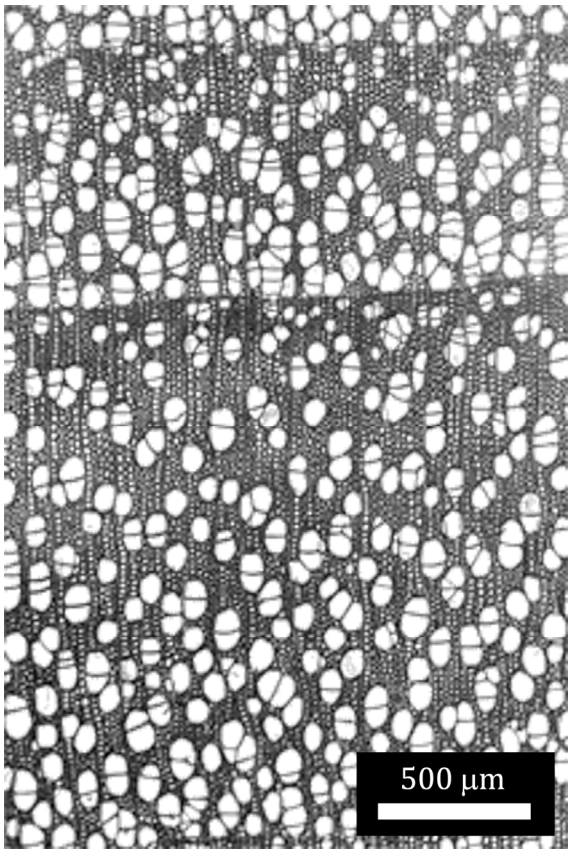

Figure 2.10. Optical micrograph of poplar (*Populus alba L.*), a semi-ring porous hardwood (Schoch *et al.* 2004).

2.3.3. Ultrastructure & Chemical Composition

Wood is not only anisotropic on the microstructural scale: the cell walls themselves are also anisotropic and consist of a multi-layer structure as shown in Figure 2.11 (Conners 2001). The layered structure is common to all wood species, but the thickness of the layers can vary. Each individual layer resembles the ply of a fiber-reinforced composite, and the layers are rotated to various angles, which results in a tough and stiff composite cylinder. The plies themselves are composed of microfibrils, which are collections of aligned and partially crystallized cellulose surrounded by a matrix of amorphous cellulose, hemicellulose and lignin; the three main chemical components in wood. The primary cell wall (P) is thin and contains randomly-oriented microfibrils surrounded by lignin. The secondary cell walls (S1-S3) contain microfibrils oriented at angles ranging from 5° to 90° to the axial direction and contain approximately 50% cellulose. The middle lamella (ML) is comprised almost entirely of lignin.

Cellulose is a polymer with chains on the order of 5 μm in length (Dinwoodie 1989; Mabee *et al.* 2001; McDonald 2001). About 70 percent of the cellulose in wood is crystalline, in segments measuring about 60 nm. Hemicellulose refers collectively to four similarly-structured polymer molecules that resemble the structure of cellulose (Figure 2.12). Compared to cellulose, hemicellulose polymers have lower molecular weights and are more amorphous. Lignin is an amorphous compound that acts as a binder within and between wood cells. While cellulose, hemicellulose and lignin are present in all woods, the percentage of each can vary between species. Table 2.2 lists the approximate percentage of each chemical constituent in softwoods and hardwoods.

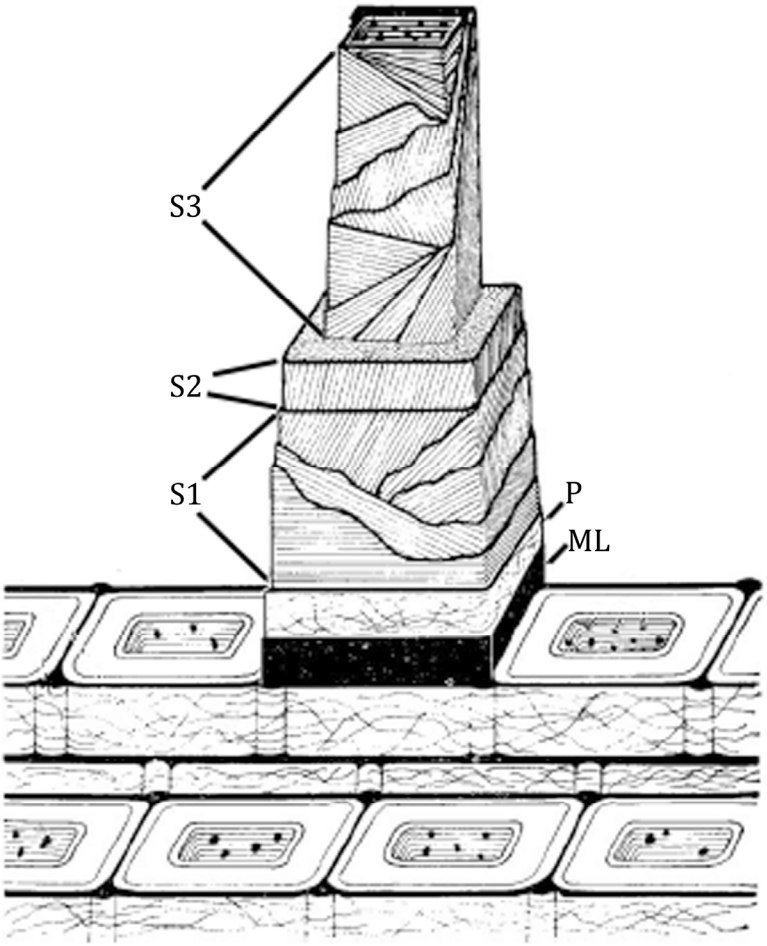

Figure 2.11. Cell wall structure of wood based on the late wood tracheids of pine wood (after Conners 2001).

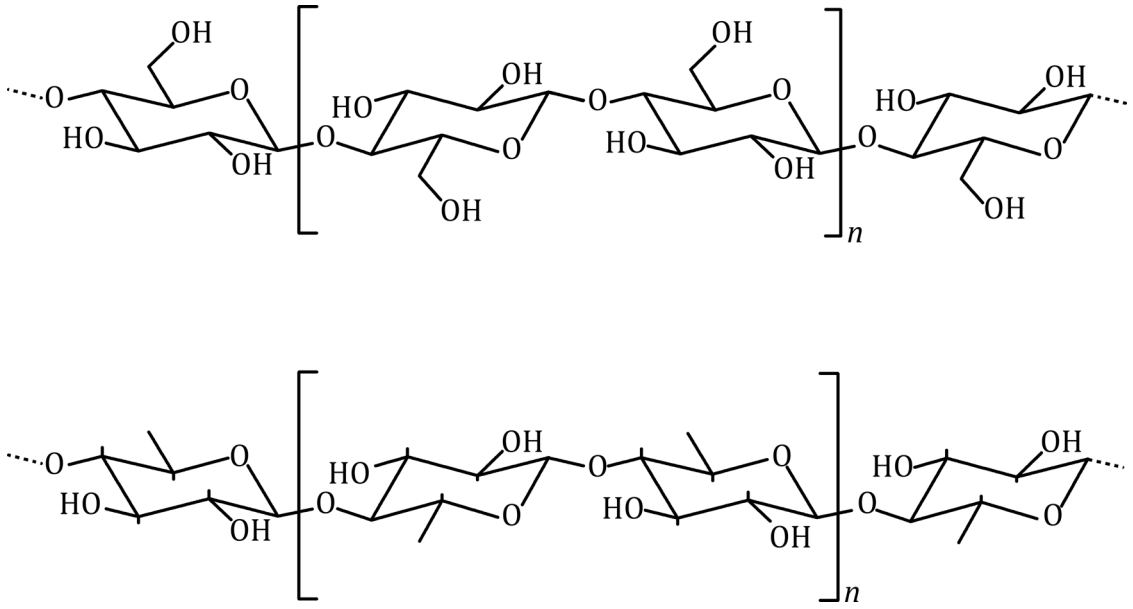

Figure 2.12. The chemical structures of (top) cellulose and (bottom) hemicellulose (after Greil 2001; McDonald 2001).

Table 2.2. Approximate percentage of cellulose, hemicellulose, and lignin in hardwoods and softwoods (Dinwoodie 1989; Mabee *et al.* 2001).

	% of dry mass	
	Hardwoods	Softwoods
Cellulose	40-45	40-50
Hemicellulose	25-35	21-35
Lignin	20-40	22-40

2.3.4. Conversion to Ceramics

Despite the relatively simple chemical composition, wood has evolved into an incredibly complex structure that is uniquely suited to be stiff, strong, and tough in compression and bending. There are many recent examples of research that seek to replicate or mimic complex natural structures in order to produce engineered materials with improved mechanical and thermal properties. Wood is no exception and is the focus of several research groups, which are processing wood and wood-based products into many different ceramic materials.

As shown in Figure 2.13, the first step in producing many wood-derived ceramic products is first producing a carbon template (Sieber 2005). Experimentally, this is a simple procedure that amounts to producing charcoal. The idea to then process the carbon templates into ceramic materials was first introduced in the mid-1990s, and microstructure-property correlations of wood-derived SiC were first made in the late-1990s (Ota *et al.* 1995; Greil *et al.* 1998a, b). In addition to SiC, research has also been devoted to studying wood-derived alumina, silica, titania, zirconia, and titanium carbide.

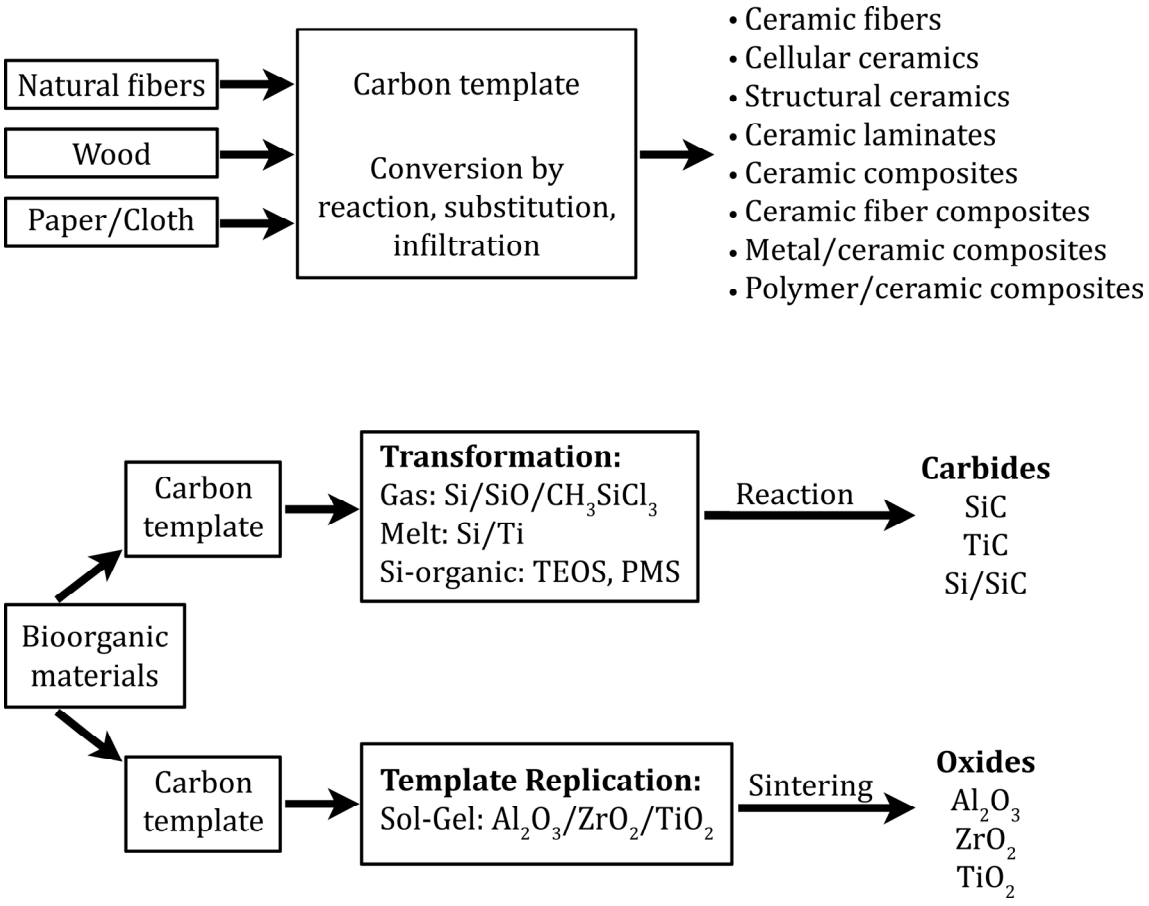

Figure 2.13. Flowchart for the conversion of wood and wood products into a variety of ceramic materials and morphologies (after Sieber 2005).

Using wood as a precursor presents several advantages over tradition porous ceramic processing routes (de Arellano-López *et al.* 2004). Wood and paper products are inexpensive starting materials and are available in a wide array of morphologies (bulk wood, fiber board, paper, cardboard, etc.). Carbon, which is the intermediate product, can easily be machined into complex three-dimensional parts using already-established machining techniques. Microstructurally, different wood species cover a wide range of porosities, pore size distributions and pore spatial distributions. The energy requirements for processing are typically lower as processing temperatures are below the ceramic sintering temperatures. Finally, the resulting ceramic products are near-net-shape as there is little to no overall volume expansion upon conversion of carbon to ceramic.

Carbon

Although the overall process of converting the organic wood material into carbon may seem simple, the complexity on the microstructural level warrants a more detailed discussion. With increasing temperature, pyrolysis progresses in several stages (Figure 2.14): desorption and vaporization of water ①; decomposition of hemicellulose ②, decomposition of cellulose and lignin ③; increased rate of cellulose and lignin decomposition ④; and finally the continued decomposition of remaining lignin ⑤ above 400°C (Byrne *et al.* 1997a). The hemicellulose, cellulose, and lignin break down between 200-260°C, 240-350°C, and 280-500°C, respectively, and several gas- and solid-phase products are released including CO, CO_2, and tar.

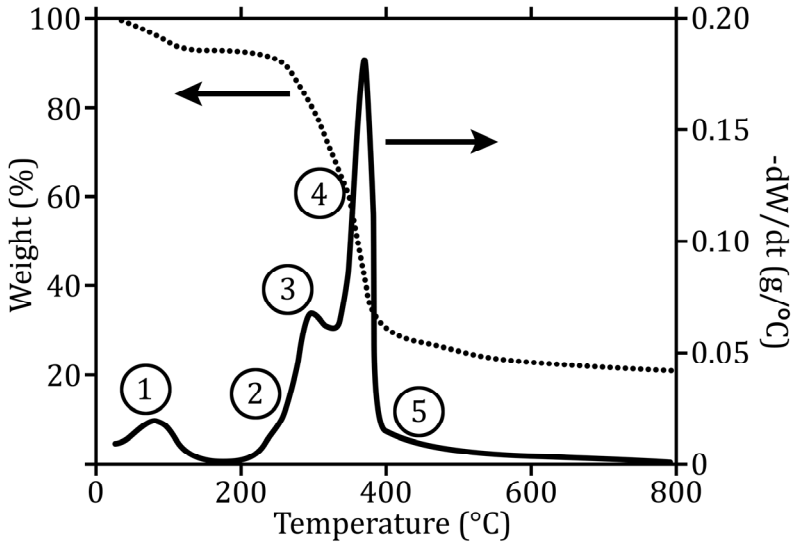

Figure 2.14. Plot of the percent of original weight and the rate of weight loss versus temperature during wood pyrolysis (after Byrne *et al.* 1997a).

The pyrolysis heating rates are extremely slow, typically below 5°C/minute, in order to minimize microstructural damage due to escaping gasses and dimensional changes. Average values for the carbon yield and reduction of bulk density, which vary depending on wood type, are 28% and 18%, respectively. Weight loss during pyrolysis occurs at varying rates as temperature increases, as shown in Figure 2.14. Dimensional changes are anisotropic due to the microfibrils, which have an overall axial-alignment, and average 15-22% in the axial direction and 22-40% in the radial and tangential directions .

In terms of using carbon as a ceramic preform, typical maximum pyrolyzing temperatures are between 800°C and 1000°C. The resulting carbon structure is amorphous, but the carbon layers have an overall axial-orientation, parallel to the original microfibrils. Heating to more extreme temperatures has a limited effect on the carbon structure, as shown in Figure 2.15. Despite pyrolysis temperatures of up to 3000°C, which are typically used in the production of graphite, little evidence of graphitization is seen (Byrne *et al.* 1997a). In fact, the small peak in the area of 26° 2θ is an indication of loosely-ordered turbostratic carbon, not crystalline graphitic carbon. This non-graphitizing behavior is typical of "hard carbons", which show no formation of the three-dimensional graphite structure upon heating to high temperatures (Franklin 1951a).

Oxides

The most common method of forming wood-derived oxides is using sol-gel chemistry and template replication. Alumina, titania and yttria-stabilized zirconia have all been made following the procedure outline in Figure 2.16 (Cao *et al.* 2004b). Low

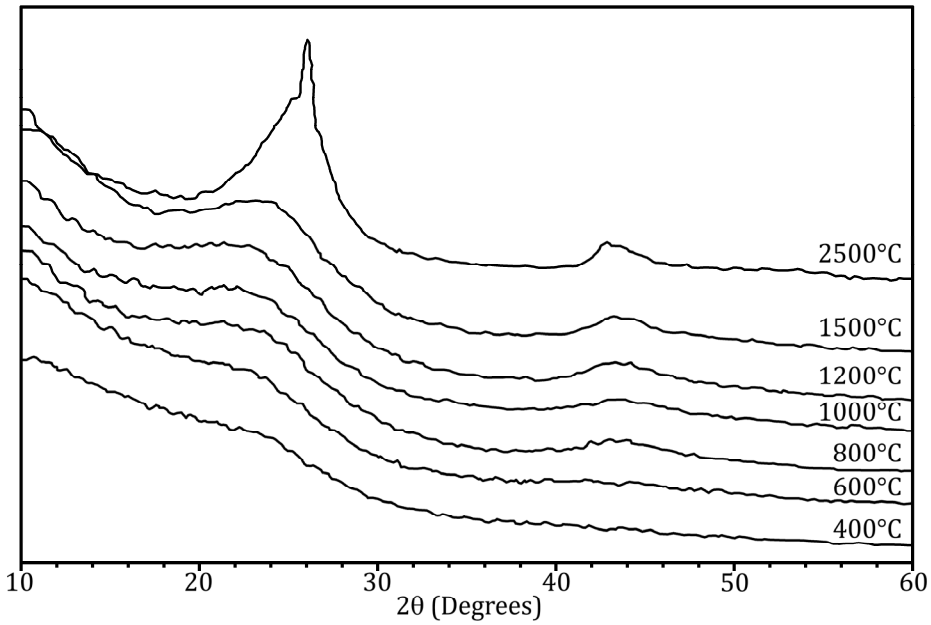

Figure 2.15. X-ray diffraction scans for poplar pyrolyzed at a range of temperatures. The peak in the 2500°C curve at just below 26° corresponds to turbostratic carbon (after Byrne *et al.* 1997b).

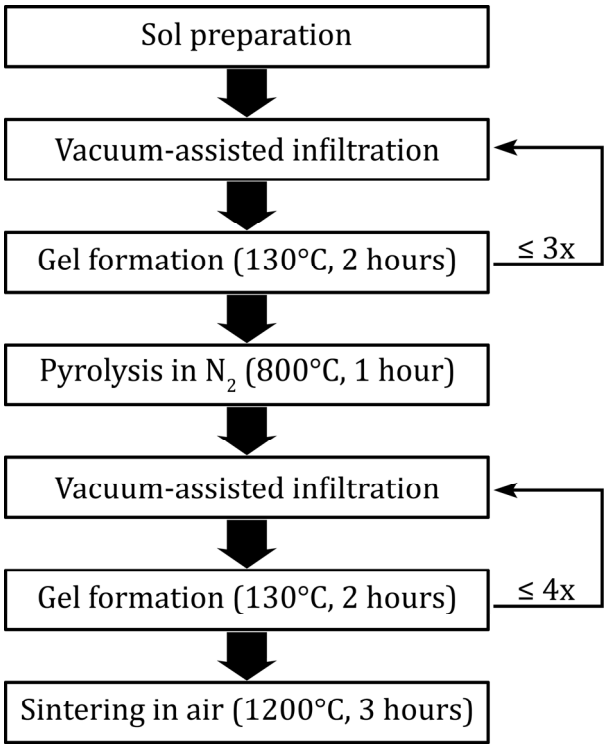

Figure 2.16. Sol-gel processing method used make alumina, titania, and yttria-stabilized zirconia via the template-replication of wood (after Cao *et al.* 2004a; Cao *et al.* 2004b; Rambo *et al.* 2004).

viscosity sols were made by mixing aluminum(III) isopropoxide (Cao *et al.* 2004a), titanium isopropoxide (Ota *et al.* 2000) or a mixture of zirconium oxychloride and yttrium nitrate (Rambo *et al.* 2004) with distilled water and acid to create a colloid consisting of fine Al_2O_3, TiO_2, or Y_2O_3-ZrO_2 particles. Wood dried, but not yet pyrolyzed, was vacuum-infiltrated with the sols and then dried to form a gel that coated the porous wood microstructure. The infiltration procedure was repeated to increase the amount of infiltrated sol before heating the samples to 800°C in nitrogen to pyrolyze the wood. To further increase the amount of ceramic material, a second round of sol-infiltration and drying was carried out. Finally, the materials were sintered in air to remove the carbon, which increased the porosity in the ceramics. The TiO_2 ceramics resulting from processing softwood, hardwood, cellulose fiber felt, and cardboard are shown in Figure 2.17.

Following slightly different processes, sol-gel processing has also been used to make wood-derived manganese oxides (Li *et al.* 2006), silicon dioxide (Shin *et al.* 2001), chromium oxide (Fan *et al.* 2006) and tin oxide (Sun *et al.* 2005). For these materials, the sol precursors were manganese nitrate, tetraethylorthosilicate, chromium nitrate and tin tetrachloride, respectively, and the wood preforms were soaked in the sol instead of being vacuum infiltrated. The soaking took more time, three days versus one hour for infiltration, so the infiltration/drying process was repeated only once before the wood template was removed. The advantages of using the vacuum-infiltration technique are the reduced time and a more homogeneous coating of the template.

TiO_2 has also been made via chemical vapor infiltration (CVI) (Ghanem *et al.* 2007). In this process, the pyrolyzed paper preforms were infiltrated with a mixture of $TiCl_4$, CH_4,

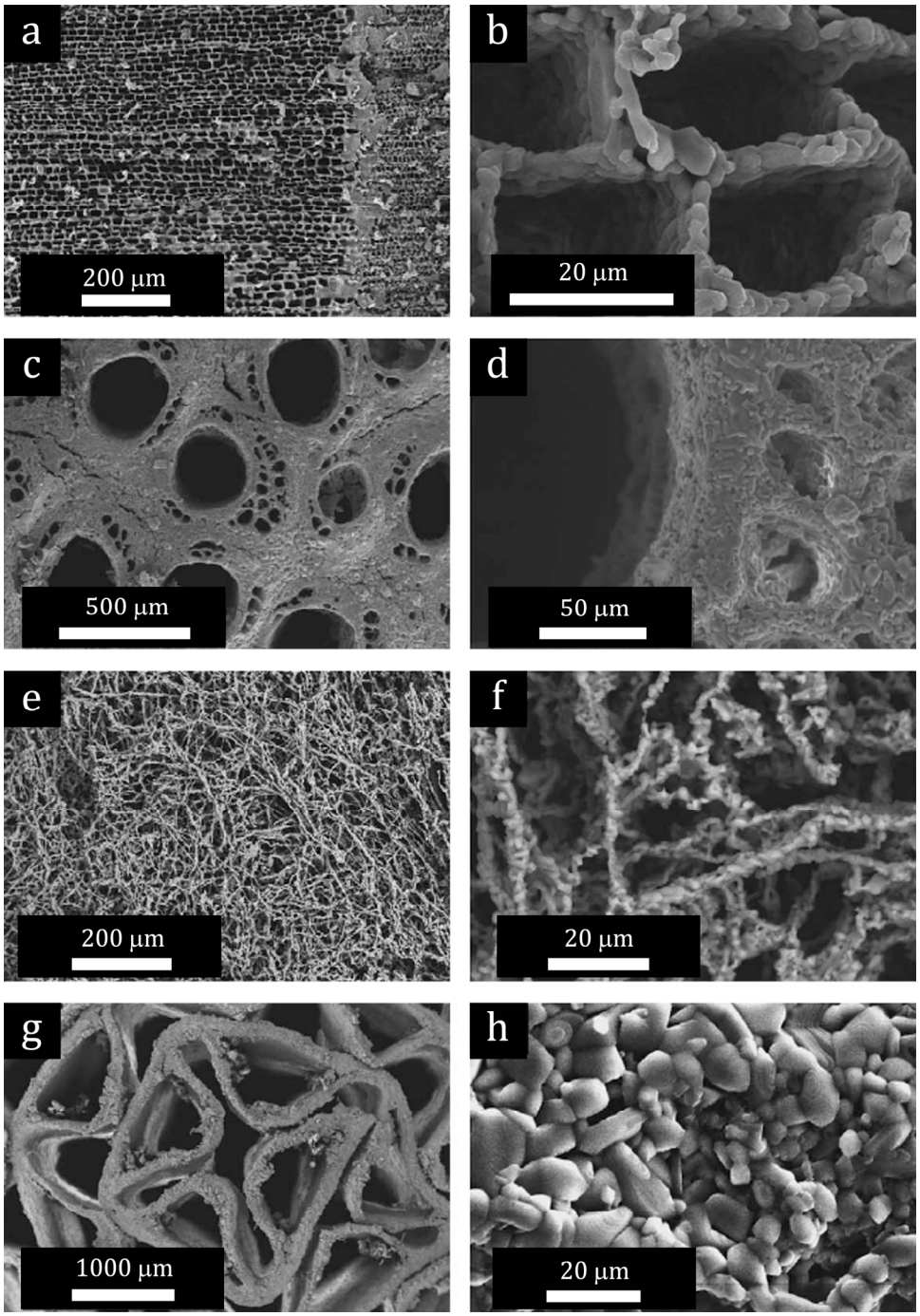

Figure 2.17. SEM micrographs of TiO_2 ceramics derived from (a,b) pine, (c, d) rattan, (e, f) cellulose fiber felts and (g, h) cardboard (Cao *et al.* 2004b).

and H_2 gases, which reacted with the carbon to form TiC. The TiC was then heated in air to temperatures between 400°C and 1200°C, which resulted in various TiC → TiO_2 conversion rates.

Carbides

Currently, wood-derived carbide research is limited to zirconium-, titanium- and silicon carbides made by CVI, sol-gel and liquid metal infiltration (LMI) processes. The CVI procedure for TiC was detailed above, see also (Popovska *et al.* 2005). A similar procedure was used to make CVI SiC (Ohzawa *et al.* 1998; Sieber *et al.* 2002; Streitwieser *et al.* 2005). The sol-gel processing of ZrC (Rambo *et al.* 2005), TiC (Sun *et al.* 2004) and SiC (Ota *et al.* 2000; Herzog *et al.* 2006a) follow procedures similar to that shown in Figure 2.16. Metal-oxide sol-gels are still used, but the starting material is a pyrolyzed amorphous carbon preform, and the final sintering step is carried out in an inert atmosphere. Sintering in argon prevents burn-off of the carbon preform, which reacts with the metal-oxide to form the carbide of interest. Depending on the amount of sol-gel, the final ceramics can still have residual carbon, which could then be burned off in air.

LMI processing has been used to make only SiC due to the relatively low melting temperature of Si (1410°C) compared to Ti (1670°C) and Zr (1860°C). In this process, the pyrolyzed wood is heated to greater than 1410°C with bulk or powdered Si. The silicon melts, is wicked into the carbon preform and reacts exothermically to form β-SiC

$$\mathrm{Si} + \mathrm{C} \rightarrow \beta - \mathrm{SiC} \qquad (2.26)$$

Similar to CVI, this technique constitutes neither template replication nor the use of a sacrificial template in that the pyrolyzed wood is never burned off, but it is reacted directly into the final product.

Several reaction mechanisms have been reported to take place during the LMI of silicon into carbon (Zollfrank *et al.* 2005). Initially, at temperatures below the Si melting point, Si vapor enters the preform and forms a thin layer (< 100 nm) of nanocrystals (19 nm mean diameter). This reaction occurs mainly on the outer surface of larger pores but was also observed in pores less than 10 μm in diameter. Once molten, the Si spontaneously wets and is wicked into the carbon. At this stage, both nano- and coarse-grained SiC are nucleated with the nanograins lining the carbon and forming a barrier between the molten silicon and carbon. This suggests two mechanisms, diffusion of the Si through the nanograined SiC to form more nanograins, and dissolution of C and nanograined SiC into the molten Si to form the coarser SiC grains.

Dissolution of the C and SiC is promoted due to the exothermic C → SiC reaction, and the coarse grains are nucleated within the molten Si at relatively cool sites away from the reaction. The coarse grains (average size = 12 μm) do not form a continuous, dense layer, and the surface of the carbon is distorted due to the volume expansion associated with the reaction. Volume expansions of up to 60% can occur depending on the density of the starting carbon material (Wang *et al.* 2004). Even after one hour at 1550°C, residual carbon can remain in areas where the carbon is thicker than 5 μm or where the volume expansion pinches a pore closed. The amount of residual carbon in the final SiC can be

reduced by using higher processing temperatures and/or longer processing times with an excess of Si (Hou *et al.* 2006, 2007).

The resulting material consists of aggregated nanometer and micrometer sized grains of SiC, residual carbon, and excess silicon (Hillig 1994; Varela-Feria *et al.* 2008). Either carbon felt or acid etching can be used to remove the excess silicon. Above 1410°C, the carbon felt wicks the excess Si away from the SiC. This procedure works well to remove excess Si from outer surfaces, but Si may still remain within the pores. Samples can be soaked in a mixture of nitric acid, which oxidizes the Si to SiO_2, and hydrofluoric acid, which etches away the SiO_2, to cyclically remove the last of the excess silicon.

The pores of the SiC produced via the LMI and CVI processes can have different structures (Greil *et al.* 2002). Figure 2.18 shows the structure of pine wood-derived SiC produced via CVI of SiO, Si, and CH_3SiCl_3 and the structure of SiC produced via the LMI of beech wood. In general, the CVI pore walls are smoother and denser than the LMI material. There are also microstructural differences within the group of CVI SiC, as seen in Figure 2.19. The SiO-derived structure has a uniform structure of submicron grains and more porous pore walls due to the release of carbon monoxide. The Si-derived walls are denser and the interface between cells is still visible in the SiC material. CVI of CH_3SiCl_3, which was mixed with H_2, deposits SiC and Si on the carbon surface. Subsequent heating above the melting point of silicon led to a LMI of the carbon strut, which increased the amount of SiC and led to thicker pore walls.

Producing SiC from wood offers several advantages over conventional ceramic processing methods (de Arellano-López *et al.* 2004). Low processing temperatures use less

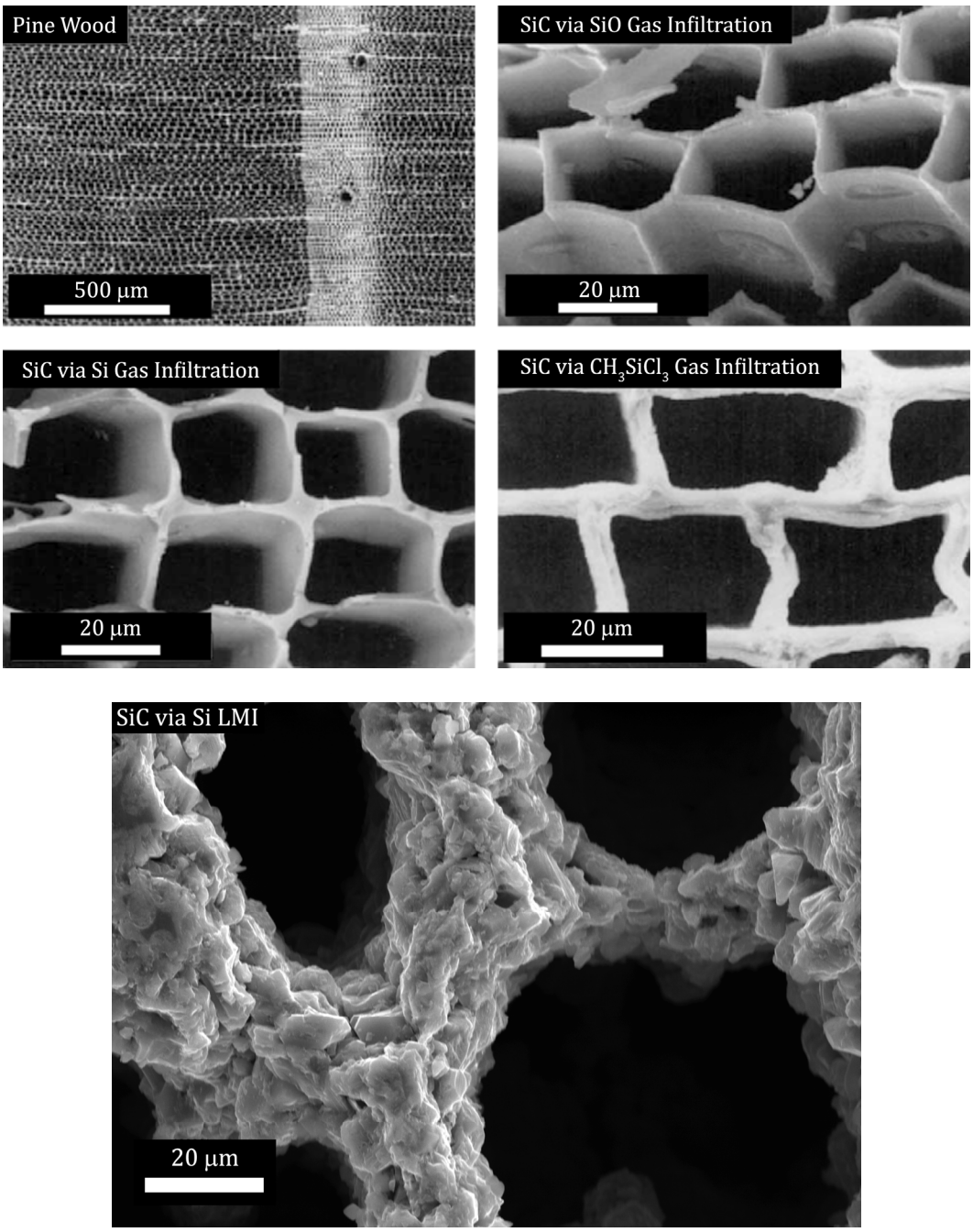

Figure 2.18. SEM micrographs of the microstructures of pine wood and the SiC produced by the gas-infiltration of SiO, Si, and CH_3SiCl_3 (Greil *et al.* 2002). The bottom micrograph is the microstructure of SiC produced from beech wood by liquid silicon infiltration.

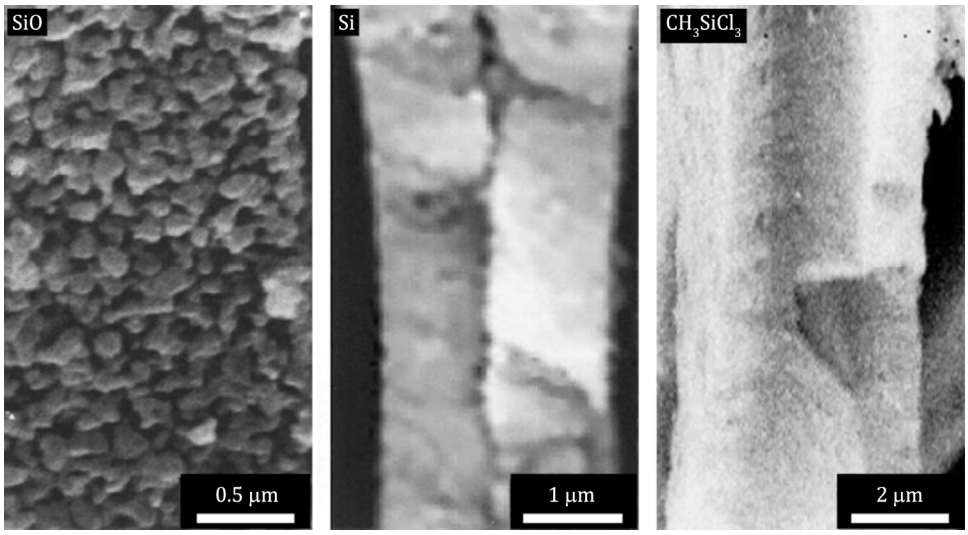

Figure 2.19. High-magnification micrographs of the cell walls of the pine wood-derived SiC in Figure 2.18 produced by the gas-infiltration of SiO, Si, and CH_3SiCl_3 (Greil *et al.* 2002).

energy than sintering processes, the multitude of different wood species allows for tailored microstructures, and near-net-shape parts can be produced with little or no machining of the SiC. These advantages make processing composites using melt-infiltration techniques easier due to eliminating the need for binders, sintering, or other complexities involved in making cohesive preforms (Mortensen *et al.* 1993).

The mechanical properties of wood-derived SiC were found to depend not only on porosity (Greil *et al.* 1998b; Martinez-Fernandez *et al.* 2000; Singh *et al.* 2002; Varela-Feria *et al.* 2002) but also on the spatial distribution of porosity (Kaul *et al.* 2006). In general, the stiffness and strength of the SiC decreased with increasing porosity, but woods with dense regions, which result in increased amounts of residual carbon, had reduced mechanical properties. Accordingly, increasing the LMI reaction time decreased the amount of residual carbon and increased both the flexural strength and fracture toughness of the SiC (Hou *et al.* 2007). These properties were highly anisotropic, being far less in the transverse directions. The thermal conductivity of the SiC was also found to be anisotropic and strongly dependent on both porosity and precursor wood (Pappacena *et al.* 2007).

2.4. Summary

Monolithic materials are increasingly being replaced by composite materials that can provide superior properties at lower weights. Metal/ceramic composites are attractive due to their high strength and stiffness, low weight and, by using melt-infiltration, the ease with which complex near-net-shape parts can be produced. Three-dimensionally interconnected porous ceramics, such as wood-derived ceramics, have gained attention

due to the wide variety of possible microstructures, porosities, and ceramic materials that can be made using economical processing techniques. The wood-derived ceramics are being considered for a wide range of applications, including as the reinforcement in composite materials.

3. Aluminum/Silicon Carbide Composites: Processing & Microstructure

3.1. Introduction

The typical morphology of an aluminum (Al) and silicon carbide (SiC) composite is a metal-matrix composite (MMC), which consists of a continuous Al phase surrounding a discontinuous SiC phase in the form of particles, whiskers, or fibers (Chawla 1998). The addition of SiC to the Al can improve the stiffness, strength and creep resistance, but composite production methods are often more expensive. Despite the cost increase, Al/SiC MMCs are used in a wide-range of industries including aeronautical, automotive and sports for applications such as wing panels, bearings and bicycle frames (Eliasson *et al.* 1995).

In contrast to traditional MMCs, this chapter and the next focus on Al/SiC composites with a continuous SiC phase surrounding a discrete Al phase. This chapter describes the experimental procedures used to produce the Al/SiC composites and characterize their microstructure. The processing of two wood precursors into SiC and the melt-infiltration of two aluminum alloys are described. The microstructure of the wood, carbon, and SiC are also discussed.

3.2. Wood-Derived Silicon Carbide

3.2.1. Processing

Two hardwoods were converted to SiC: beech (*Fagus sylvatica*), a semi ring-porous hardwood, and sapele (*Entandrophragma cylindricum*), a diffuse-porous hardwood. The process to manufacture the SiC involved first pyrolyzing the wood in an argon atmosphere at 1000°C for one hour. Next, the resulting amorphous carbon was heated in vacuum to

1550°C for another hour with a stoichiometric excess of silicon powder (99.6 wt.% Si). Once molten, the silicon reacted with the carbon to form β-SiC. This reaction promoted wetting, and the silicon was wicked into the cylindrical pores. If necessary, this reaction step was repeated to minimize the amount of residual carbon in the specimens. Upon solidification, some pores retained excess silicon, which was removed by etching the samples for at least 14 days in an acid solution consisting of 50:50 vol.% concentrated hydrofluoric and nitric acids.

3.2.2. Experimental Methods

Archimedes' Method

The density and porosity of a specimen can be measured using the density of a known liquid, usually water, and the Archimedes method. In this technique, the mass of a specimen is measured dry, suspended under the liquid and saturated in the liquid (ASTM 1988). After measuring the dry mass, D, the sample is boiled in water to infiltrate the open porosity with water. The suspended mass, S, is measured by placing the sample in a submerged basket, the mass of which is tarred. The saturated mass, M is measured after removing excess water droplets from the surface of the specimen. By assuming the density of water at room-temperature to be 1 g/cm^3, the bulk density, B, apparent specific gravity, (density of impermeable material), T, and apparent porosity (open porosity), P, can be calculated as

$$B = \frac{D}{M - S} \tag{3.1a}$$

$$T = \frac{D}{D - S} \tag{3.1b}$$

and,

$$P = \frac{M - D}{M - S} \times 100\% \tag{3.1c}$$

Mercury Intrusion Porosimetry

Due to the non-wetting nature of most materials by mercury, mercury intrusion porosimetry is used to measure the pore-size distribution of materials. A cylindrical pore is infiltrated with mercury according to the Washburn equation (Equation 2.13) (Washburn 1921). Typical values of γ and θ for mercury are 0.485 N/m and 130°, respectively. The pore-size distribution of a material is calculated by recording volume changes of mercury associated with a small increase in pressure. As the pressure increases, smaller pores are filled with mercury, and the change in mercury volume is attributed to filling pores of diameter, d,

$$d = \frac{-4\gamma \cos(\theta)}{p} \tag{3.2}$$

From these data, the bulk density, B, apparent porosity, P, and apparent specific gravity, T, from Equation 3.1 can also be measured. The major drawback of mercury porosimetry is the underlying assumption that the porosity is composed of cylinders each having a uniform radius along their length. The intrusion of non-uniform cylinders is affected by the shape of the pores and the size of throats or necks between voids (Zgrablich *et al.* 1991).

For the current work, representative volumes of the beech (BE) and sapele (SA) C and SiC were studied with an Autopore IV mercury porosimeter (Micromeritics, Norcross, GA). The amounts of carbon and SiC were typically ≈ 1 g and ≈ 2 g, respectively. The data output included the cumulative intrusion (mL/g), incremental intrusion (mL/g), total porosity (%), and total intrusion volume (mL/g) as a function of applied pressure. From these data, the incremental and cumulative pore volume fractions were calculated according to

$$\text{Intrusion Fraction(p)} = \frac{\text{Intrusion (p)}}{\text{Total Intrusion Volume}} * \frac{\text{Total \% Porosity}}{100} \qquad (3.3)$$

where Intrusion Fraction(p) was either the incremental or cumulative volume fraction at pressure, p, associated with the corresponding amount of incremental or cumulative intrusion at p, Intrusion(p). These data were plotted as a function of pore diameter by using Equation 3.2 and the previously stated values of γ and θ.

3.2.3. Microstructure

Representative micrographs of both the axial and radial sections of BE- and SA-derived C and SiC are shown in Figure 3.1(a)-(d) and (e)-(h), respectively. The replicated wood characteristics, including the cell types, are most evident in the carbon cross-sections. The axially-oriented pores propagate into and out of the page in the axial sections and vertically in the radial sections. The radially-oriented pores are vertical in the axial sections and run into and out of the page in the radial sections. In Figure 3.1a, the radial pores, indicated by the vertical arrow, intersect a relatively dense horizontal band, indicated by the horizontal arrow that separates the late wood (bottom) from early wood (top). The features of SA-

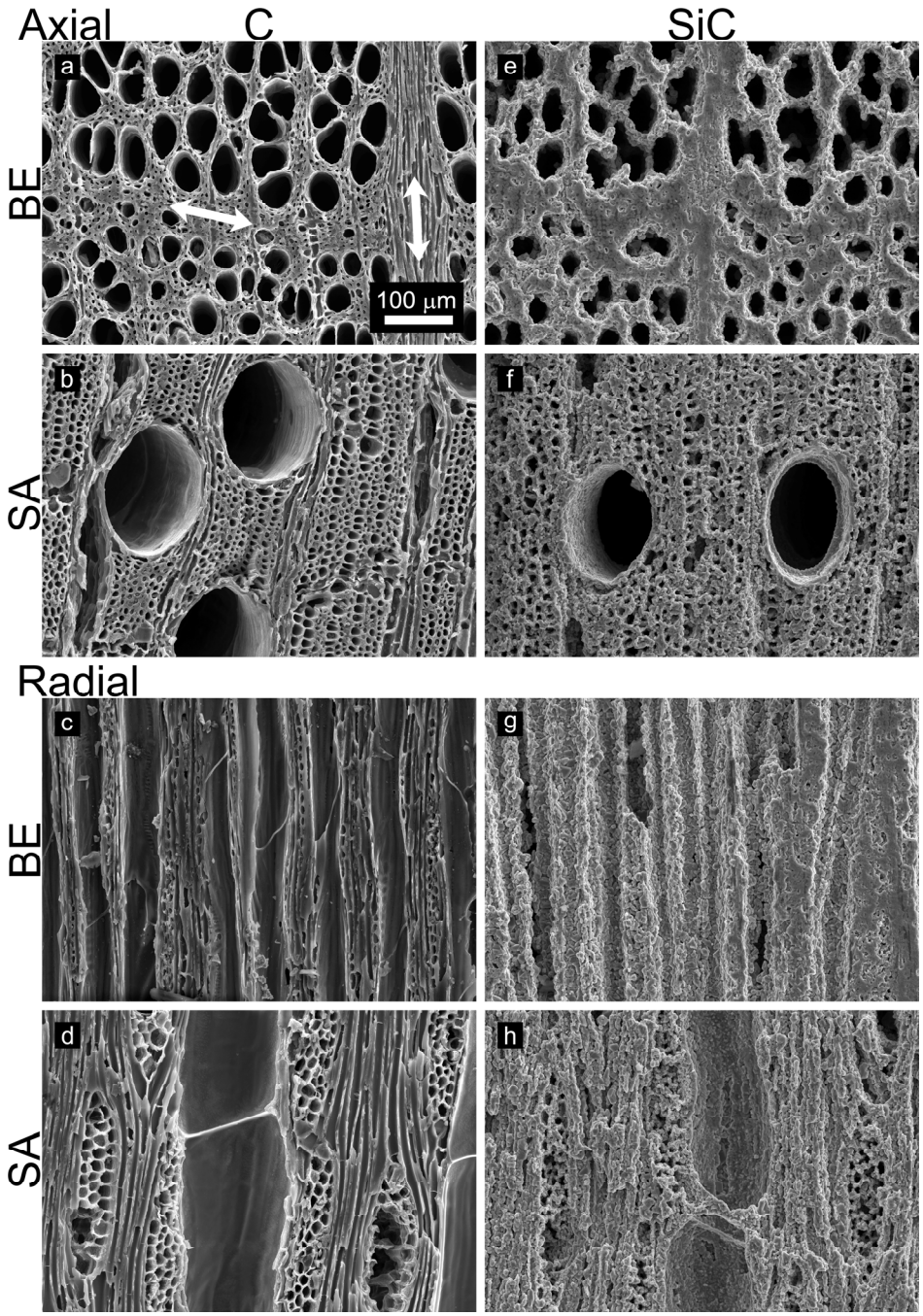

Figure 3.1. SEM micrographs of the BE- and SA-C and -SiC. Cross-sections are perpendicular to either the axial direction (top) or radial direction (bottom). BE and SA micrographs are on the top and bottom of each half, respectively, and the columns depict, from left to right, the C and SiC. In (a), the vertical arrow indicates the band of radially-oriented pores and the horizontal arrow separates the late- and early wood.

derived specimens are generally larger than the BE counterparts, but the late- to early wood transitions are less distinct because sapele is diffuse porous as opposed to the semi-ring porous beech structure.

Upon conversion to SiC, the reaction between molten silicon and amorphous carbon to form SiC was accompanied by a volume change of about 50% (Wang *et al.* 2004). While the overall specimen dimensions did not significantly change, the volume change was accommodated within the pores. This resulted in decreased pore diameters, but some of the pore walls in the BE specimens were damaged, which led to some effectively larger pores (Figure 3.1e), due to the dissolution/precipitation reaction mechanism. Most of the smaller diameter pores were no longer present in the BE-SiC (Figure 3.1e, g) but were observed in the SA-SiC (Figure 3.1f, h). Measurements of the pore size distributions, shown in Figure 3.2, confirmed these observations: the peaks representing porosity smaller than 1 μm in the C curves almost completely disappeared once the material was converted to SiC. Each curve represents the data from one sample, but the curves were reproduced with multiple samples from different batches of C or SiC material. The peak centered about 5 μm in the SA-SiC curve may represent pores formed as a result of damaged pores combining to form effectively larger pores as was seen with the larger-diameter BE porosity.

A one-hour hold at 1550°C was insufficient to completely convert the entire C scaffold into SiC for some of the sample sizes used in this study. As carbon in a smaller pore reacted and the pore closed due to the volume expansion, a barrier was formed, which impeded further reaction to form the SiC. Most of the residual C was converted to SiC after repeating

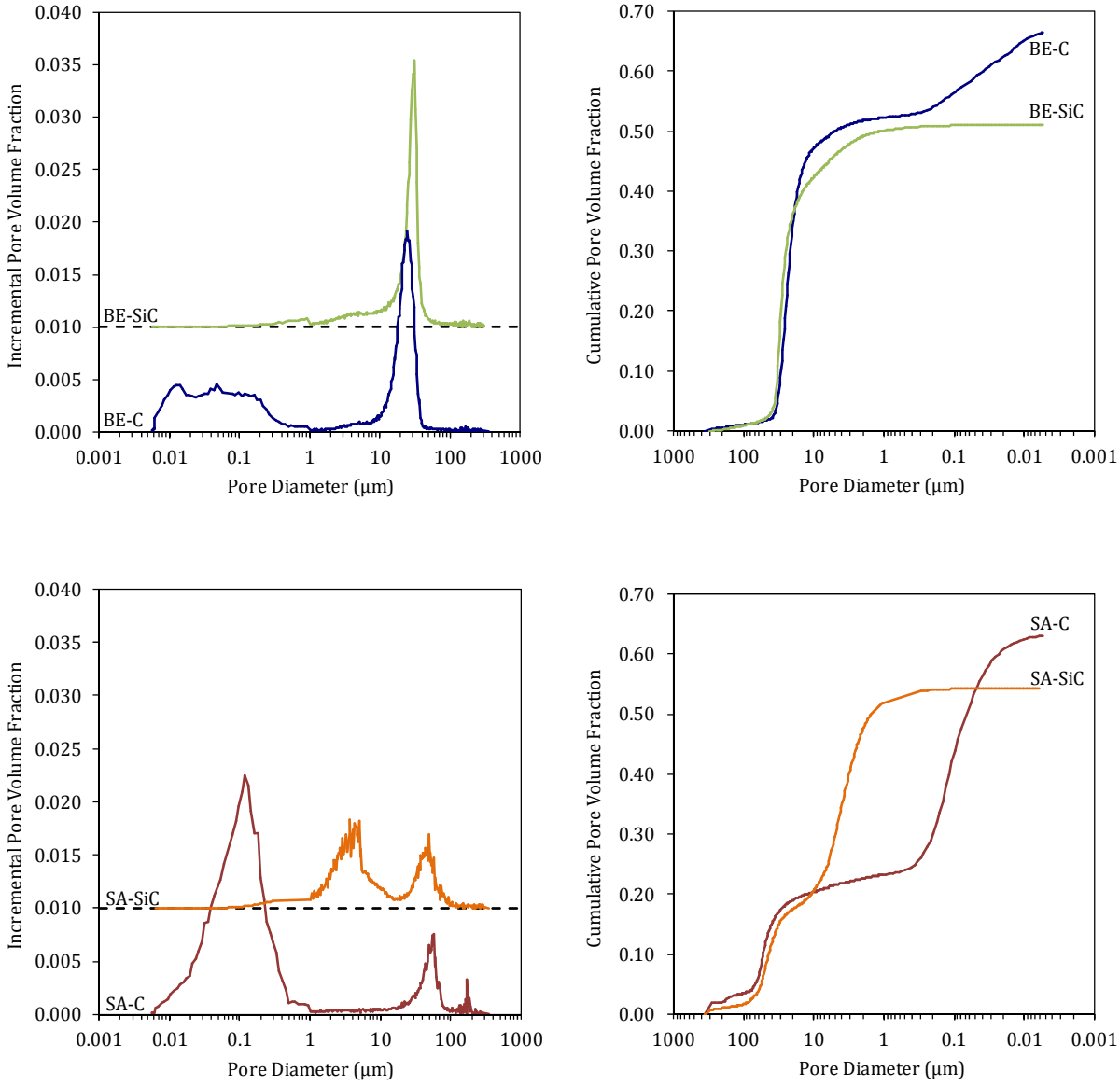

Figure 3.2. Representative plots of the (left) incremental and (right) cumulative pore volume fraction versus pore diameter, measured by mercury intrusion porosimetry, of the (top) BE-C and -SiC and the (bottom) SA-C and -SiC. For clarity, the incremental SiC curves are offset vertically by 0.01.

this reaction step. Small amounts of residual carbon were observed in both specimen types. Based on the theoretical SiC density of 3.21 g/cm^3, Archimedes' density measurements of the BE- and SA-SiC specific gravity, shown in Table 3.1, indicated an upper bound of 4 vol.% residual carbon. This is an upper bound because the Archimedes calculation of specific gravity does not distinguish closed porosity from solid material. Therefore, the combination of closed porosity and residual carbon accounts for no more than 4% of the total sample volume in this batch of samples.

Table 3.1. Apparent porosity and specific gravity of the BE- and SA-SiC as measured by Archimedes' method (ASTM 1988).

	Apparent Porosity (%)	Apparent Specific Gravity (g/cm^3)
BE-SiC	50 ± 3	3.14 ± 0.02
SA-SiC	51 ± 3	3.18 ± 0.03

3.3. Infiltration of A356 (Al - 7 wt.% Si)

Initial pressureless infiltration experiments of the porous wood-derived SiC used a commercially-available aluminum alloy, A356, which contains approximately 7 wt.% Si and 0.35 wt.% Mg. The A356 used in this work was donated by Prototype Casting, Inc (Denver, CO). The pressureless infiltration experiments were conducted in a horizontal tube furnace equipped with an alumina tube and end caps that allowed the use of either a vacuum or inert gas atmosphere. Within an alumina crucible, a billet of the A356 alloy measuring approximately 8.0 x 8.0 x 10 mm^3 was placed on a piece of wood-derived SiC measuring approximately 10 x 10 x 3.0 mm^3. A ramp rate of 10°C/minute was used to reach a

temperature of either 800°C or 900°C, which was held for either 60 or 120 minutes. These conditions are summarized in Table 3.2.

Table 3.2. Conditions used for the pressureless A356 infiltration of the wood-derived SiC.

Atmosphere	Temperature (°C)	Hold Time (min.)
Argon	800	60
	900	
Vacuum	800	60
Nitrogen	900	120

Unfortunately, all of the experiments were unsuccessful: while there was clear evidence that the aluminum melted, it did not wet or infiltrate the porous SiC. This was unexpected because, even though additions of up to 12 wt.% Si were shown to have little effect on the wetting angle of Al on SiC, the contact angle between Al and SiC was shown to be below 90° after a 30 minute hold at temperatures above 725°C in vacuum (Han *et al.* 1993). This indicated that an Al_2O_3 skin could have acted as a barrier and prevented the molten aluminum from wetting and infiltrating the wood-derived the SiC (Mortensen *et al.* 1992). While temperatures greater than 900°C could have been used in an attempt to vaporize the alumina layer, the experimental conditions were such that, according to Figure 3.3, the formation of the brittle intermetallic compound Al_4C_3 was likely even at 800°C (Rajan *et al.* 1998).

Clearly, a pressurized infiltration process was the solution: lower temperatures and gas-pressure could be used to avoid Al_4C_3 formation and force infiltration, respectively. A gas-pressure liquid-metal infiltration furnace (Blucher 1992; San Marchi *et al.* 2003),

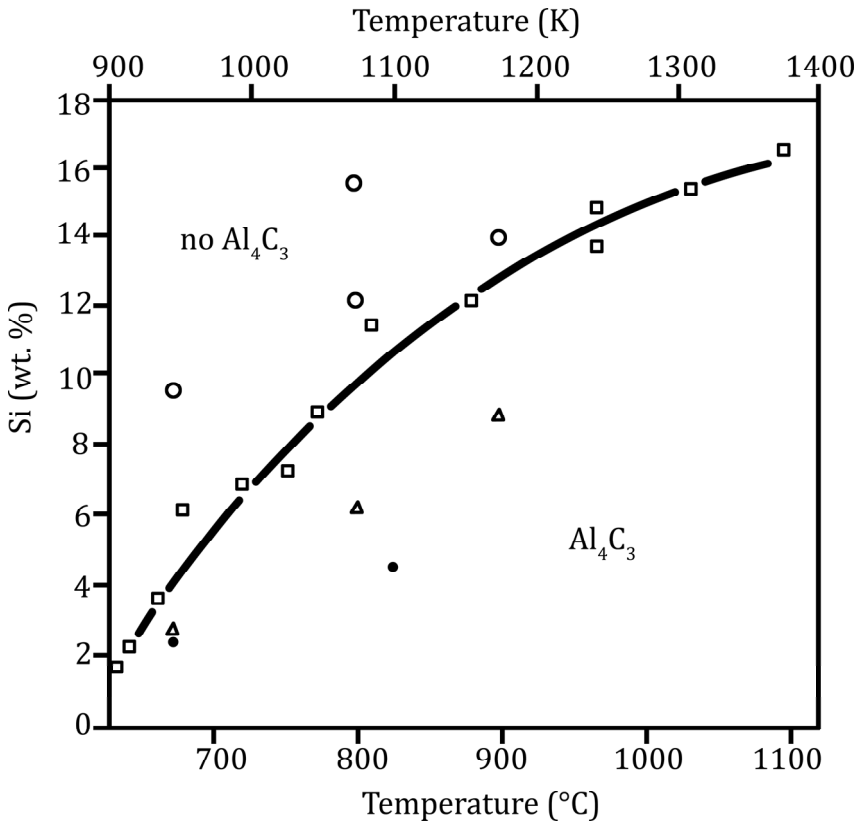

Figure 3.3. The effect of temperature and weight percent silicon in Al-Si alloys on the formation of aluminum carbide (Al_4C_3) (after Rajan *et al.* 1998).

shown schematically in Figure 3.4, was used for pressurized melt-infiltration. The samples were held in place with a piece of machined graphite. A cylinder of the A356 alloy, which had been cast to shape in an ambient atmosphere, was placed on top of specimens in a graphite crucible. The furnace was heated to 750°C in vacuum whereupon the molten aluminum alloy had formed a seal with the crucible walls, isolating the porous SiC in a vacuum environment. The furnace was then pressurized, using ultra-high-purity argon, to 3.5 MPa to force the metal into the pores.

A representative cross-section of the resulting SA-MCC material is shown in Figure 3.5. While some of the pores were infiltrated with metal, the residual porosity was still significant: 37 ± 6%. Despite the use of multiple pressureless infiltration conditions and multiple gas-pressurized infiltration attempts, neither technique resulted in complete A356 infiltration of the wood-derived SiC. At this point, other techniques that would improve the Al/SiC wetting were considered; mainly using a different aluminum alloy. In aluminum systems, alloy additions are designed to either react with the reinforcement or disrupt the Al_2O_3 layer (Skibo *et al.* 1988; Mortensen *et al.* 1992). Alloying additions of magnesium have been shown to weaken the alumina layer, which in turn allows the molten aluminum to come into direct contact with and wet the SiC (Han *et al.* 1993). An alloy containing 13 wt.% Si and 9 wt.% Mg has been shown to optimize the contact angle, surface tension and driving force for wetting (Pech-Canul *et al.* 2000a). The magnesium acts to weaken the alumina layer through three possible reduction reactions

$$3Mg_{(l)} + Al_2O_{3(s)} \rightarrow 3MgO_{(s)} + 2Al_{(l)} \qquad (3.4a)$$

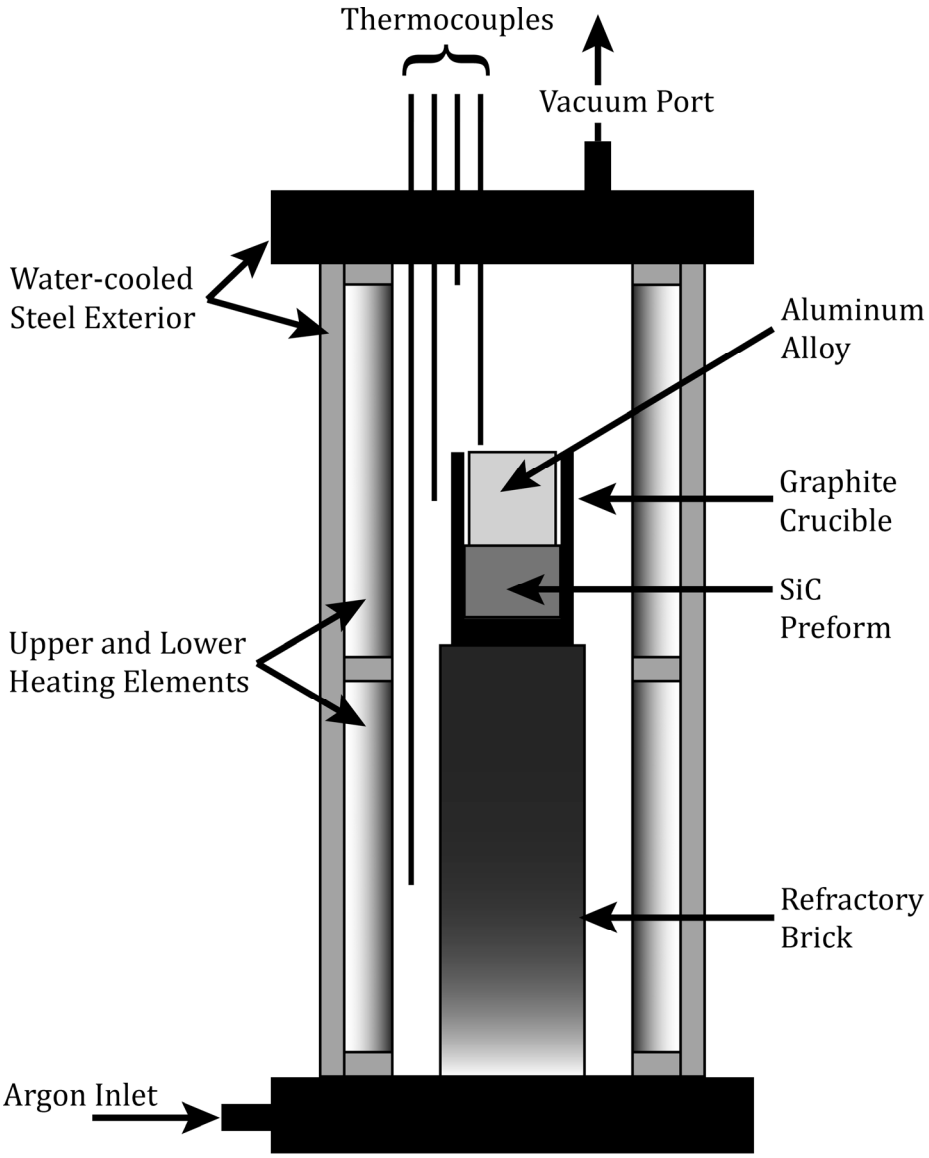

Figure 3.4. Schematic of the gas-pressure assisted liquid-metal infiltration furnace used to infiltrated aluminum into the wood-derived SiC preforms.

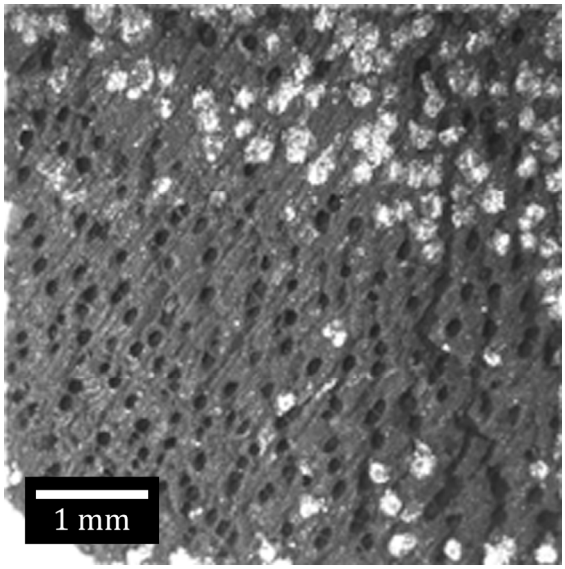

Figure 3.5. Optical stereomicrograph of the axial section of an A356 pressure-infiltrated SA-SiC composite. The aluminum alloy (light gray) only partially infiltrated the SiC preform (dark gray).

$$Mg_{(l)} + 2Al_{(l)} + 2O_2 \rightarrow MgAl_2O_{4(s)} \quad (3.4b)$$

and

$$3Mg_{(l)} + 4Al_2O_{3(s)} \rightarrow 3MgAl_2O_{4(s)} + 2Al_{(l)} \quad (3.4c)$$

and results in direct contact between the Al and SiC after the oxide is broken.

3.4. Infiltration of Al-Si-Mg (Al - 13 wt.% Si - 9 wt.% Mg)

An alloy, which contained 13 wt.% Si and 9 wt.% Mg, was made by adding appropriate amounts of Al-Si and Al-Mg master alloys (both 50:50 wt.%) to the A356 alloy. The three metals were placed into an alumina crucible, heated to 700°C in air, stirred to promote mixing and then cast to shape. The sample specifications for the pressureless infiltrations were the same as those used for the A356 alloy. The specific atmosphere, temperature and holding time were nitrogen, 900°C and 60 minutes, respectively. These conditions were similar to the Lanxide Corporation's PRIMEX™ pressureless metal infiltration process (White *et al.* 1989; Schiroky *et al.* 1997) in which the nitrogen atmosphere reacts with evaporating magnesium to form a nitride that then reacts with the molten aluminum via

$$Mg_3N_2 + 2Al \rightarrow 2AlN + 3Mg \quad (3.5)$$

to reintroduce Mg into the alloy. The cyclical process is said to induce wetting and pressureless infiltration of the SiC preform (Zulfia *et al.* 2002).

Like the A356 infiltration experiments, these too were unsuccessful and indicated that an alumina skin was still preventing contact between the metal and ceramic. Pressurized infiltration experiments, however, showed promise. A representative cross-section of a BE-MCC, Figure 3.6, depicts the partial infiltration that occurred. Pores corresponding to

the early wood were consistently infiltrated, but the late wood remained uninfiltrated. This suggested that complete infiltration could be accomplished by increasing the temperature, amount of magnesium or gas pressure.

As the magnesium alloy was expected to infiltrate the SiC without the use of gas-pressure, a closer look was taken at the process used to make the alloy. During processing in air and upon initial melting, a black reaction product was observed within the melt. Energy dispersive X-ray spectroscopy showed the presence of Mg, Al, and oxygen, which corresponds to the formation of $MgAl_2O_4$ via Equation 3.4b. The occurrence of this reaction reduced the amount of magnesium in the aluminum alloy and it was hypothesized that this affected the wetting characteristics enough to prevent complete infiltration. To test this theory, a batch of the Al-Si-Mg alloy was first mixed in an inert argon atmosphere. Metal in an alumina crucible was melted for one hour, to promote diffusion of the Mg and Si, under a slow and constant flow of argon. As mechanical mixing was not possible, the resulting billet was cut into halves, which were stacked on top of each other, and the process was repeated. This promoted mixing and, after a total of two or three heating cycles, resulted in a qualitatively homogeneous billet, which was then melted and cast to shape in air without the formation of $MgAl_2O_4$.

Results of the pressureless infiltration of this alloy into the BE-SiC are shown in Figure 3.7. It is clear that $MgAl_2O_4$ formation had an effect on the Al/SiC wettability: in some cases the smallest porosity was infiltrated without the aid of gas-pressure. These results still showed varying levels of success; some samples remained uninfiltrated while others were infiltrated through the entire 3.0 mm sample thickness. Gas-pressure

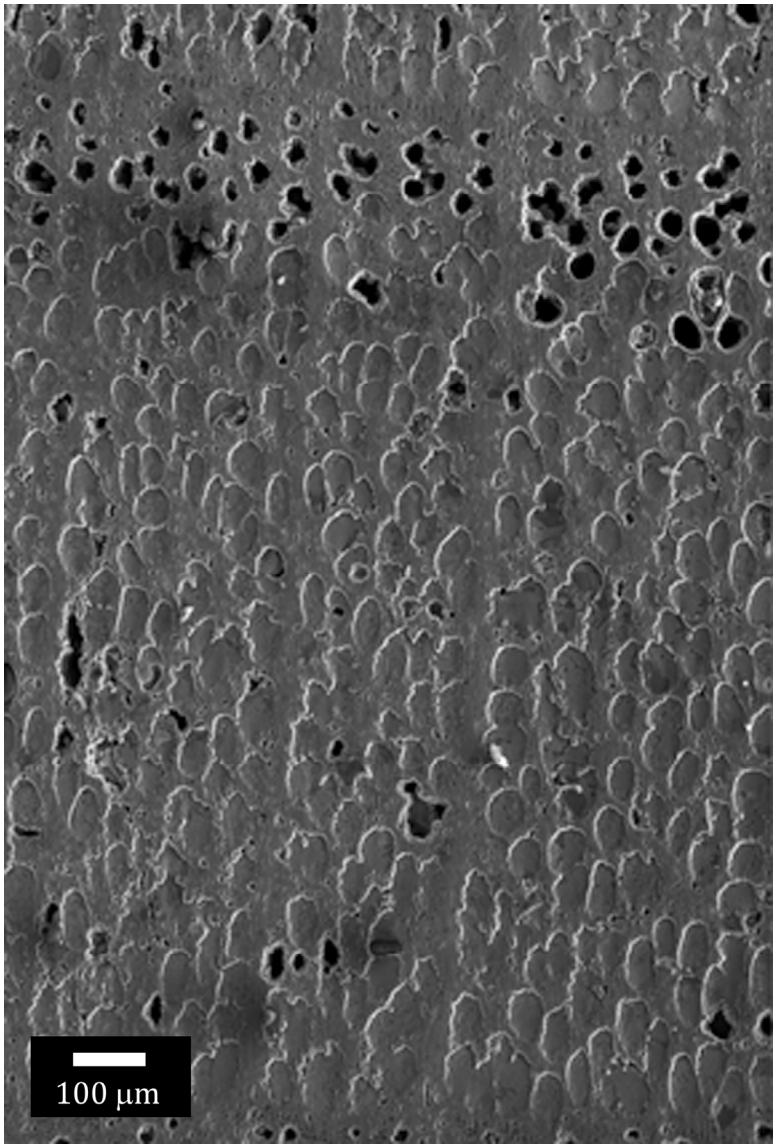

Figure 3.6. SEM image of a pressure-infiltrated Al-Si-Mg/BE-SiC MCC. While the early wood regions (lower and extreme top) were infiltrated, the late wood regions (black) were devoid of metal.

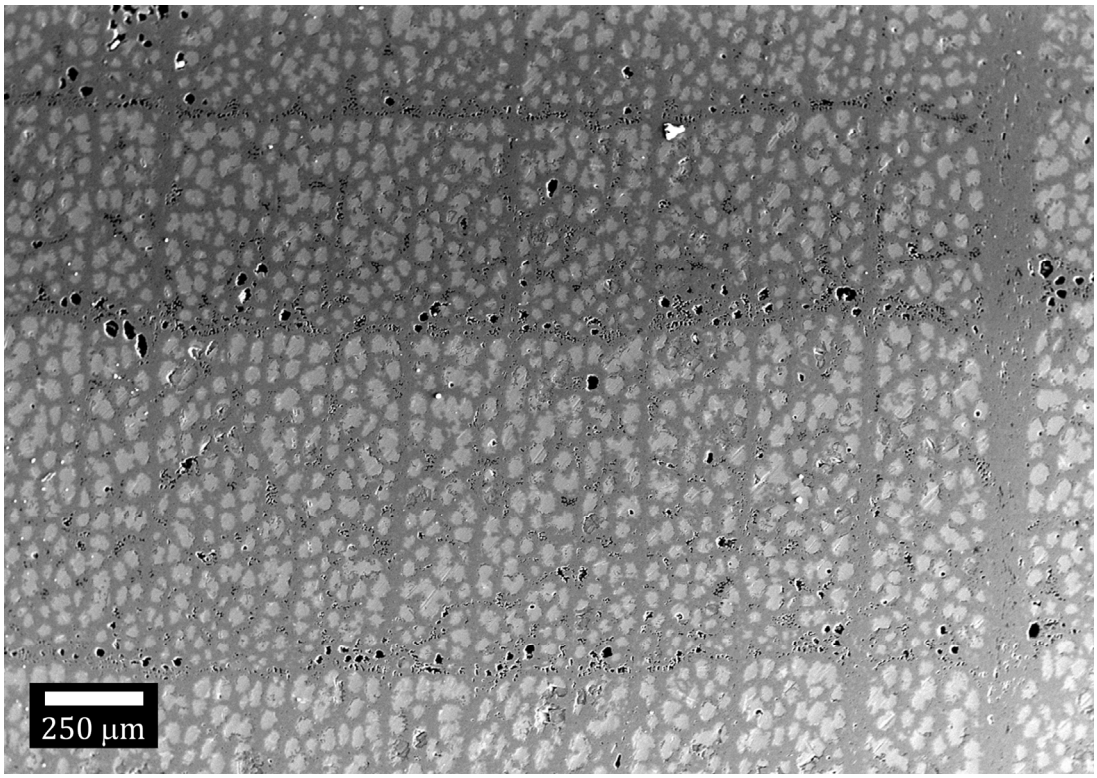

Figure 3.7. SEM image of a pressureless-infiltrated Al-Si-Mg/BE-SiC MCC. Premixing the Al-Si-Mg alloy in argon before casting prevented the formation of $MgAl_2O_4$ and improved wetting between the Al alloy and the SiC preform.

infiltration was used to circumvent these inconsistencies. Representative back-scattered electron images of the axial and radial planes of these BE- and SA-MCCs are shown in Figure 3.8(a-d). The porosity and specific gravity of both the MCCs and bulk metal, which contained shrinkage porosity, are reported in Table 3.3. The arrows in Figure 3.8c indicate areas of closed porosity corresponding to instances where small-diameter pores were pinched closed due to the volume expansion that occurred during the C → SiC reaction.

Table 3.3. Apparent porosity and specific gravity of the BE- and SA-MCCs and the Al-Si-Mg alloy as measured by Archimedes' method (ASTM 1988).

	Apparent Porosity (%)	Apparent Specific Gravity (g/cm^3)
BE-MCC	4 ± 2	2.84 ± 0.02
SA-MCC	5 ± 3	2.82 ± 0.07
Al-Si-Mg	5 ± 3	2.49 ± 0.04

Higher magnification scanning electron micrographs showed the Al-Si-Mg alloy precipitate structure in both the bulk specimens (Figure 3.9a) and in the composites (Figure 3.9b). The microstructure was made up of a continuous Al phase (light gray) that included both elongated crystals of primary Si (dark gray) and irregularly-shaped Mg_2Si precipitates (black), which were both identified using energy dispersive X-ray spectroscopy. The overall microstructure was similar in both materials and was typical of hypereutectic Al-Si-Mg alloys that were slowly cooled from processing temperatures (Wang *et al.* 2001a). The Si crystals in the bulk alloy were larger than those in the composites because the pore size limited growth in the latter. Also, SiC is known to

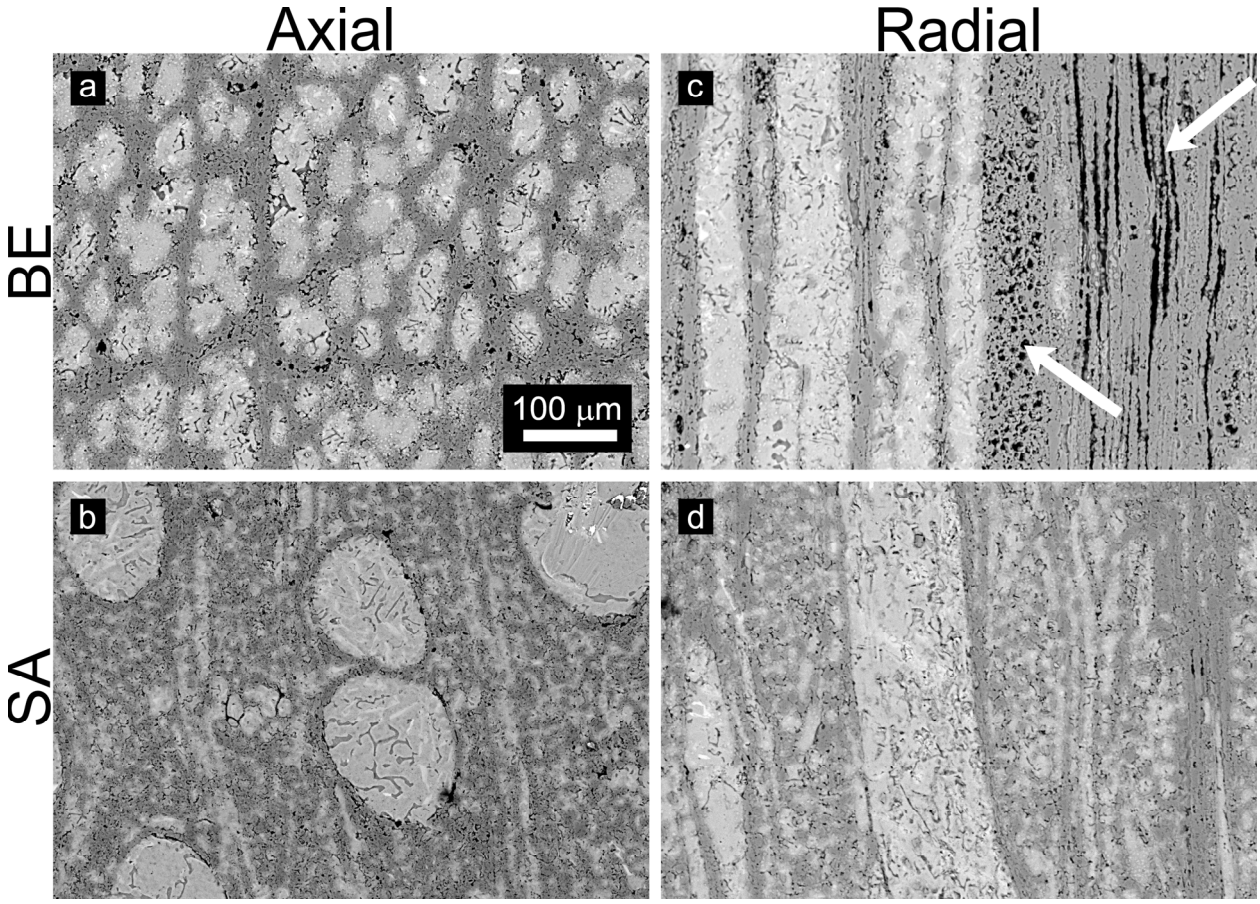

Figure 3.8. Back-scattered electron micrographs of the BE- and SA-MCCs. Cross-sections are perpendicular to either the axial direction (left) or radial direction (right). BE and SA micrographs are on the top and bottom, respectively. In (c), the arrows point to closed porosity oriented in both the radial (left) and axial (right) directions.

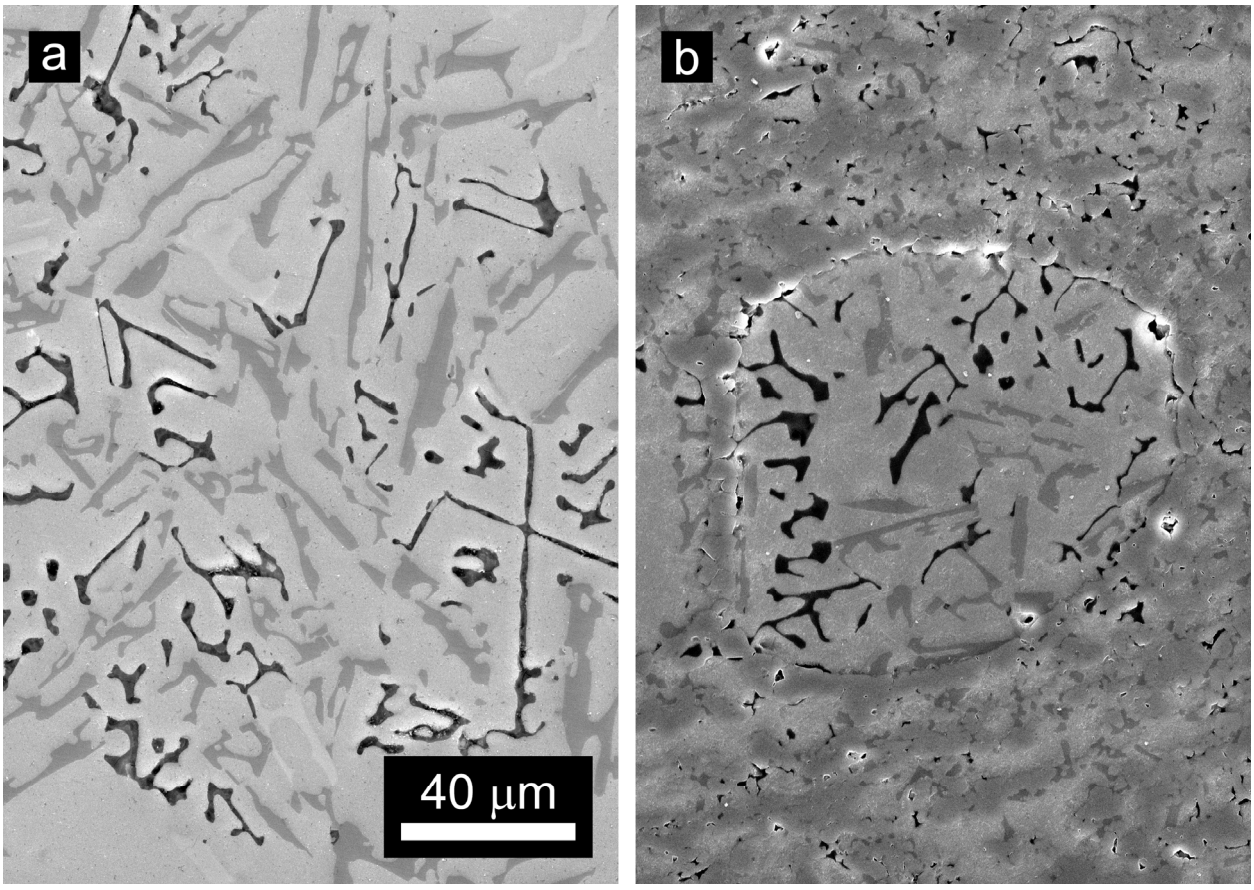

Figure 3.9. SEM micrographs of the Al-Si-Mg microstructure in (a) the bulk metal and (b) the Al-Si-Mg filled pore of a SA-MCC. Large primary Si crystals (dark gray) and Mg_2Si precipitates (black) were observed within the Al matrix (light gray) in both cases.

catalyze the nucleation of Si crystals in composites with hypereutectic Al-Si alloys. This results in grain refinement and a larger number of primary Si crystals per unit volume (Mortensen *et al.* 1992).

3.5. X-ray Microtomography

3.5.1. Introduction

Although it is best known for its use in medical practices, e.g. CAT scans, X-ray microtomography can also be used to non-destructively image the internal microstructure of engineering materials and achieves spatial resolutions on the order of one micrometer (Stock 1999). X-ray microcomputed tomography (μCT) has been extensively used to study composite materials such as SiC-SiC, SiC-Si_3N_4, and Al- and Ti-MMCs. The damage accumulation within particle-reinforced composites has also been studied. The technique has also been used to characterize the properties, such as pore connectivity, of porous materials.

Three-dimensional representations are reconstructed from X-ray attenuation data collected as a sample is rotated 180° about a vertical axis, as shown in Figure 3.10. X-ray microtomography utilizes the fact that X-rays of wavelength λ are attenuated according to

$$\frac{I}{I_0} = \exp(-\mu x) \tag{3.6}$$

where I_0 and I are the initial and attenuated X-ray beam intensities, respectively, transmitted through a material with thickness x and linear attenuation coefficient μ (Cullity *et al.* 2001). By measuring I/I_0 from many different angles, often every 1/10° to 1/8°, the

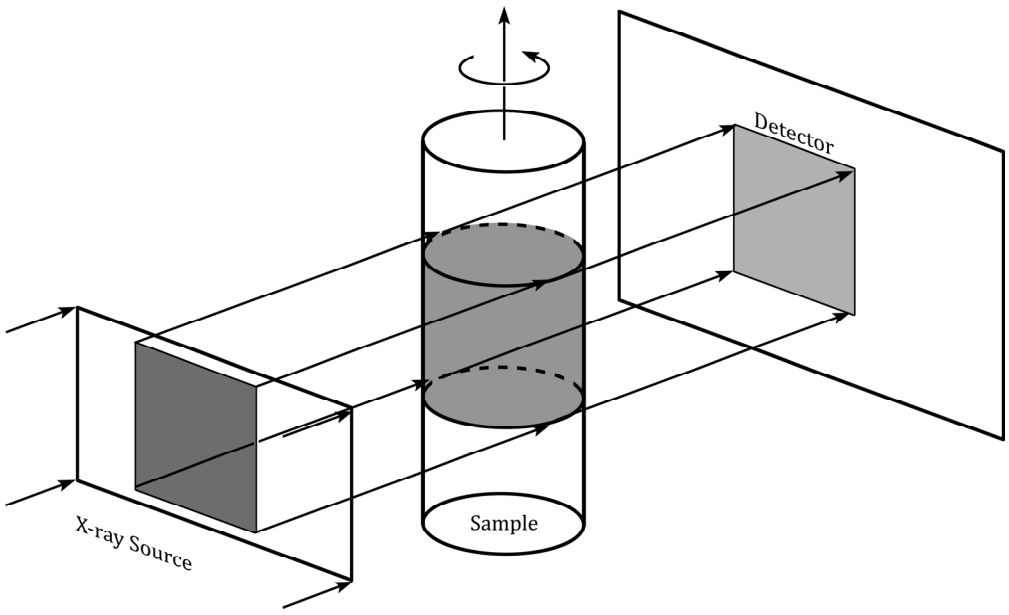

Figure 3.10. Simplified schematic of the μCT experimental setup. A monochromatic X-ray source passes through an aperture before transmitting through the sample. The attenuated signal is collected on a CCD detector at multiple sample rotations (after Stock 1999).

structure and location of features such as cracks, pores or reinforcements can be located within the specimen.

The experimental configuration shown in Figure 3.10 consists of a parallel-beam X-ray source, which shines through the sample, and is collected on a two-dimensional detector. This method results in rapid and simultaneous data collection because the X-ray beam is parallel but it requires a high-energy X-ray source such as synchrotron X-radiation. Allowable sample dimensions, which are typically less than 5.0 mm, are limited by the X-radiation source energy and material attenuation coefficients. A charge-coupled-device (CCD) camera is used as a detector to collect the X-radiation absorption data after the attenuated beam is converted to light using a scintillator.

In the parallel-beam configuration, each instance of data collection corresponds to one projection of the sample. After rotating 180°, the 2-D projections are reconstructed using computer algorithms which convert the vertical projections into horizontal slices of the sample. Each slice is represented by a row of pixels on the CCD detector. The dimensions of a 2-D pixel, or 3-D voxel, depend on the spatial resolution of the configuration. After applying thresholds to the 2-D images to better distinguish between materials, the layers can be combined into 3-D representations of the original sample.

3.5.2. Experimental Methods

Cylindrical samples of the beech wood, C, SiC and Al-Si-Mg/SiC MCC measuring 3 mm in diameter by approximately 10 mm long were machined from bulk materials using an ultrasonic drill press (Branson Ultrasonics Corp, Danbury, CT). Synchrotron μCT was

carried out at bending magnet station 2-BM of the Advanced Photon Source at Argonne National Lab (Argonne, IL) by Stuart R. Stock, Francesco De Carlo and colleagues using the equipment described by Wang *et al.* and shown schematically in Figure 3.10 (Wang *et al.* 2001b; Chu *et al.* 2002). The X-radiation energies were 17.4 keV for the wood and carbon samples and 26.4 keV for the SiC and MCC samples; approximately 750 μm of the length of each sample was studied. The detector consisted of a $CdWO_4$ single-crystal scintillator, a 5x optical lens and a 2048 x 2048 pixel CCD camera; the resulting cubic voxels measured 1.46 μm per side.

The μCT data were displayed in grayscale, and lighter pixels corresponded to voxels with greater linear attenuation coefficients. Segmentation thresholds were applied to the data by James R. Wilson using Photoshop® (Adobe Systems, Inc., San Jose, CA), and the data were reconstructed into 3-D representations using IDL (Research Systems, Inc., Boulder, CO). ImageJ (Rasband 2007) was used to extract numerical quantities from the data. Both the VolumeViewer plugin (Barthel 2006) for ImageJ and Amira® (Visage Imaging, Inc., Carlsbad, CA) were used to display reconstructed 2-D slices. The linear attenuation coefficients of the carbon, silicon carbide, and aluminum alloy were calculated from the carbon, SiC, and Al/SiC samples, respectively, by dividing the ImageJ grayscale value by the voxel dimension (1.46×10^{-4} cm). The coefficients were calculated from averages of 25 regions in each sample, five each from five random slices through the 750 μm sample thickness.

3.5.3. Results

Representative axial cross sections of the reconstructed data for the four samples are shown in Figure 3.11. The calculated linear attenuation coefficients, μ, of the C, SiC, and Al-Si-Mg alloy were 0.8 ± 0.4 cm^{-1}, 3.4 ± 0.6 cm^{-1} and 3.3 ± 0.5 cm^{-1}, respectively. The similarity between the linear attenuation coefficients of the Al alloy and SiC made differentiating between these phases difficult and prohibited thresholding and 3-D reconstruction. On the other hand, the distinction between pores and solid material was clear in the wood, carbon and SiC samples. Representative 3-D reconstructions of the wood, carbon and SiC are shown in Figure 3.12. As some of the finer microstructural details were lost during the segmentation processing, 2-D slices of the data were also reconstructed to correspond approximately to the principle axes (axial, radial, tangential) of the samples (Figure 3.13 through 3.16).

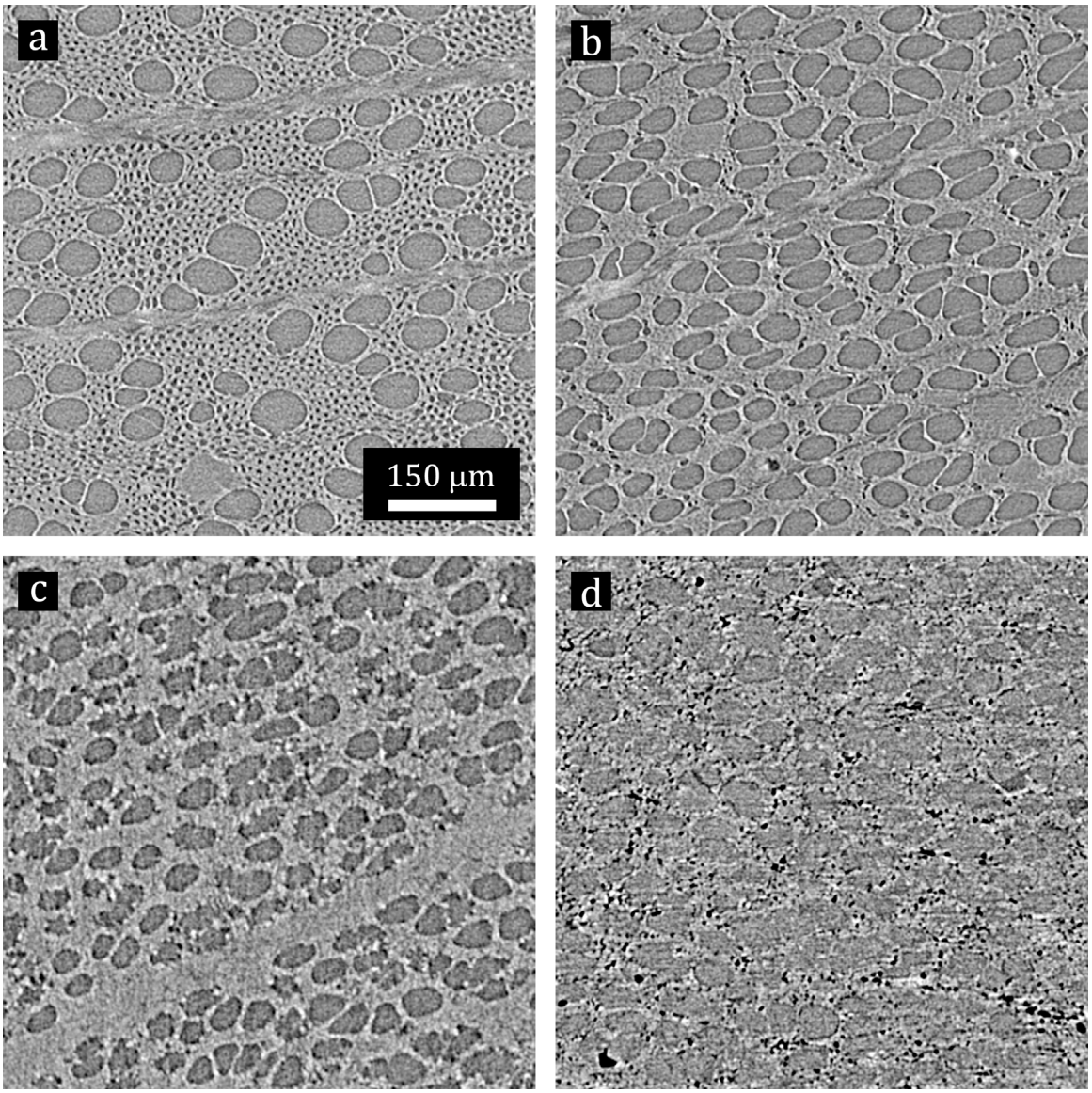

Figure 3.11. Representative axial cross sections of the reconstructed μCT data for the (a) wood, (b) carbon, (c) SiC and (d) Al/SiC MCC.

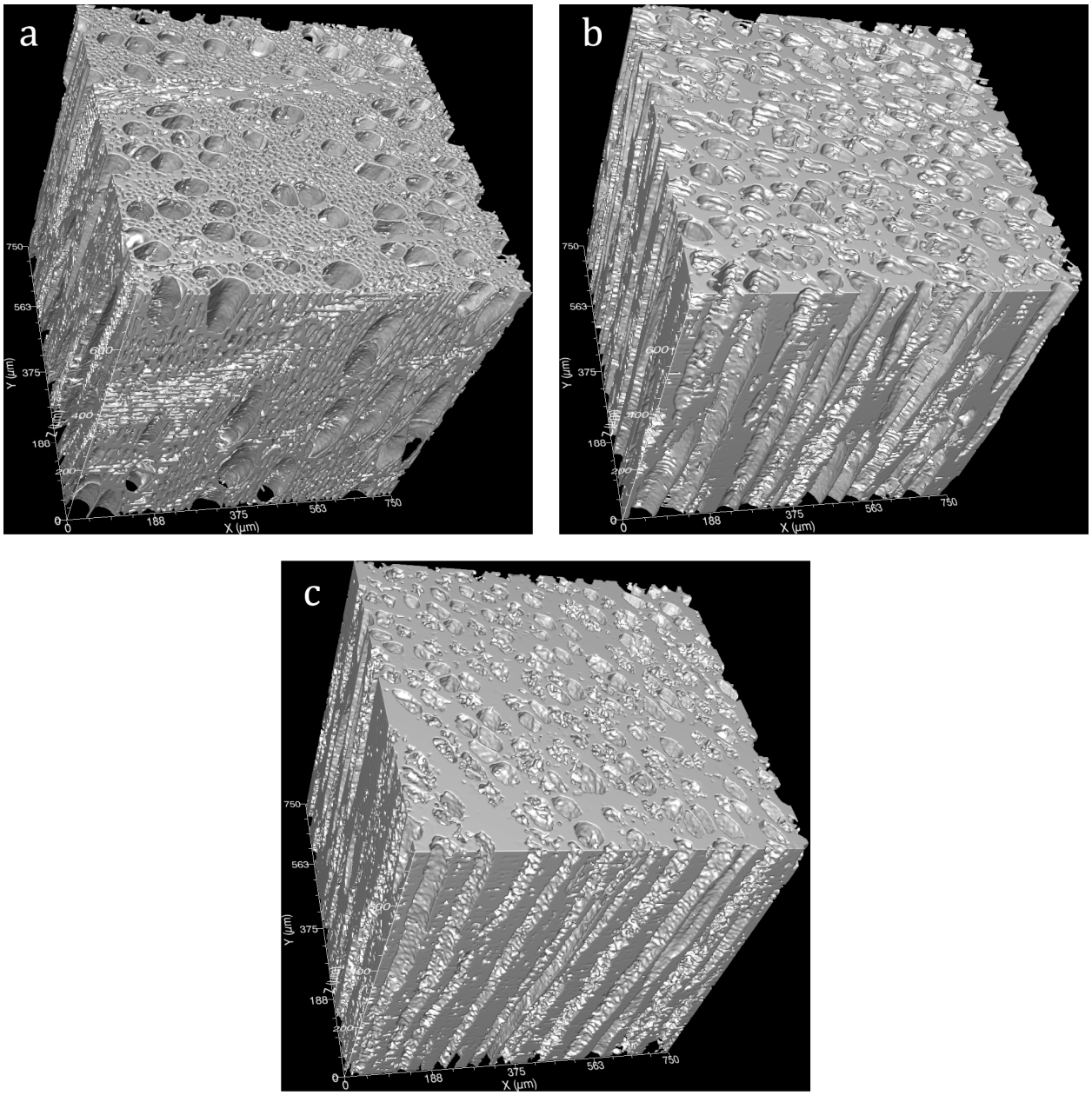

Figure 3.12. Three-dimensional representations, which were reconstructed from the µCT data, of the beech (a) wood, (b) carbon and (c) SiC samples. The cubes measure approximately 750 µm per side.

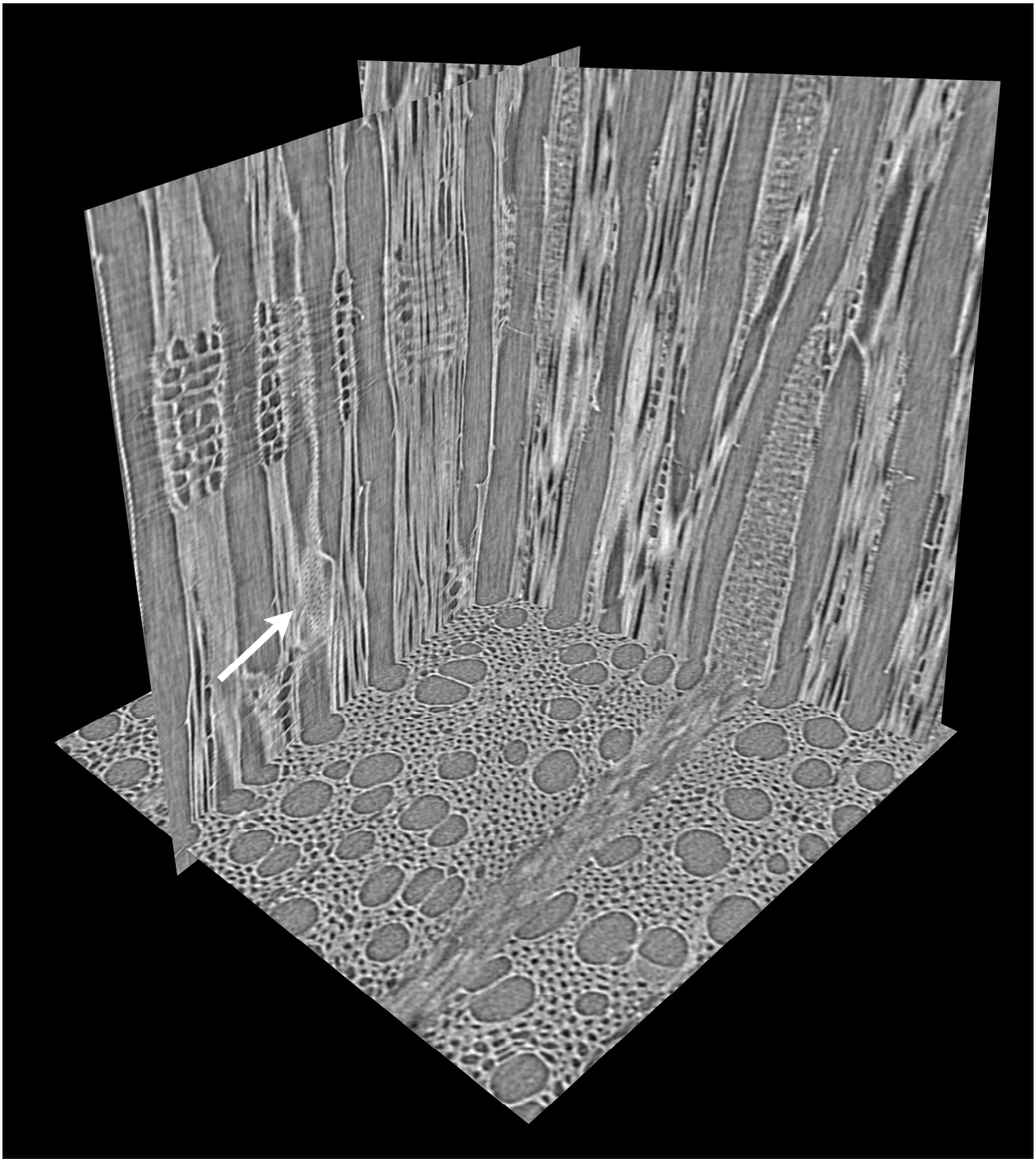

Figure 3.13. Beech wood sample sectioned through three orthogonal planes perpendicular to the axial, tangential (left vertical slice) and radial (right vertical slice) directions. The arrow on the tangential slice points to small-diameter interconnections between the pores. The slice dimensions are approximately 750 μm.

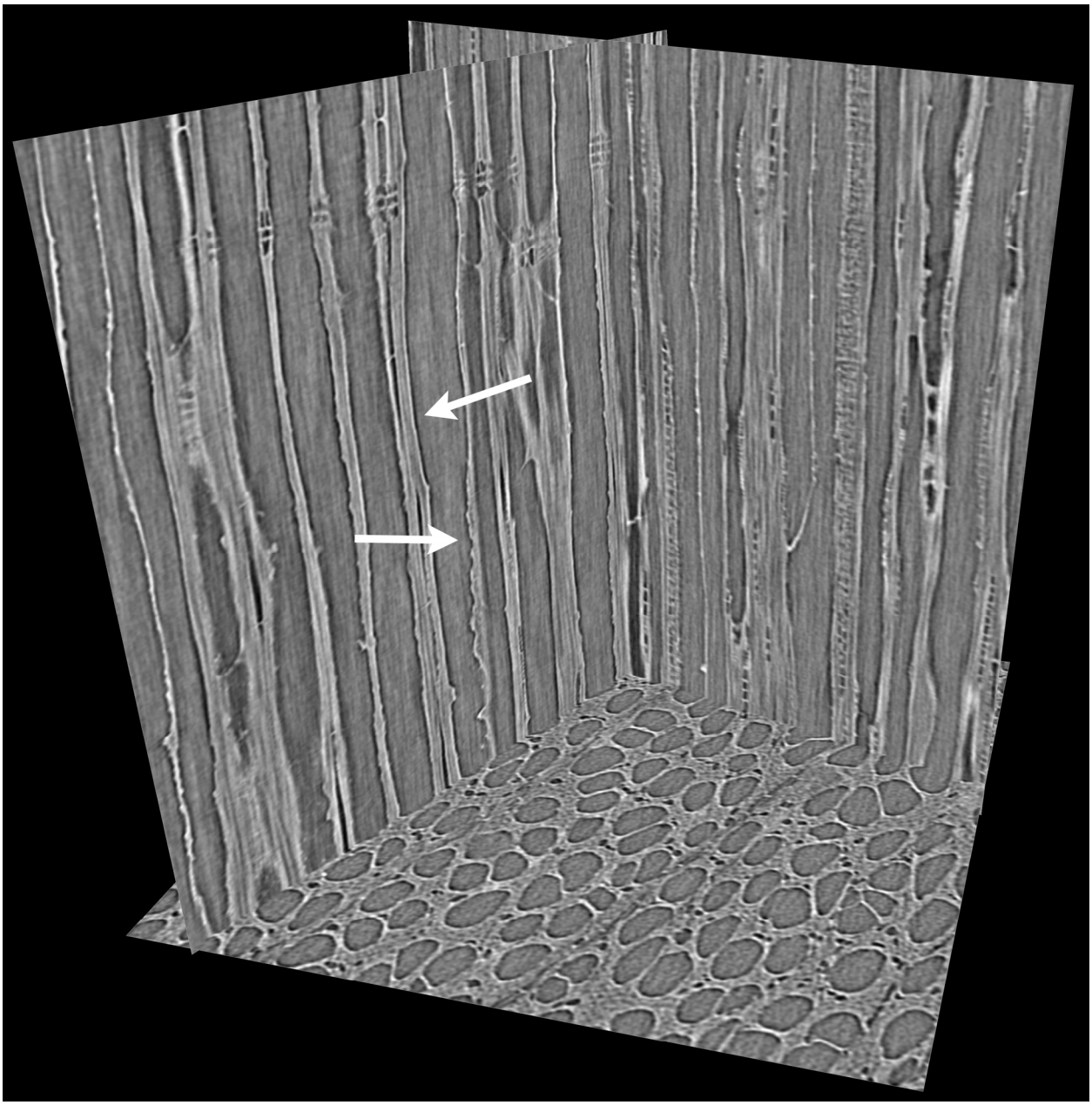

Figure 3.14. Pyrolyzed beech sample sectioned through three orthogonal planes perpendicular to the axial, tangential (left vertical slice) and radial (right vertical slice) directions. The arrows on the tangential slice point to smooth and rough pore-wall regions. The slice dimensions are approximately 750 μm.

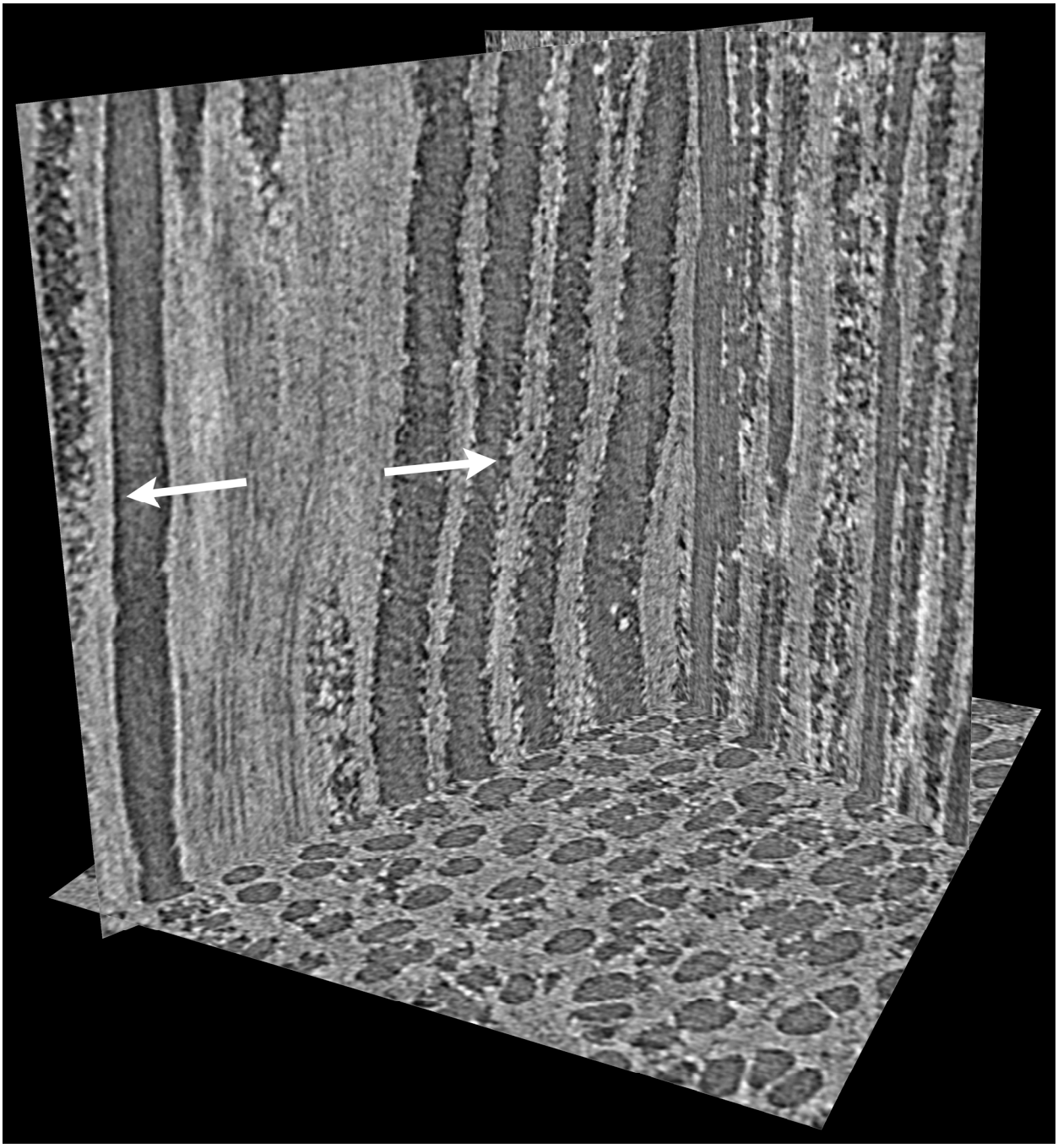

Figure 3.15. Beech SiC sample sectioned through three orthogonal planes perpendicular to the axial, tangential (left vertical slice) and radial (right vertical slice) directions. The arrows on the tangential slice point to smooth and rough pore-wall regions. The slice dimensions are approximately 750 μm.

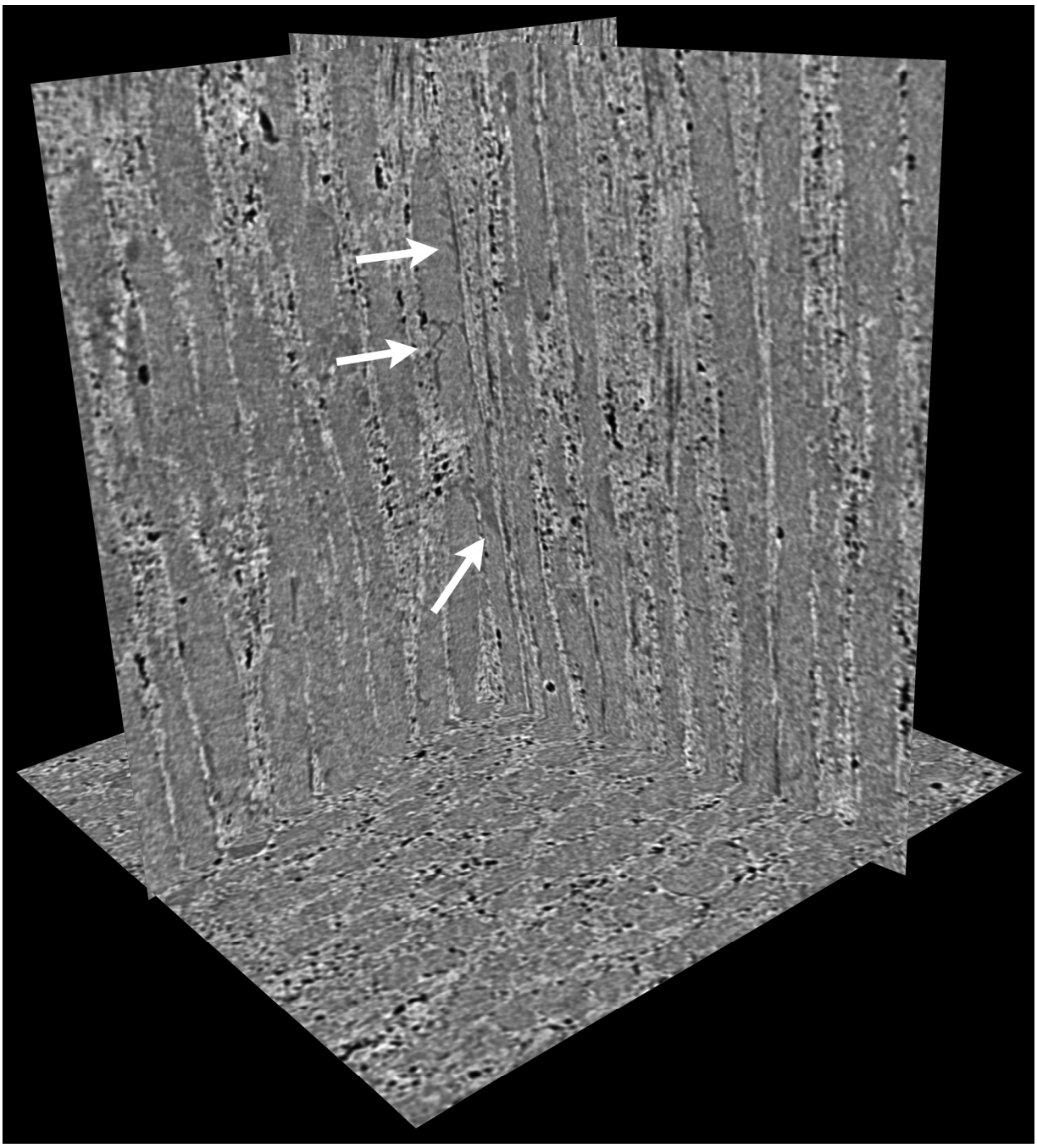

Figure 3.16. Beech-derived Al/SiC MCC sample sectioned through three orthogonal planes perpendicular to the axial, tangential (left vertical slice) and radial (right vertical slice) directions. Residual porosity appears black and the aluminum alloy is slightly darker than the SiC. The arrows on the tangential slice point to precipitates visible in the Al alloy. The slice dimensions are approximately 750 μm.

3.5.4. Discussion

For the X-ray beam energies used, the μ for C (graphite), SiC, and pure Al are 1.1 cm^{-1}, 6.0 cm^{-1} and 5.3 cm^{-1}, respectively (Hubbel *et al.* 2008). The experimental values exhibited large standard deviations; in fact some of the sampled regions exhibited standard deviations that included values of $\mu < 0$ cm^{-1}, which are nonphysical. This has been observed in other μCT studies and is caused by refraction at the Al/SiC interfaces, which artificially alter the collected X-ray attenuation data (Stock *et al.* 2003; Stock *et al.* 2008). Discounting these effects, the difference between the experimental and theoretical attenuation coefficients could be due to electron density differences between the wood-derived amorphous carbon and graphitic carbon, residual porosity and carbon in the SiC, and the Si and Mg_2Si ($\mu = 5.9$ cm^{-1} and 3.8 cm^{-1}, respectively) in the aluminum alloy.

In contrast to microscopy, it was possible to quickly sample large volumes with the μCT data. In addition, the high-resolution that resulted from using high-energy synchrotron radiation reproduced even small details in the studied samples. For example, it is well known that interconnections exist between the cells in wood (Dinwoodie 1989), but observing these in the wood was difficult with optical or electron microscopy. Small-diameter holes were observed in the μCT data and are visible on the tangential section in Figure 3.13. The presence of these interconnections was later confirmed with scanning electron microscopy, shown in Figure 3.17. Microscopy of the carbon also revealed interconnections (Figure 3.17), but they were not observed in the carbon μCT data. This is most likely due to reaching the resolution limit of the μCT experimental conditions. These

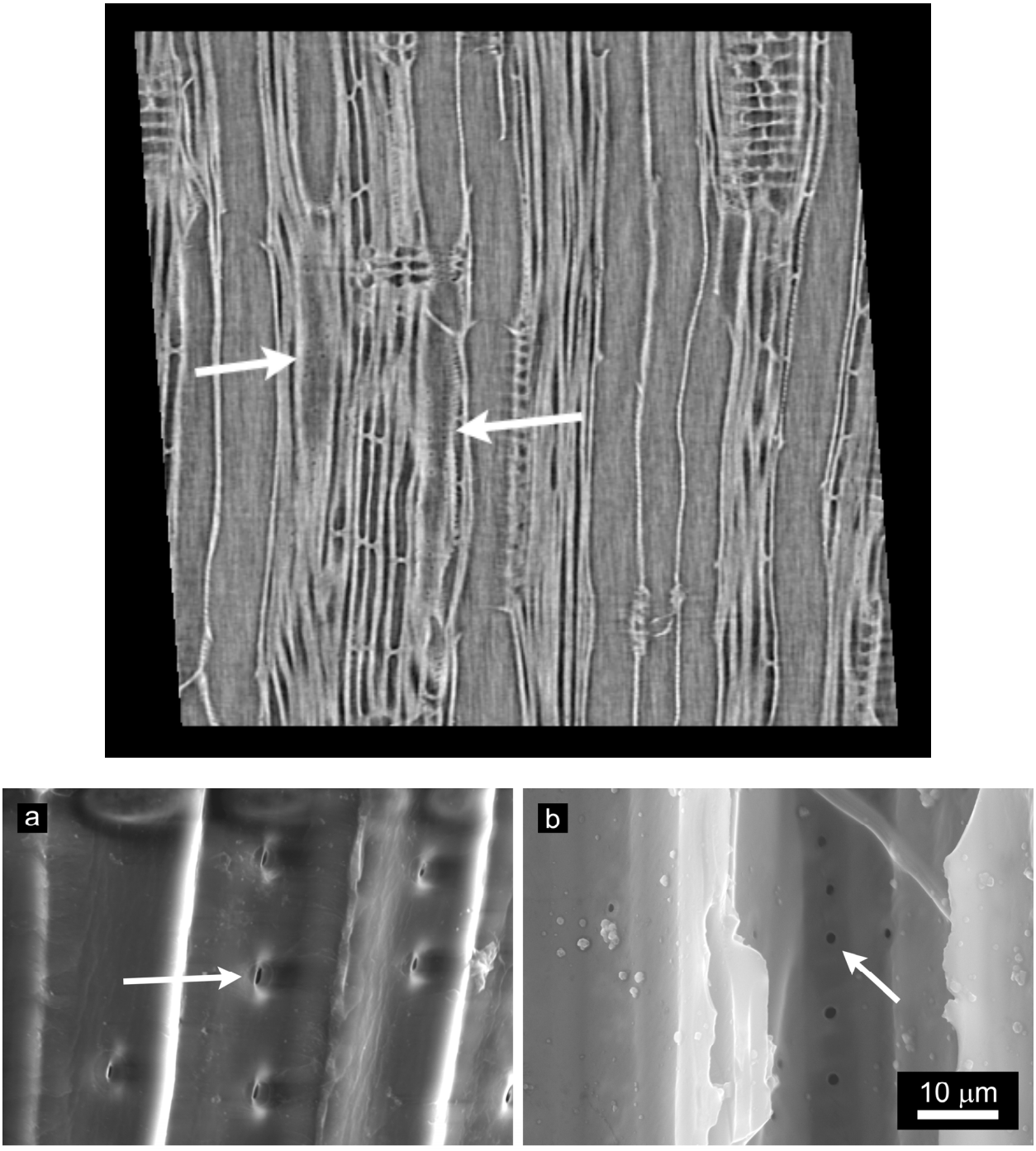

Figure 3.17. Tangential µCT slice of the BE-wood (top), and (a) an environmental SEM micrograph image of the BE-wood, and (b) a SEM micrograph of the BE-C. The width of the µCT slice is approximately 750 µm. The arrows indicate the observed interconnections between pores.

small features in the wood and carbon were lost upon conversion of the C to SiC due to the dissolution of the carbon and precipitation of relatively large SiC grains.

The μCT data also revealed the imperfect nature of the pores in the wood, C and SiC. The vessels were generally aligned in the axial direction but often deviated from linearity, and the diameter of the vessels undulated through the sample thickness. While the wood pore walls were smooth, some roughness was observed in the C and SiC samples. This appears almost randomly as there are instances where one pore is smooth and the adjacent pore is rough. The roughness in the C sample could be the result of escaping volatile gasses or volumetric shrinkage during the pyrolysis process. This pore wall damage would then be retained in the SiC microstructure during the silicon melt-infiltration. Decreasing the pyrolysis heating rates, or adding additional hold times at intermediate temperatures could reduce the amount of damage accumulated during pyrolysis.

3.6. Summary

Beech and sapele wood were converted into porous SiC by pyrolyzing the wood, infiltrating the carbon with molten silicon, and finally etching away the excess silicon. The density and porosity of the SiC were measured using Archimedes' method, and the pore size distribution was measured with mercury intrusion porosimetry. The Archimedes measurements and microscopy revealed the presence of closed porosity and residual carbon in the SiC preforms. The pore size distributions of the BE- and SA-SiC were monomodal and bimodal, respectively. Pores measuring less than about one micrometer in diameter were not observed in the SiC, as they were in the carbon material, due to the

volume expansion that occurred during the reaction between carbon and molten silicon to form the SiC.

Infiltration experiments with the A356 alloy were largely unsuccessful: both pressureless and gas-pressurized infiltration experiments resulted in, at best, partial Al-infiltration of the SiC preforms. Pressurized infiltration of the Al-Si-Mg alloy was successful, and it was found that the alloy had to be prepared in an inert environment to prevent the magnesium from reacting with the aluminum and oxygen. The metal in the resulting composites contained both Si and Mg_2Si precipitates due to the large amounts of Si and Mg in the Al-alloy.

X-ray microtomography was performed on the BE-wood, C, SiC, and MCC. The data were used to compare microstructural features present in each of the processing stages. While the general structure of the beech was retained throughout processing, some wood features, such as the connections between pore channels and smooth nature of the pore walls, were lost upon conversion to SiC.

4. Aluminum/Silicon Carbide Composites: Mechanical Properties

4.1. Introduction

This chapter describes the experimental methods used to characterize the mechanical properties of the Al/SiC composites introduced in the previous chapter. The composite properties are compared to those of the Al-Si-Mg alloy and, where data are available, to the porous wood-derived SiC. Predictions for the elastic modulus and of the longitudinal toughness are obtained from constituent properties and the appropriate models: Halpin-Tsai bounds (Halpin *et al.* 1976) for the elastic properties and the Ashby model of the effect of ductile particle-reinforcement on the toughness of brittle materials (Ashby *et al.* 1989). Comparisons of the model predictions with the experimental results provide information on the main microstructural factors which control the mechanical behavior of the composites.

4.2. Experimental Methods

4.2.1. Compressive Strength

Compression testing was carried out on BE-MCC samples measuring 4 x 4 x 8 mm^3, which were made four per infiltration batch using the graphite sample holder shown in Figure 4.1. The composites measured 5 x 5 x 10 mm^3, but the outer edges consisted of an aluminum skin, which was machined away. In order to decrease the sample processing time, the graphite sample holder was altered to accommodate a SiC preform measuring 25 x 25 x 10 mm^3. Machining compression samples from the larger block decreased the overall machining per sample and increased the sample yield per infiltration run.

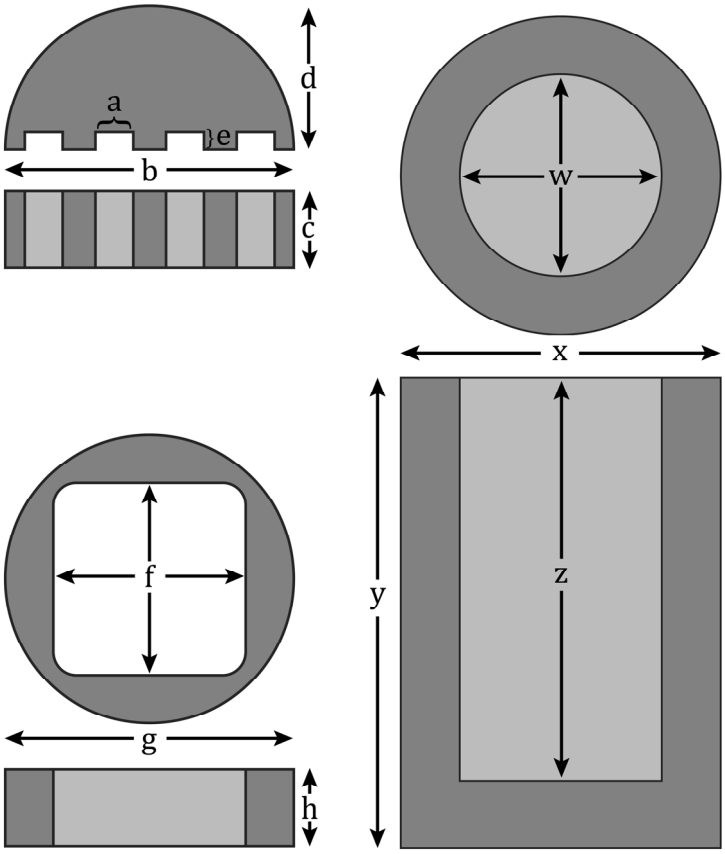

		Compression Tests (5 x 5 x 10 mm³ preform)	Compression Tests (25 x 25 x 10 mm³ preform)	Flexure Tests (35 x 35 x 35 mm³ preform)
Dimensions	a	5	-	-
	b	38	-	-
	c	15	-	-
	d	19	-	-
	e	3	-	-
	f	-	25	35
	g	-	38	51
	h	-	15	40
	w	38	38	51
	x	70	70	76
	y	89	76	89
	z	73	60	73

Figure 4.1. Schematic drawings of the graphite sample holders and crucibles used for pressurized infiltrations. The dimensions, listed in the table, are in millimeters.

The compression strength was calculated as the maximum recorded load divided by the specimen cross-sectional area. In order to study the anisotropy of the composites, specimens were machined with the 8.0 mm dimension both parallel and perpendicular to the axial, or longitudinal (LO), direction. A Sintech 20/G (MTS Systems Corp., Eden Prairie, MN) universal testing machine was used to load the specimens along the 8.0 mm direction at a rate of 100 μm/minute.

4.2.2. Ultrasonic Pulse Echo

The velocity of sound waves propagating through a material can be related to the material's elastic constants (McGonnagle 1968). Pulse echo refers to a technique where an ultrasonic wave is transmitted through a material, echoes off the opposite face and returns to the starting point. The total time-of-flight (TOF) is recorded from an oscilloscope and interpreted to characterize the material in question. The ultrasonic pulses are typically transmitted and received by piezoelectric transducers; for pulse echo, one transducer is used for both duties. A couplant is used between the transducer and material surface to eliminate air, which impedes the signal transmission. Attenuation of an ultrasonic wave within the specimen increases the TOF and is caused by factors such heat generation due to vibrating particles and scattering at material interfaces.

Two types of waves are used in pulse echo measurements: longitudinal and transverse. As the ultrasonic wave travels through the specimen, particles are displaced. Longitudinal waves propagate in the same direction as the displaced particles, as shown in Figure 4.2. Transverse, or shear, waves propagate perpendicular to the direction of the displaced

particles. If either the thickness or elastic stiffness of a material is known, the TOF can be used to calculate the other property.

The number of independent TOF measurements needed depends on the material symmetry and is equal to the number of independent components of the 6 x 6 elastic compliance (S_{ij}) or stiffness (C_{ij}) matrices, i.e. the maximum is 21 (Ledbetter *et al.* 1977). Only two measurements, one longitudinal and one transverse, are needed for isotropic materials. To calculate the elastic stiffness, the TOF measurements are used to calculate the velocity of sound in the specimen which is related to the modulus, E, Poisson's ratio, ν, and density, ρ, of the material:

$$V_L = \left(\frac{E(1-\nu)}{\rho(1+\nu)(1-2\nu)} \right)^{1/2} \tag{4.1a}$$

$$V_T = \left(\frac{E}{2\rho(1+\nu)} \right)^{1/2} \tag{4.1b}$$

where V_L and V_T are the velocity in the longitudinal and transverse directions, respectively. After measuring the density of the sample, Equation 4.1 can be solved for E and ν.

Composite materials can present a more difficult situation due to anisotropy and the signal attenuation caused by the acoustic impedance mismatch of the matrix and reinforcement materials. For orthorhombic materials (9 independent C_{ij} components), longitudinal wave measurements are used to calculate C_{11}, C_{22}, and C_{33} according to:

$$C_{ii} = \rho v_{ii}^2, \tag{4.2}$$

where ρ is the specimen density and the velocity, v, is twice the specimen thickness divided by the TOF (Musgrave 1970). The first and second velocity subscripts denote the sound

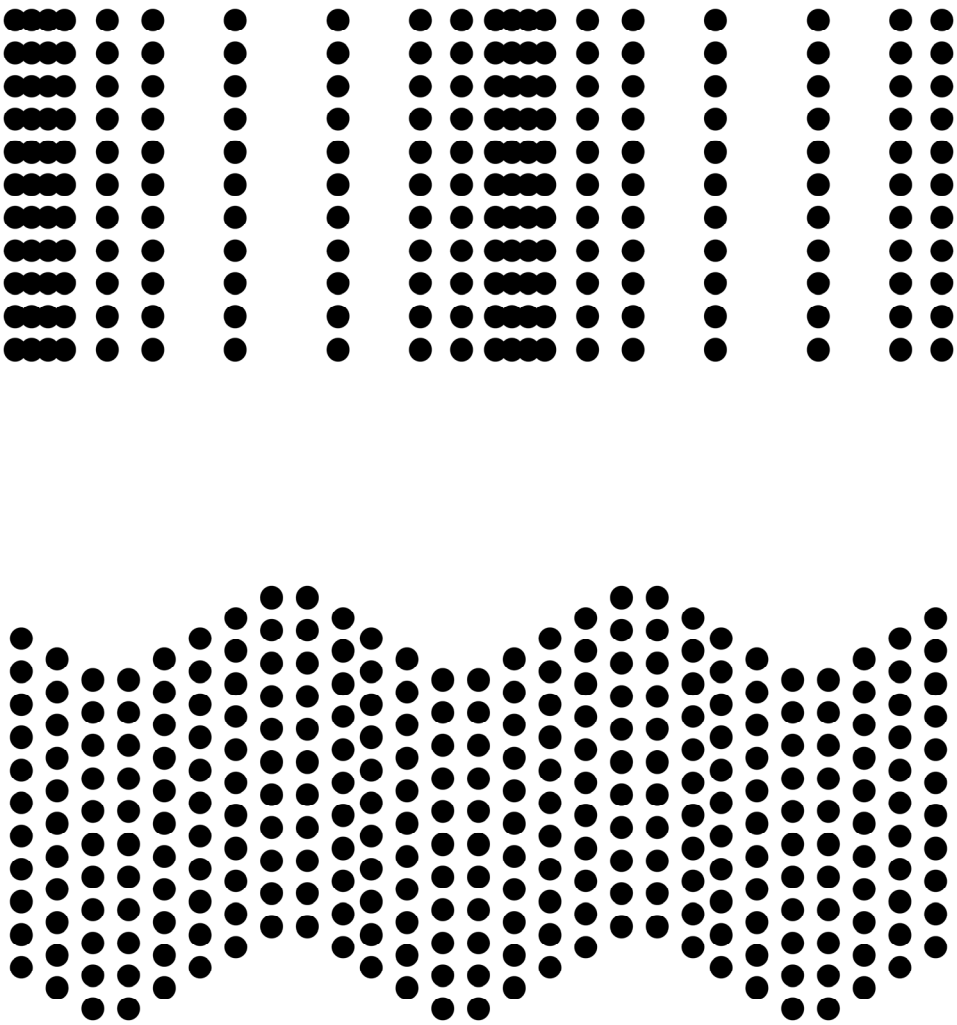

Figure 4.2. Schematic of particle displacement resulting from the propagation of either a (top) longitudinal or (bottom) transverse wave.

wave propagation and particle displacement directions, respectively. Shear wave measurements are used to calculate C_{44}, C_{55}, and C_{66} where:

$$C_{44} = \rho v_{23}^2,\ C_{55} = \rho v_{13}^2, \text{ and } C_{66} = \rho v_{12}^2. \quad (4.3)$$

Calculating the off-diagonal constants, C_{12}, C_{13}, and C_{23}, requires specimens oriented in non-principle directions (Ledbetter *et al.* 1977). Once complete, the stiffness matrix is inverted to calculate the elastic compliance matrix, S_{ij}, which is used to calculate values for the Young's moduli E_{11}, E_{22}, and E_{33}.

For the current work, ultrasonic measurements were made with 5 MHz transducers and an ultrasonic inspection system (Matec Instrument Companies, Northborough, MA) on BE-MCC samples measuring 4.0 x 4.0 x 8.0 mm^3. The sound velocity was measured by recording the TOF of sound waves through the specimens. Orthorhombic symmetry was assumed and nine measurements were made: one longitudinal and two shear measurements for each principal direction. Error in the diagonal elastic stiffnesses was calculated as the standard deviation of 10 separate TOF measurements. The sample-couplant-transducer bond was completely broken between measurements. Two coupling materials were used: glycerin for longitudinal wave measurements and molasses for shear wave measurements.

The TOF measurements were used to calculate the elastic stiffness matrix, C_{ij}. Longitudinal wave measurements were used to calculate C_{11}, C_{22}, and C_{33} according to Equation 4.2, and shear wave measurements were used to calculate C_{44}, C_{55}, and C_{66} according to Equation 4.3. In order to calculate the elastic compliance matrix, S_{ij}, the three

off-diagonal elastic stiffnesses were estimated by assuming transverse isotropy and using the relationship

$$C_{12} = C_{11} - 2C_{66} \tag{4.4}$$

Standard propagation of error was used to calculate the error in C_{12}, C_{13}, and C_{23}, which were assumed to be equal. The C_{ij} matrix was inverted to obtain the elastic compliance matrix, S_{ij}, which was used to calculate the values for the Young's moduli: E_{11}, E_{22}, and E_{33} which correspond to E_{Radial}, $E_{Tangential}$, and E_{Axial}, respectively.

4.2.3. Flexural Tests

As bigger samples were needed for bend tests, the graphite components for the gas-pressure infiltration process were modified (Figure 4.1) to accommodate a 35 x 35 x 35 mm^3 preform. The amount of time needed to convert a carbon preform of that size into SiC and the subsequent etching time were decreased by using seven preforms each measuring 35 x 35 x 5.0 mm^3. After infiltration, the BE- or SA-MCCs were machined into bars measuring 3.0 x 3.0 x 35 mm^3, which allowed for a span length of 30 mm.

The flexural strength and modulus were measured with 30 mm spans while single-edge notched bars with dimensions 3.0 x 3.0 x 15 mm^3 were used to measure the fracture toughness (span length of 12 mm). The notches were introduced using a slow-speed diamond saw and measured 0.5 mm deep and 0.2 mm wide. The notch tips had a square cross-section with rounded corners. All bend tests were carried out in a three-point bend configuration as shown schematically in Figure 4.3, which also depicts the three specimen

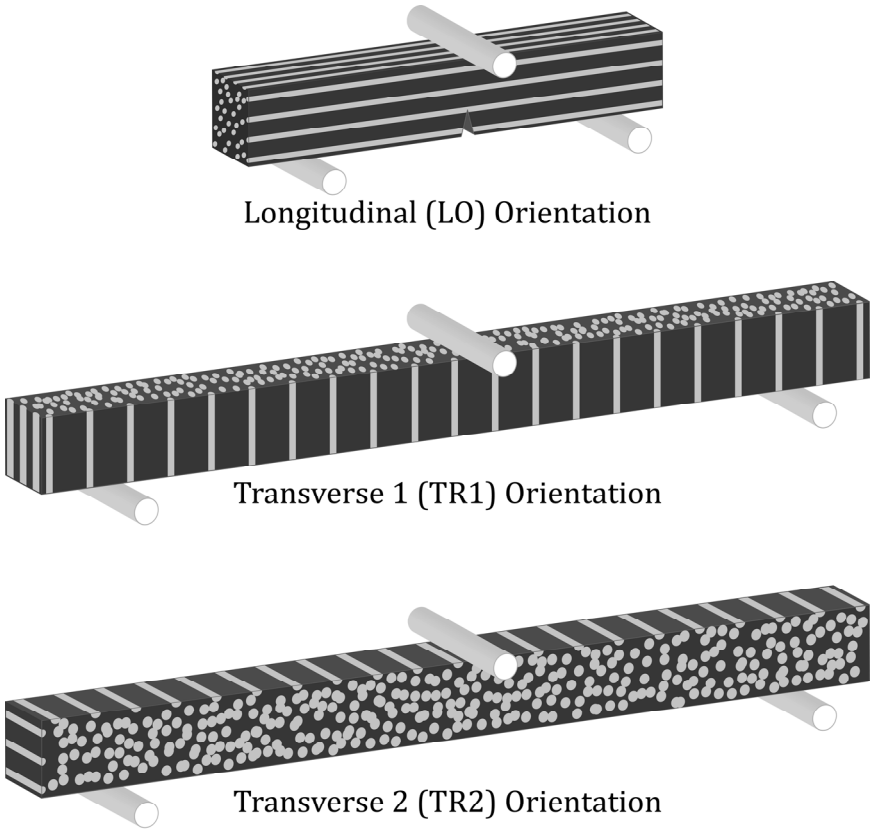

Figure 4.3. Bend test sample orientations: (top) a notched longitudinal (LO) specimen for fracture toughness measurements and transverse 1 (TR1) and 2 (TR2) specimens without notches, middle and bottom respectively, for flexural modulus or strength measurements.

orientations. The Al-filled pores in LO samples are oriented normal to fracture surfaces. Transverse samples are oriented with the Al-filled pores lying in the fracture plane and either parallel (TR1) or perpendicular (TR2) to the applied load. Bars of the Al-Si-Mg alloy were also machined and tested using the same dimensions and specifications as the MCC specimens. For the purposes of modeling the fracture behavior, the tensile properties of the Al-Si-Mg alloy were also measured. In particular, the yield stress and Young's modulus were determined with cylindrical samples according to ASTM standard E8 (ASTM 2004). The specimen gage diameter and gage length were 6.4 mm and 28.6 mm, respectively.

Flexural strength and fracture toughness tests were conducted with an Instron 8501 (Norwood, MA) mechanical testing machine, and a frame-mounted MTS 653 furnace (Eden Prairie, MN) was used to heat specimens for tests above room-temperature. A linear variable differential transducer was used to measure the displacement. Tests were conducted using a displacement rate of 100 μm/minute, a heating rate of 10°C/minute and a hold time of 20 minutes. The flexural strength was calculated according to ASTM C1161 (ASTM 2003), and the fracture toughness was calculated according to sample parameters in (Guinea *et al.* 1998) and ASTM C1421 (ASTM 2002) using between three and six samples for each testing condition. Specimen microstructures, fracture surfaces, and crack paths were examined by scanning electron microscopy.

Tests to measure the evolution of the flexural modulus with temperature were carried out in an Instron 4505 mechanical testing machine with a custom-built furnace (Entech, Ängelholm, Sweden). The mid-span deflection of the bend bar was measured through a quartz window in the furnace using a high-resolution laser extensometer (Zygo 2211,

Middlefield, CT). The displacement rate, heating rate, and hold time were 100 μm/minute, 10°C/minute, and 20 minutes, respectively. The flexural modulus was calculated from the slope of force versus mid-span displacement curves according to ASTM C1161 (ASTM 2003). For each material and orientation, one specimen was used to measure elastic loading-unloading curves for the entire range of testing temperatures. After each measurement, the specimen was heated to the next set-point and held for 20 minutes before repeating the loading-unloading measurement.

Tensile testing of the aluminum alloy was conducted in an MTS 808 (Eden Prairie, MN) mechanical testing machine, using a frame-mounted ATS 3210 (Butler, PA) furnace, and an extensometer (MTS 632-13B-21, Eden Prairie, MN). Tests were carried out under displacement control with a displacement rate of 1.0 mm/minute. Samples tested above room-temperature were heated under load-control without a programmed heating rate. Before testing, the temperature was held until the extensometer reading stabilized, i.e. when both the specimen and fixture had reached thermal equilibrium. The Young's modulus of the aluminum alloy was measured as the slope of the tensile stress versus strain curve, and the yield strength was calculated using the offset method at 0.2% strain.

4.2.4. Strain Measurements via High-Energy X-ray Diffraction

The mechanical behavior of a metal/ceramic composite is governed by load transfer from the compliant metal to the stiff ceramic phase (Clyne *et al.* 1993). Under an applied stress, both phases in a composite initially act in an elastic manner, each carrying a load proportional to the phase volume fraction. As the stress increases, the metal yields and

load is transferred to the ceramic phase. As the load borne by the ceramic increases, debonding between phases or fracture of the ceramic may occur; this decreases the efficiency of load transfer and leads to macroscopic failure (Wanner *et al.* 2000).

Both neutron diffraction and X-ray diffraction have been used to measure the lattice strains of composites during loading (Balch *et al.* 2006; Young *et al.* 2007a; Young *et al.* 2007b). The advantages of using high-energy X-rays over neutron diffraction are the faster exposure times and smaller diffraction volumes needed to measure the bulk strain. In the X-ray diffraction experiments, shown schematically in Figure 4.4, incrementally increasing load is applied to the sample in either tension or compression. The X-ray beam is diffracted through a small volume of the sample and Debye rings are collected on a detector. A sample pattern is shown in Figure 4.5. The radius of each ring in the pattern corresponds to a specific crystallographic plane of one of the materials present in the sample.

An unstressed and untextured polycrystalline material will have perfectly circular Debye rings, but the rings are distorted into ellipses in a stressed state. Ring distortions, are related to deviations from the equilibrium d-spacing according to

$$\varepsilon_\eta = \frac{d_\eta - d_0}{d_0} = \frac{r_\eta - r_0}{r_0} \tag{4.5}$$

where ε_η is the strain at azimuth angle η, and d and r are the d-spacing and radius of the ring, respectively, in the unstressed (subscript 0) or stressed (subscript η) state at angle η (Noyan *et al.* 1987). An azimuth angle of η=0° corresponds to the loading direction while an angle η=90° corresponds to the direction orthogonal to the loading and beam propagation directions.

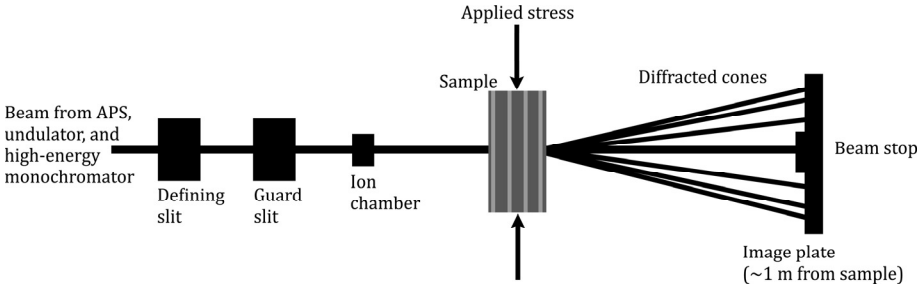

Figure 4.4. Schematic of the experimental set-up used to measure strain with high-energy X-ray diffraction (after Young 2006).

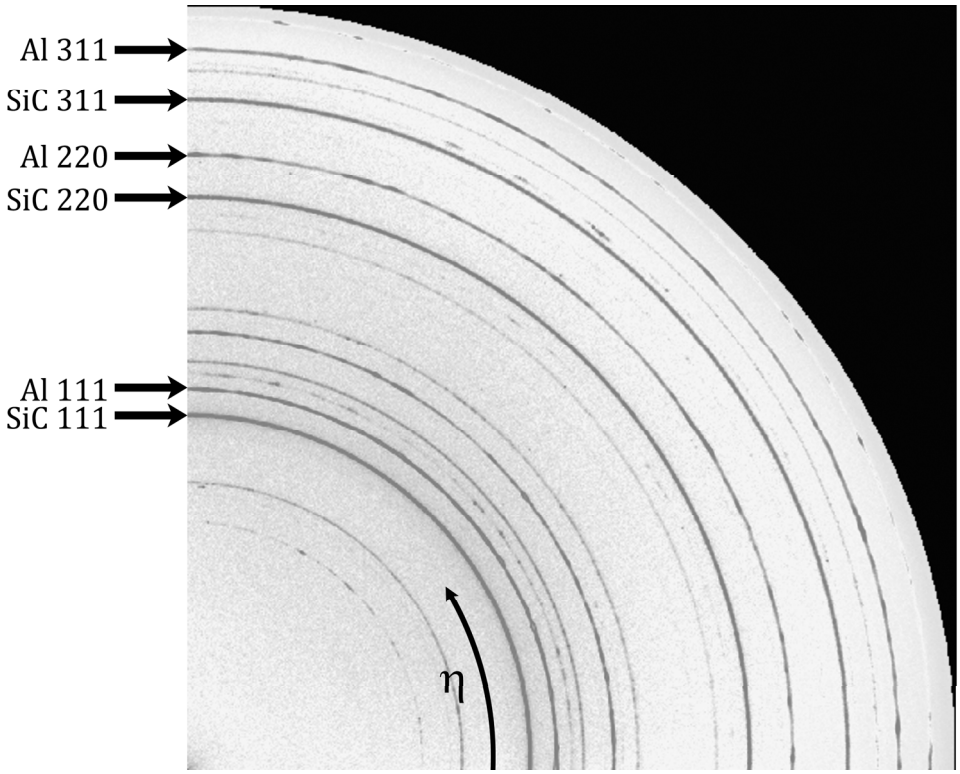

Figure 4.5. Representative X-ray diffraction pattern (one quarter of the total plate) depicting the rings for the BE-MCC sample studied in this work.

To study the load partitioning of the Al/SiC MCCs, the volume-averaged lattice strains of the aluminum and SiC were measured by synchrotron X-ray diffraction (1-ID XOR-CAT, Advanced Photon Source, Argonne National Laboratory) as a function of applied stress in uniaxial compression. A screw-driven system was used to apply load to a BE-MCC sample measuring 4.0 x 4.0 x 8.0 mm^3 with the loading direction corresponding to the axial direction. The applied stress was increased in steps of ≈ 25 MPa and was constant during the diffraction measurements, which took ≈ 30 seconds per measurement. As depicted in Figure 4.6, two data sets were collected at each applied stress in order to account for any deviation from transverse isotropy within the sample. Data were collected with the beam propagation direction corresponding to both the radial (RA) and tangential (TA) directions.

A high-energy (87 keV) monochromatic X-ray beam with a 100 x 100 μm^2 cross-section was transmitted through the 4.0 mm sample thickness, which resulted in a diffraction volume of 0.04 mm^3. A Mar345 imaging plate, approximately 1200 mm from the sample, was used to collect the diffraction data, a sample of which is shown in Figure 4.5. Strain in the Al and SiC was calculated at $\eta = 0°$ and 90°, according to Equation 4.5 (He *et al.* 1998). The strain-free d-spacing and radius were calculated using single crystal elastic constants (Hellwege 1979; Noyan *et al.* 1987; Hauk *et al.* 1997) and the relationship between the Poisson's ratio, ν, of a crystallographic plane and the strain-free azimuth angle, η^*,

$$\nu = \frac{\sin^2\eta^*}{1-\sin^2\eta^*} \tag{4.6}$$

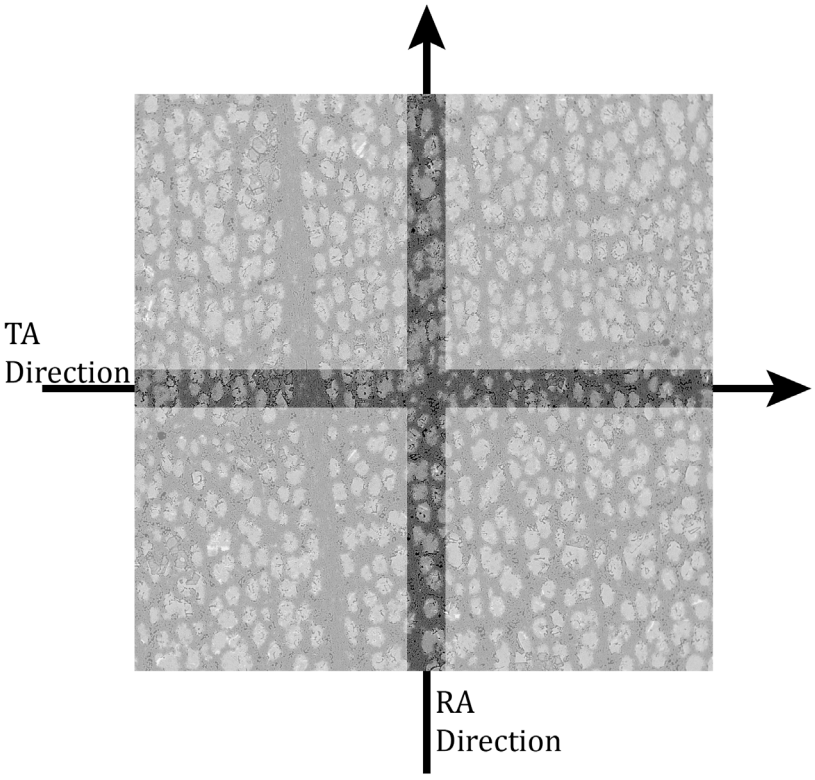

Figure 4.6. Representation of the two perpendicular X-ray beam propagation directions used during high-energy X-ray diffraction. The dark areas represent the 100 μm width of the beam.

4.3. Results

4.3.1. Compressive Strength & Ultrasonic Pulse Echo

In compression, the MCC samples exhibited linear elastic behavior until failure. Stress versus strain curves showed deviations corresponding to about 0.1% plastic strain before reaching ultimate load, upon which the samples exhibited brittle failure. The corresponding strength of both axially- and radially- loaded samples are summarized in Table 4.1 along with the strengths of the porous BE-SiC material (Kaul *et al.* 2006).

Table 4.1. Apparent specific gravity and porosity, volume fraction of SiC, and compressive strength of the BE-MCCs and porous BE-SiC.

	Loading Direction	Apparent Specific Gravity (g/cm^3)	Apparent Porosity (%)	SiC Fraction (vol. %)	Compressive Strength (MPa)
BE-SiC[a]	Axial	3.04 ± 0.05	53.2 ± 1.3	100	401 ± 95
BE-MCC	Axial	2.72 ± 0.03	11.6 ± 3.5	53	563 ± 79
BE-SiC[a]	Radial	3.04 ± 0.05	53.2 ± 1.3	100	25 ± 3
BE-MCC	Radial	2.76 ± 0.05	3.0 ± 1.5	48	405 ± 53

a) BE-SiC data from (Kaul *et al.* 2006).

The BE-SiC strength is highly anisotropic, being larger by a factor of 16 in the axial direction as compared to the radial direction. The presence of the aluminum alloy in the channels resulted in a higher axial compressive strength and a significantly higher radial strength (by a factor 16), but at the expense of a 70% higher average density. Also of note are the large standard deviations, which were most likely due to the heterogeneous nature of the wood starting material.

An example of the output (amplitude versus time) from the pulse echo software is shown in Figure 4.7. The measured elastic stiffnesses, compliances, and moduli of the BE-MCCs are shown in Table 4.2 along with values calculated with the Halpin-Tsai equations (Equations 2.16 and 2.17). The matrix modulus, E_m, was taken as the pulse echo-measured modulus of the aluminum alloy, 78 GPa. The modulus of the SiC, E_f, was assumed to be 408 GPa, which has been previously measured by nanoindentation of the wood-derived SiC (Kaul *et al.* 2008). The SiC volume fraction, V_f, was taken as 0.50, and the ξ values used were those reported for uniaxial composites: infinity for the axial orientation and 0.50 for the radial and tangential orientations (Chawla 1998).

Table 4.2. Elastic stiffnesses measured via ultrasonic pulse echo and the corresponding elastic moduli. Also shown are the Halpin-Tsai predictions.

ij	C_{ij} (GPa)	E_{ii} (GPa)	Halpin-Tsai (GPa)
11	155 ± 3	119	146
22	124 ± 3	91	146
33	197 ± 3	158	243
44	56 ± 4		
55	55 ± 2		
66	47 ± 4		
12	62 ± 5		
13	62 ± 5		
23	62 ± 5		

Figure 4.7. Digital readout from the ultrasonic inspection system of wave amplitude versus time.

4.3.2. Flexural Modulus

The flexural modulus of the MCCs and Al alloy are shown as a function of temperature for each orientation in Figure 4.8. The dashed lines represent Halpin-Tsai predictions (Chawla 1998), which were calculated according to Equations 2.16 and 2.17. The matrix modulus, E_m, was taken as the experimentally-measured flexural modulus of the bulk metal. The modulus of the SiC, E_f, was assumed to be constant in the temperature range of this study, and was taken to be 408 GPa (Kaul *et al.* 2008). For simplicity, the SiC volume fraction, V_f, was taken as 0.50 for both the BE- and SA-MCCs, and ξ was taken to be infinity for the LO orientation and 0.50 for the TR1 and TR2 orientations (Chawla 1998). The modulus of the bulk aluminum alloy remained relatively constant at about 70 GPa from 25°C to 300°C, decreased between 300°C and 400°C to 30 GPa, and was too compliant to reliably test at 500°C. The elastic moduli of the LO-MCCs remained relatively constant at about 200 GPa up to 300°C and decreased linearly above this temperature to about 130 GPa at 500°C. The Halpin-Tsai predictions overestimated the stiffness of the BE- and SA-MCCs in the LO orientation. The moduli in the transverse orientations were lower than those of the LO specimens and decreased linearly from a maximum stiffness of about 130 GPa at 25°C to a minimum of about 85 GPa at 500°C. Agreement between the Halpin-Tsai calculations and the transverse data was, in general, better than that in the LO orientation. The LO data at 25°C were equal, within error, to data from literature for the flexural modulus of the same Al-Si-Mg alloy reinforced with SiC particles (Pech-Canul *et al.* 2000b). The SiC_p-reinforced Al-Si-Mg, which had 41-54 vol.% SiC and 3-8 vol.% porosity, was stiffer than the wood-derived composites tested in the transverse orientation.

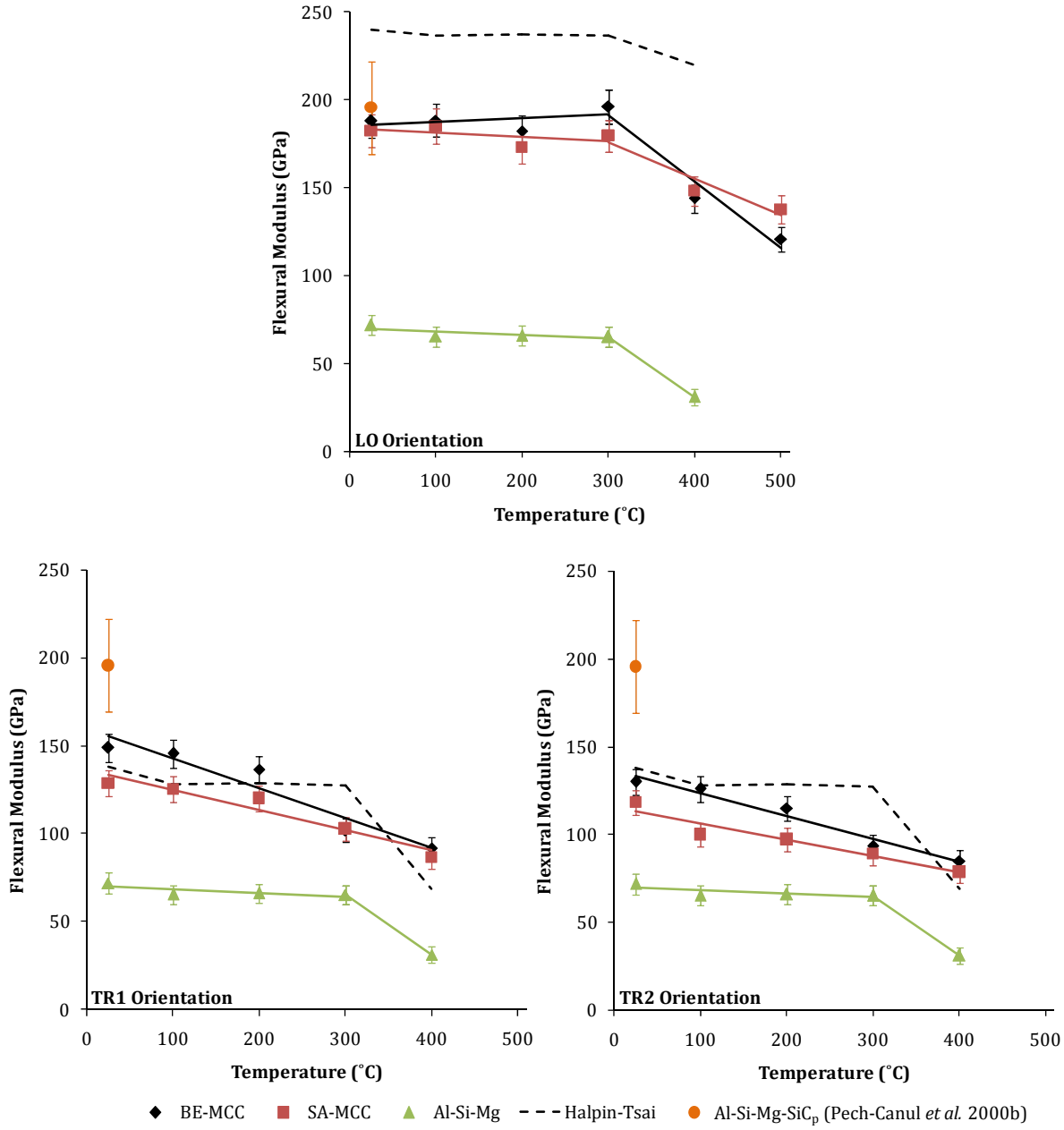

Figure 4.8. Flexural modulus versus temperature for the LO, TR1 and TR2 orientations of the BE- and SA-MCCs and the bulk Al-Si-Mg alloy (Wilkes *et al.* 2008). The dashed lines represent Halpin-Tsai predictions for the modulus of a uniaxial composite (Chawla 1998). The error bars represent one standard deviation. Also shown are room-temperature data from Pech-Canul *et al.* (2000b) for SiC_p-reinforced Al-Si-Mg composites.

4.3.3. Flexural Strength

Representative load-displacement curves are shown in Figure 4.9. The composites presented linear-elastic behavior until fracture in the longitudinal direction regardless of test temperature and despite evidence of extensive plastic deformation of the metal at high-temperatures. The room-temperature load-displacement curves in the transverse directions were also linear-elastic until fracture in all cases, but the BE-MCCs tested in the TR2 orientation showed serrations in the curves. The serrations are indicative of intermittent crack propagation due to differences in the microstructure along the crack path. The specimens tested in the transverse orientations at high-temperatures showed non-linear load-displacement curves and the degree of non-linearity increased with temperature.

The average value of the flexural strength of the MCCs and of the Al alloy are shown as a function of temperature for each orientation in Figure 4.10. The difference between the strength of the bulk Al-Si-Mg at 25°C and 200°C was statistically insignificant, but the alloy was drastically weaker at higher temperatures; the composites exhibited a similar trend. As was the case with the elastic modulus, the strength of the MCCs was anisotropic, and the specimens tested in the longitudinal direction were consistently stronger than those tested in the TR1 and TR2 orientations over the entire temperature range. Also plotted in Figure 4.10 are data from literature for the room-temperature flexural strength of the same Al-Si-Mg alloy reinforced with SiC_p (Pech-Canul *et al.* 2000b). The strength of the SiC_p-reinforced Al-alloy was equal, within the experimental error, to the BE-LO composites, slightly weaker than the SA-LO composites and stronger than the TR1 and TR2 composites.

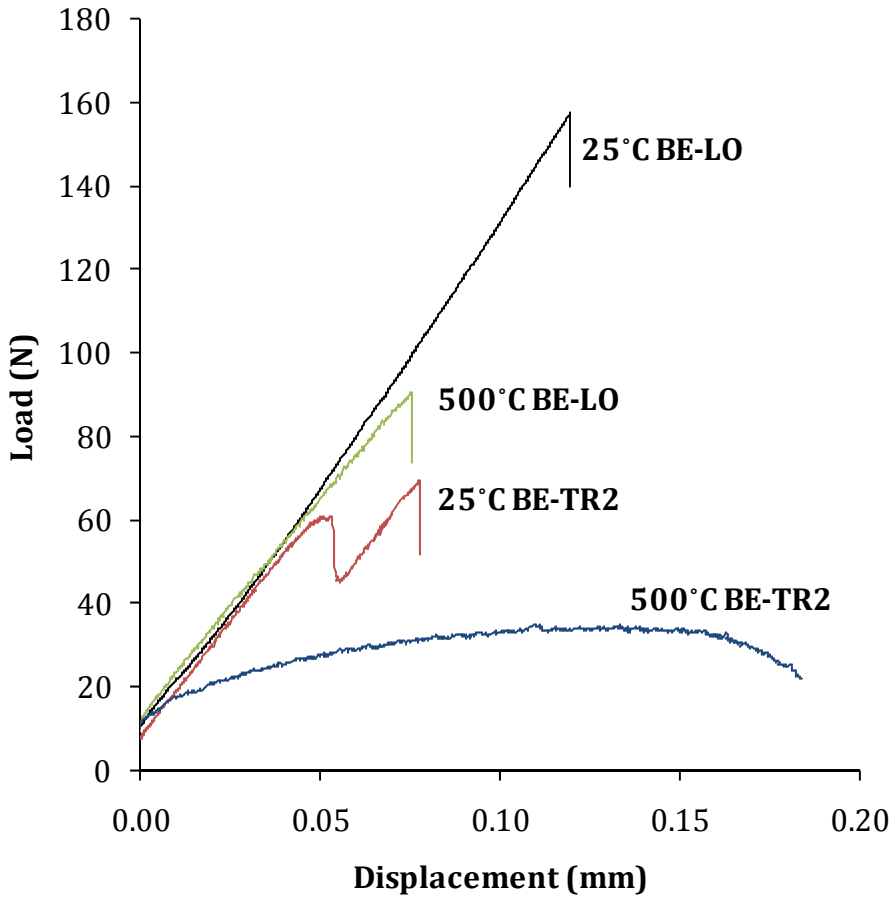

Figure 4.9. Load-displacement curves of BE-MCCs tested in the LO and TR2 orientation at 25°C and 500°C (Wilkes *et al.* 2008).

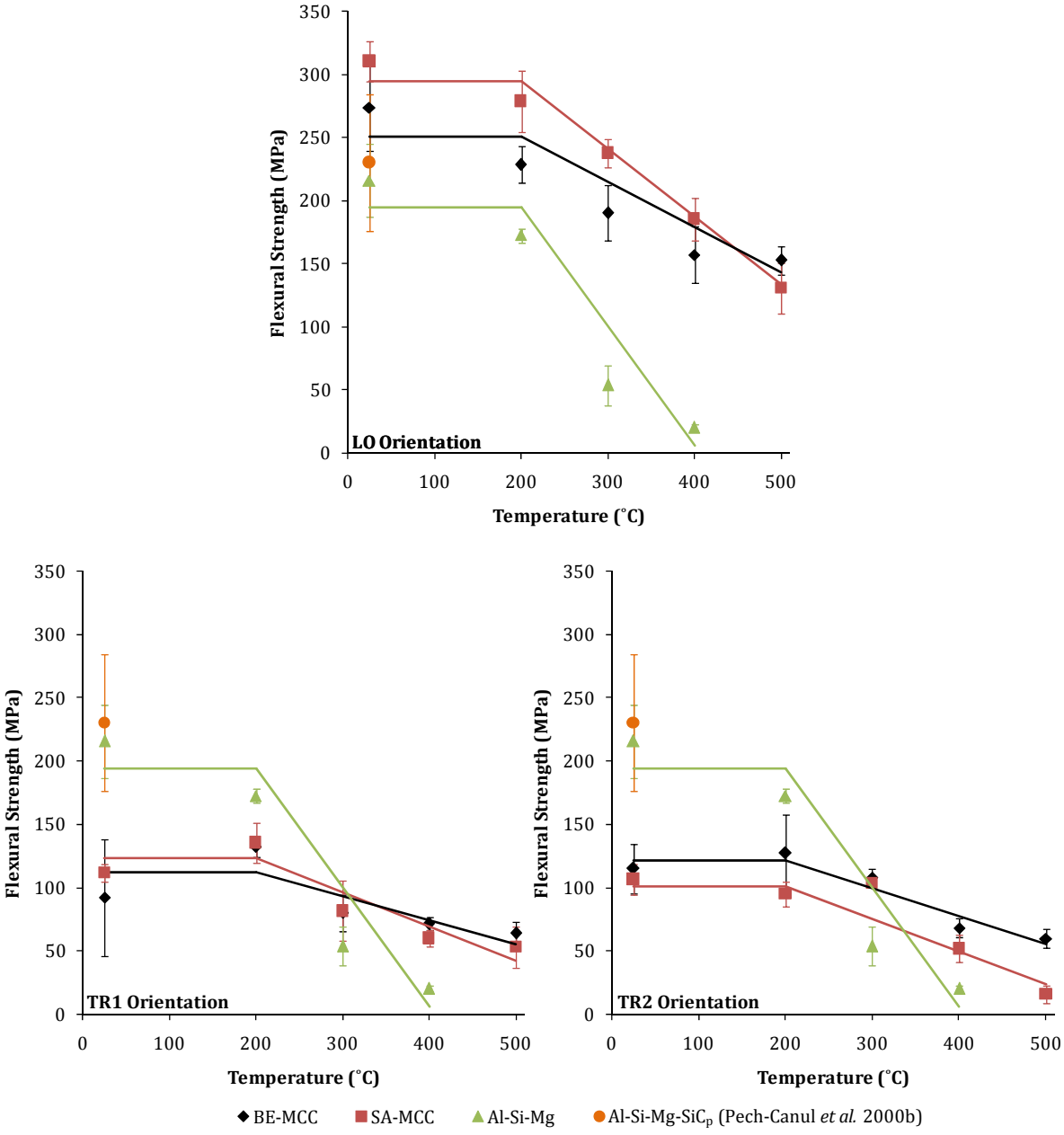

Figure 4.10. Flexural strength versus temperature for the LO, TR1 and TR2 orientations of the BE- and SA-MCCs and the bulk Al-Si-Mg alloy (Wilkes *et al.* 2008). The error bars represent one standard deviation. Also shown are room-temperature data from Pech-Canul *et al.* (2000b) for SiC_p-reinforced Al-Si-Mg composites.

4.3.4. Fracture Toughness

The average values of the toughness of the Al alloy and of the MCCs in the longitudinal and transverse orientations are plotted in Figure 4.11 as a function of temperature. The toughness of the bulk alloy, as compared with some Al alloys (Hahn *et al.* 1975), was low due to the large volume fraction and size of the primary Si crystals and Mg_2Si precipitates. Moreover, the toughness decreased rapidly above 200°C, following a trend similar to that found for the flexural strength. The LO toughness was greater than the TR1 or TR2 toughness, particularly at ambient temperature, and decreased linearly with temperature. The toughness in the TR1 and TR2 orientations was relatively constant from 25°C to 200°C and decreased linearly above this temperature.

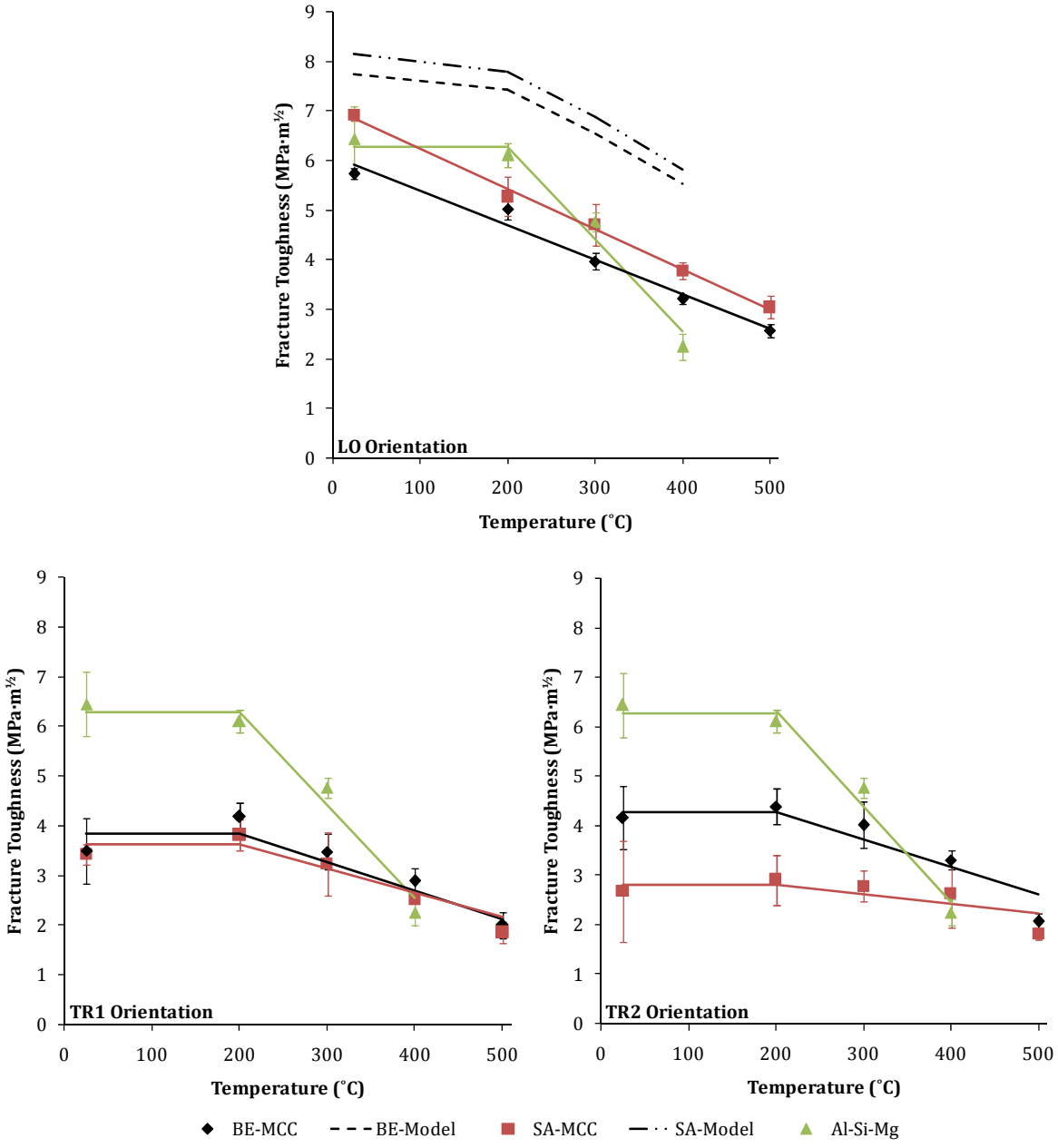

Figure 4.11. Fracture toughness versus temperature for the LO, TR1 and TR2 orientations of the BE- and SA-MCCs and the bulk Al-Si-Mg alloy (Wilkes *et al.* 2008). The error bars represent one standard deviation. Also plotted, for the LO orientation, are fracture toughness models calculated following Ashby *et al.* (1989).

4.3.5. Load Partitioning

Figure 4.12 depicts the applied stress versus lattice strain, in both the longitudinal (parallel to load) and transverse (perpendicular to load) directions, calculated from diffraction measurements for the Al (111) and SiC (111) reflections. The data for both sample rotations (Figure 4.6) are shown: filled symbols indicate data collected with the beam transmitted through the sample in the radial direction (RA), and unfilled symbols indicate data collected in the tangential direction (TA). At zero applied load, the residual longitudinal strains were small and compressive for the SiC (-69 and -129 με) and tensile for the Al (136 and 60 με). The residual transverse strains were near zero (8 and 9 με) for the SiC and compressive for the Al (-41 and -224 με).

In regard to the longitudinal lattice strain, the slopes of the Al curves increased at stresses above the ninth load point (-213 MPa), which indicated the onset of plastic deformation. The two curves for the Al were approximately equal throughout loading, but the measured bulk longitudinal lattice strain of the SiC, at a given applied stress, was more compressive in the TA orientation than in the RA orientation. Figure 4.13 plots the applied stress versus lattice strain for both the SiC and Al (111), (220) and (311) reflections with the sample in the TA orientation (similar behavior was observed in the RA orientation). In the elastic region, the slopes of both the SiC and Al curves were equal within the experimental error. In the plastic region, the three Al curves were relatively equal within the experimental error, but the (111) curve became vertical at applied stresses above ≈ 300 MPa.

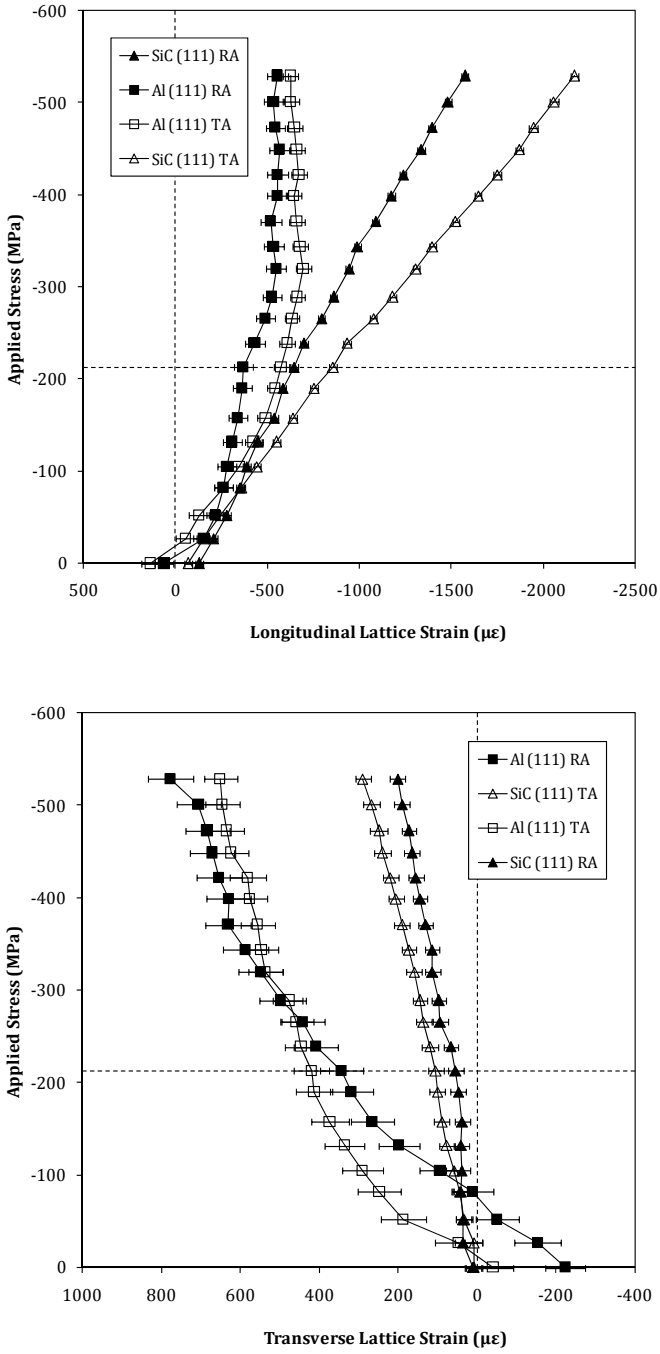

Figure 4.12. Applied compressive stress versus (top) longitudinal and (bottom) transverse lattice strain for the Al (111) and SiC (111) reflections with the beam parallel to both the RA and TA direction. The horizontal dashed line (-213 MPa) indicates approximately the transition from elastic to plastic deformation.

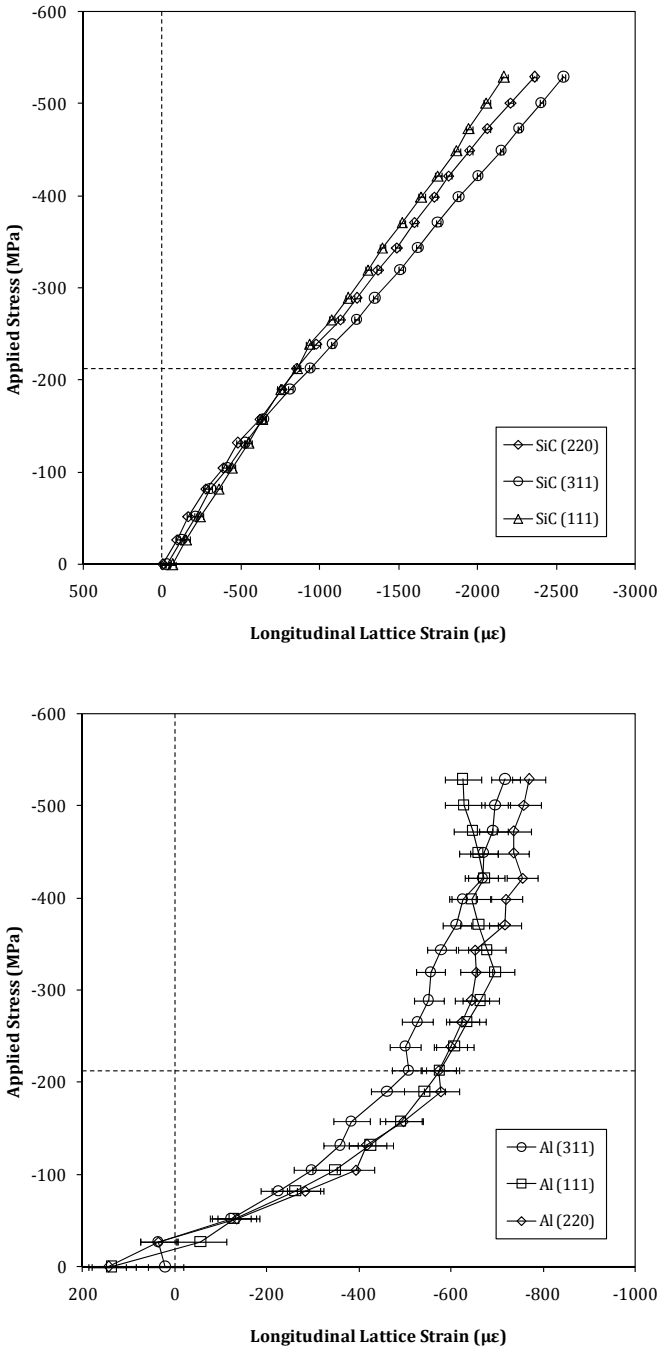

Figure 4.13. Applied compressive stress versus longitudinal lattice strain for the (top) SiC (111), (220) and (311) reflections and (bottom) Al (111), (220) and (311) reflections with the beam parallel to the TA direction. The horizontal dashed line (-213 MPa) indicates approximately the transition from elastic to plastic deformation.

4.4. Discussion

4.4.1. Elastic Behavior

In addition to conditions for transversely isotropic materials identified in Equation 4.4, $C_{11} = C_{22}$ and $C_{44} = C_{55}$ are also true in the case of transverse isotropy. Although the values of C_{11} and C_{22} (155 GPa and 124 GPa) differ by more than 30 GPa, transverse isotropy was assumed for the sake of simplicity. The composites exhibit moduli lower than those predicted by Halpin-Tsai due to the presence of residual carbon, porosity and the non-ideal microstructure of the MCCs, which contain non-linear and non-parallel Al-filled pores.

The pulse echo results also show a difference in the transverse moduli: E_{Radial} = 119 GPa and $E_{Tangential}$ = 91 GPa. A possible explanation for this difference can be drawn from the properties of the wood starting material. Wood is typically stiffer when loaded radially as opposed to tangentially (Price 1928). The rays, visible in Figure 3.1, have a higher density than the surrounding channels and act as reinforcements when loading is in the radial direction. The same reasoning can be used for the MCCs because the structure of the wood is maintained throughout the process steps leading to the composites.

The results for the modulus in bending (Figure 4.8) were higher at ambient temperature than the pulse echo results (Table 4.2), but the composites used in bending contained less residual porosity and carbon (Table 3.1). The elastic moduli of the MCCs in the longitudinal direction also compared well to results published for SiC particle-reinforced Al-Si-Mg MCCs prepared by pressureless infiltration. Moduli from 165 GPa to 226 GPa were reported for samples with 41-54 vol.% SiC and 3-8 vol.% porosity (Pech-Canul *et al.* 2000b). The flexural moduli were also similar to those measured by T. S. Orlova

and colleagues who used dynamic resonance techniques to measure the modulus and internal friction of the Al-Si-Mg and the BE- and SA-MCCs (see Appendix A).

In order to gauge the Al-alloy contribution to the composite stiffness, a comparison with the porous wood-derived SiC is needed. The elastic moduli of BE- and SA-SiC, measured in compression with the applied load in the axial direction, were 116 GPa and 23 GPa, respectively, while the moduli with the load perpendicular to the pore channels was 16 GPa and 7 GPa (Kaul *et al.* 2006). These data indicated that the microstructure, i.e. spatial distribution of pores for a given volume fraction of porosity, strongly influenced the SiC mechanical properties, but this was not the case for the MCCs.

The flexural moduli for the BE- and SA-MCCs were equal within experimental error, which suggests that eliminating the porosity via aluminum infiltration decreases the influence of the wood characteristics. This leads to a stronger dependence on the volume fractions of the ceramic and metal phases and on the test orientation. The SA-SiC benefits more from the Al-infiltration, where LO and TR moduli were improved by factors of 11 and 18, respectively, as compared to improvements of less than two- and six-fold for the BE-SiC. The larger increases in TR moduli (18 and 6 times greater) versus the LO moduli (11 and <2 times greater) correspond to a reduction in the anisotropy in the moduli of the composites.

The stiffness of porous materials, such as wood-derived SiC, is dependent on microstructural features including the connectivity and thickness of the pore walls, presence of defects, and orientation (Studart *et al.* 2006). Variations in these features can change the dominant deformation mode from stretching to bending and will alter the

stiffness of the material. In contrast, the stiffness of the MCCs is controlled by load transfer between phases, which depends on the spatial distribution of phases (Clyne *et al.* 1993).

In the case of the BE- and SA-MCCs, the microstructure consists of a three-dimensionally continuous SiC phase and long Al alloy fibers oriented in the longitudinal direction. The elastic behavior of this microstructure should follow an isostrain model in the longitudinal direction and an isostress model in the transverse orientations. While agreement between the Halpin-Tsai model and the transverse data is relatively good, the LO data fall well below the predicted stiffnesses. A sensitivity analysis of the Halpin-Tsai equations (Equation 2.16 and 2.17) can be used to determine if the discrepancy between theory and experiment is due to variability in the data used to predict the LO modulus. By changing one variable at a time in order to best fit the LO experimental data, V_f would have to be ≈ 0.35 (instead of 0.50), E_m would have to be less than 1% of the experimentally measured values or E_f would have to be ≈ 300 GPa. These are unrealistic values as the standard deviation in the experimentally measured porosity, E_m and E_f were only 0.03, 5 GPa, and 32 GPa, respectively. The LO data can be fitted by combining changes in V_f and E_f, but it should be noted that changing these values also affects the relatively good fit of the TR1 and TR2 data. The one variable that can be changed without affecting the fit of the transverse data, ξ, would have to be changed from ∞ to ≈ 5 to fit the LO data.

Another factor that may explain the poorly-fit LO data is misalignment of the Al-filled pores, which is not accounted for by the Halpin-Tsai equations and would decrease the elastic properties of the composites. While the Halpin-Tsai calculations are based on an

ideal structure, the MCCs contain a non-ideal microstructure with non-linear and non-parallel Al-filled pores. The effect of misaligned Al 'fibers' can be calculated according to

$$E_\theta = \left[\frac{m^4}{E_1} + \frac{n^4}{E_2} + \left(\frac{1}{G_6} - \frac{2\nu}{E_1} \right) m^2 n^2 \right] \quad (4.7)$$

where E_θ is the composite modulus with an average fiber misalignment of θ, m and n are the cos(θ) and sin(θ), respectively, E_1 and E_2 are the Voigt and Reuss composite moduli, respectively, G_6 is the composite shear modulus and ν is the Poisson ratio (Chawla 1998). In order to account for the ≈ 20% discrepancy between the LO flexural modulus and the Halpin-Tsai prediction, the average misalignment of the Al-filled pores would have to be approximately 20°. This is unlikely as the maximum misalignment observed in the μCT data was on the order of only 10°. The Halpin-Tsai equations are too insensitive to individual changes in V_f, E_m, E_f, ξ and θ; therefore, the disagreement between theory and experiment is most likely due to the combined effect of variability in experimentally-measured data and the non-parallel and non-linear nature of the Al-filled pores in the wood-derived composites.

4.4.2. Residual Strain & Load Partitioning

As with most MCCs, the large mismatch between the coefficients of thermal expansion (Al: 22 x 10^{-6} /K, SiC: 4.5 x 10^{-6} /K) resulted in residual strains. However, the measured residual strains are small, which indicates that relaxation by matrix plasticity occurred upon cooling by creep at high temperatures and then microplastic deformation at lower temperatures. The different slopes of the curves in the RA versus TA orientations for the Al

(111) and SiC (111) (Figure 4.12) indicate, similar to the pulse echo results, that the microstructure of the tested sample was not transversely isotropic. Variability in the microstructure (nonlinearity of the Al-filled pores and the relatively dense late wood and ray regions, which were observed with both microscopy and μCT), could lead to a non-uniform stress distribution through the sample. This could cause the difference in the bulk longitudinal lattice strain measurements, which should be equivalent in a transversely isotropic system, because of the different sample volumes in the two sample orientations. The slopes of the Al curves in the elastic-region of Figures 4.12 and 4.13 are all greater than the modulus of the bulk alloy. This indicates that the apparent strain of the Al in the composite is less than what would be experienced by the bulk alloy for a given applied stress. On the other hand, the slopes of the SiC curves, which are less than the modulus of the bulk SiC, indicate that load transfer is occurring from the Al to the SiC and the SiC in the composite is undergoing greater strain compared to bulk (dense) SiC at an equal applied stress.

The deviation from linear-elastic behavior of the Al phase (Figure 4.12) indicates the onset of Al plasticity and load transfer from the aluminum to the SiC. The average principal stress in each phase can be estimated from the measured strains according to

$$\sigma_1 = \frac{E}{1+\nu}\varepsilon_1 + \frac{\nu E}{(1+\nu)(1-2\nu)}(\varepsilon_1 + \varepsilon_2 + \varepsilon_3) \tag{4.8a}$$

$$\sigma_2 = \frac{E}{1+\nu}\varepsilon_2 + \frac{\nu E}{(1+\nu)(1-2\nu)}(\varepsilon_1 + \varepsilon_2 + \varepsilon_3) \tag{4.8b}$$

$$\sigma_3 = \frac{E}{1+\nu}\varepsilon_3 + \frac{\nu E}{(1+\nu)(1-2\nu)}(\varepsilon_1 + \varepsilon_2 + \varepsilon_3) \tag{4.8c}$$

where σ_1 is the longitudinal stress, σ_2 and σ_3 are the transverse stresses, $\varepsilon_{1\text{-}3}$ are the measured strains, and E and ν are the modulus and Poisson's ratio of the crystallographic plane of the material under consideration, respectively (Meyers *et al.* 1984). These stresses can then be used to calculate the effective von Mises stress, σ_{eff}, for each phase

$$\sigma_{eff} = \frac{1}{\sqrt{2}}\left[(\sigma_1 - \sigma_2)^2 + (\sigma_2 - \sigma_3)^2 + (\sigma_3 - \sigma_1)^2\right]^{1/2} \tag{4.9}$$

which is a measure of the load partitioning occurring between phases. The von Mises effective stress of a monolithic material under uniaxial load will be equal to the applied stress, σ_{app}. However, in composite materials exhibiting stiffness mismatch, σ_{eff} of the different phases can deviate from σ_{app}. As load transfer occurs from the compliant to the stiff phase, the difference between the effective stress of the stiff versus the compliant phase will increase as the applied load increases.

A plot of the effective stress versus applied stress is shown in Figure 4.14 for data from the SiC (111) and Al (111) reflections (similar behavior was observed for the (220) and (311) reflections). In the BE-MMC under an applied compressive stress of 52 MPa, the SiC (111) plane exhibits an effective stress of 118 MPa while the Al (111) plane exhibits an effective stress of 17 MPa, which is 7 times lower than the SiC (111). At the last recorded load of 529 MPa, the SiC (111) and Al (111) effective stresses are 855 MPa and 71 MPa, a difference of a factor of 12 between the two phases. The transition from elastic to plastic behavior can be measured by plotting the von Mises effective stress of the Al versus the measured Al (111) lattice strain. This transition occurred after the ninth loading point, at an effective stress of 46 MPa and an applied stress of -213 MPa, and corresponded to the

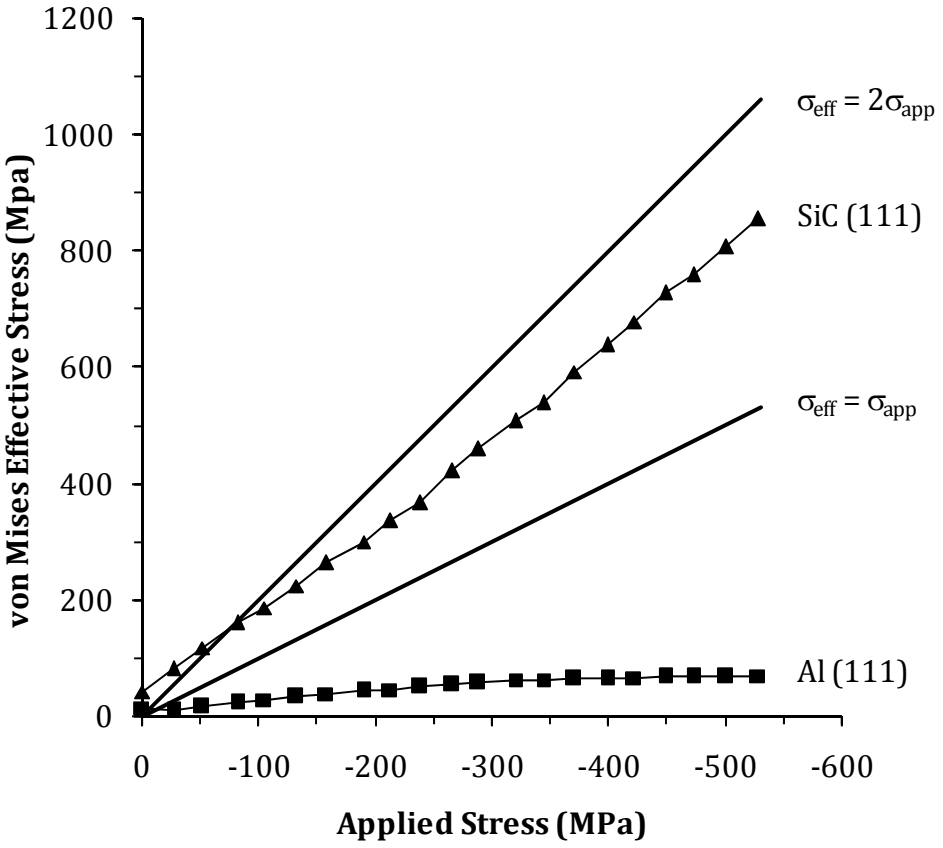

Figure 4.14. Von Mises effective stress versus applied stress for the Al and SiC phases. The solid lines correspond to 1:1 and 2:1 ratios between the effective and applied stresses.

small decrease in the slope of the SiC curves in Figure 4.12 and the increased slope of the SiC curve in Figure 4.14. The Al yield point, at an effective stress of 46 MPa, was greater than that measured of the bulk alloy in tension (≈ 35 MPa). This could be caused by the microstructural differences in the composite versus the bulk alloy (Figure 3.9) or the constrained nature of the metal in the composite, which leads to different load-displacement behavior (Ashby *et al.* 1989).

In Figure 4.13, the linearity of the SiC (111), (220) and (311) curves corresponds to an elastic response throughout loading. The slight increase in the slope of the SiC (111) curve indicates that load is being transferred from the (111)-oriented grains to the (220) and (311) grains, the curves of which slightly decrease. In the plastic region of the aluminum curves, the load is redistributed from the grains producing the (111) reflection to the grains producing the (220) and (311) reflections; behavior that has been previously observed (Clausen 1997).

4.4.3. Strength & Fracture Mechanisms

At room temperature, the load-displacement curves corresponding to the bending and fracture tests of the Al alloy were linear elastic until fracture. This brittle behavior is a result of the presence of the large primary Si crystals. In fact, the strain-to-failure in tension of the Al-Si-Mg alloy at 25°C was only 0.7% and the ductility increased with temperature up to 8.5% at 400°C. Composite specimens tested in the longitudinal orientation also presented linear elastic behavior at ambient temperature, and the non-linearity in the load-displacement curves was limited even at 500°C (Figure 4.9). This

behavior reflects the presence of a continuous SiC phase which limits macroscopic plastic deformation; however, differences in the microscopic fracture mechanisms between ambient and elevated temperature were observed. While the Al fibers in the fracture surfaces showed little evidence of plastic deformation at 25°C (Figure 4.15a), the infiltrated Al tended to span the crack opening and then fail by ductile mechanisms of void nucleation and growth at high temperatures (Figure 4.15b). Figure 4.15c presents a side view in which a bridging metal inclusion has completely failed during a test at 500°C. The data from the current study agree with data for SiC_p-reinforced Al-Si-Mg MCCs with 41-54 vol.% SiC and 3-8 vol.% residual porosity, which were between 183 MPa and 298 MPa (Pech-Canul *et al.* 2000b).

The composite specimens tested in the transverse orientations presented brittle behavior at ambient temperature, which corresponds with the straight crack paths observed and with the brittle appearance of the fracture surfaces, as shown in Figure 4.16a of a BE-MCC tested in the TR1 orientation. Extensive contribution of the plastic deformation of the Al alloy to the non-linear behavior in the load-displacement curves was observed at high-temperature (Figures 4.16b and 4.16c). The bending strength in the TR1 and TR2 orientations of the beech-based composites at 25°C were equivalent to those measured in specimens infiltrated with pure aluminum, which had strengths of 81 MPa and 92-95 MPa for the TR1 and TR2 orientation, respectively (Herzog *et al.* 2006b). The load-displacement curves of the pure Al-MCCs also exhibited serrations, which was attributed to the varying density resulting from the growth rings. This is supported by results from the

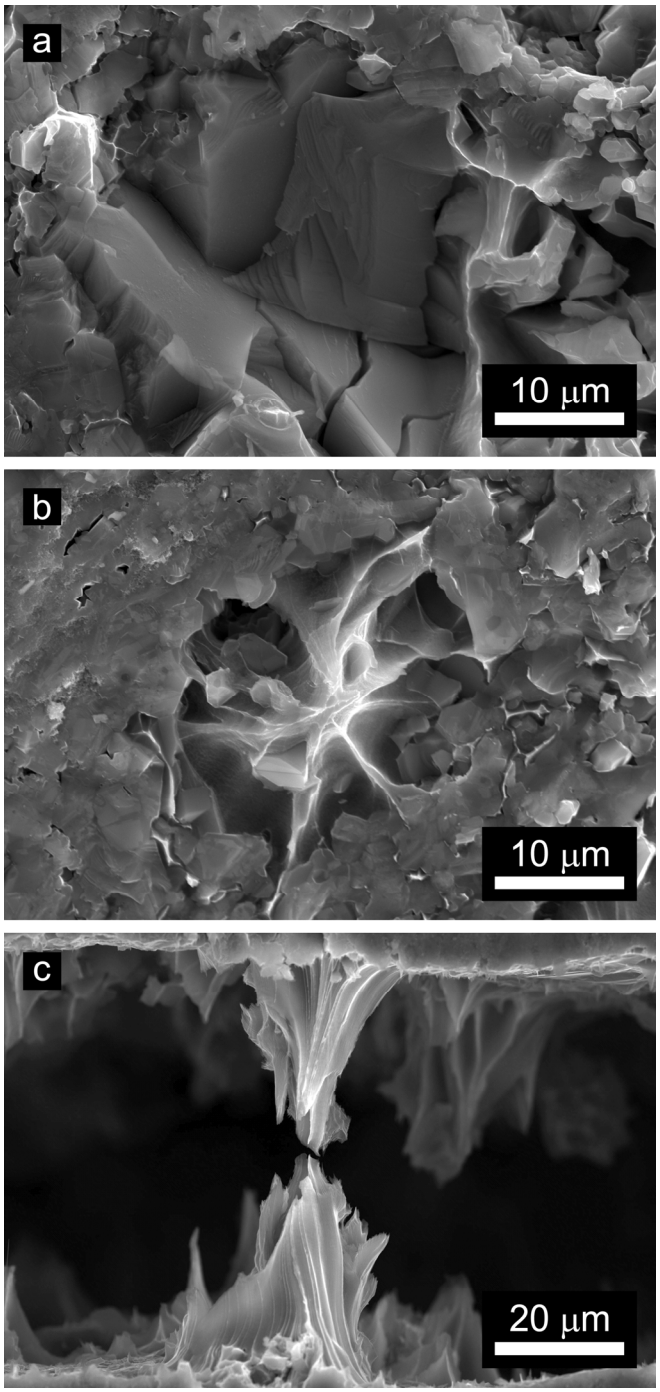

Figure 4.15. SEM micrographs of fractured BE-MCC specimens in the LO orientation: (a) 25°C fracture surface showing the brittle fracture of the metal within a pore, (b) 500°C fracture surface showing the ductile pullout at high-temperature of the metal within a pore and (c) 500°C crack profile showing a failed bridging ligament.

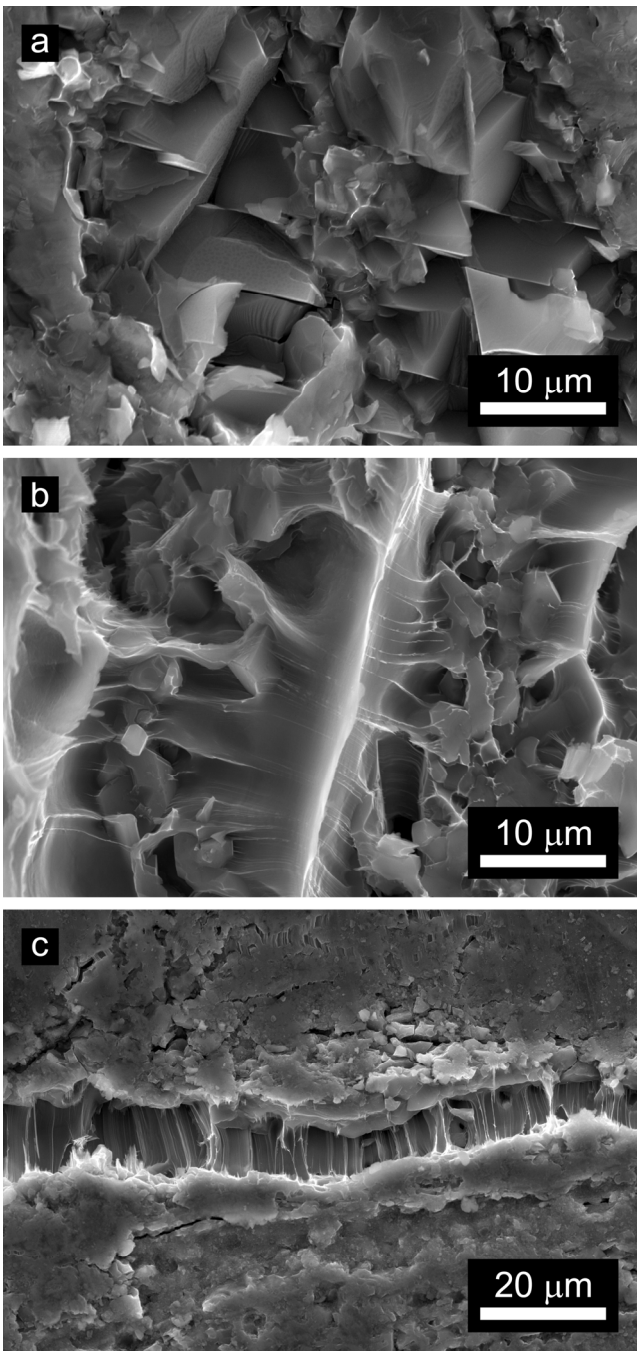

Figure 4.16. SEM micrographs of fractured BE-MCC specimens in the TR1 orientation: (a) 25°C fracture surface showing brittle fracture due to the large Si crystals and Mg_2Si precipitates, (b) 500°C fracture surface showing the ductile behavior of the metal at high temperature and (c) 500°C crack profile showing the Al-Si-Mg alloy spanning the crack width.

current work: the serrations were observed in the BE-TR2 MCCs but not the SA-TR2 specimens, which lacked the repetitive density changes due to growth rings.

The room temperature bending strength of porous beech-derived SiC was reported as 120 MPa and 40 MPa in the longitudinal and transverse orientation, respectively (Hou *et al.* 2007). The BE-MCCs were stronger in both orientations (274 MPa and 104 MPa, respectively), as was the case with the compressive strength (Table 4.1). It is unlikely that the large increases in the composite strengths, which were as much as 16 time stronger than the porous preforms, were caused solely by a significant drop in the load borne by the SiC and increase in the load carried by the Al-Si-Mg. Therefore, a significant effect of the infiltrated metal was to prevent buckling of the SiC until, after load transfer (Figure 4.12), the Al yields and provides no additional support to the SiC. This is supported by the similarities between the failure mechanisms of the porous SiC (Kaul *et al.* 2006) and the composites. In both cases, the relatively dense regions of SiC, which corresponded to late wood or rays, served as failure initiation sites due to the increased amounts of residual carbon and porosity (in the composites) in those regions. Also, at 500°C, where the load-bearing capacity of the Al-alloy is negligible, the flexural strength of the BE-MCCs (LO: 153 ± 11 MPa, TR1: 64 ± 9 MPa, TR2: 60 ± 7 MPa) is reduced to values that are equivalent, within experimental error, to the room-temperature strength reported by Hou *et al.* (2007).

4.4.4. Fracture Toughness

The room-temperature toughness of porous wood-derived SiC was reported as 1.25 MPa·m½ in the longitudinal orientation and 0.59 MPa·m½ and 0.24 MPa·m½ in transverse orientations for porous BE- and SA-SiC (Kaul *et al.* 2006), respectively, and the toughness of bulk SiC is 2.4 MPa·m½ (Faber *et al.* 1983). Although the toughness of the Al alloy was poor due to the presence of the large Si crystals and Mg_2Si precipitates, the toughness increased significantly with the Al-infiltration. Several toughening mechanisms could contribute to the toughness of the Al/SiC composites including metal deformation, Al-fiber fracture, interfacial debonding, frictional sliding/fiber pullout, crack deflection and crack shielding (Hull *et al.* 1981; Lawn 1993). Only insignificant amounts of debonding between the Al and SiC were observed, and no evidence of fiber pullout was observed in microscopy of fractured samples. Some crack deflection was observed in the TR1 and TR2 samples but only at room temperature: at higher temperatures, cracks propagated through the softened metal. Therefore, the increased toughness of the composites is most likely due to the deformation and fracture of the infiltrated aluminum.

Based on experimental evidence (Figure 4.15c), the increase in toughness in the longitudinal orientation was due to the bridging effect of the infiltrated Al within the pores. The metal in the pores acted as constrained fibers that were stretched and absorbed energy as the crack opened, which contributed to the toughness. The contribution of this toughening mechanism was modeled by Ashby *et al.* (1989) as

$$\Delta K_{IC} = E\left[CV_f \frac{\sigma_y}{E} a_0\right]^{1/2} \tag{4.10}$$

where E is the elastic modulus of the metal, V_f is the area fraction of metal intersected by a crack, σ_y is the yield stress of the metal, a_0 is the radius of the metal inclusion, and C stands for a constant which depends on the constraint of the metal within the ceramic and is approximated as

$$C = 2.5\frac{u^*}{a_0} \tag{4.11}$$

where u* is the crack opening displacement at failure of a bridging ligament (Ashby *et al.* 1989). This constant depends on only the interface strength and is independent of the diameter of the inclusion. For this study, E and σ_y were measured using tensile tests of the bulk Al-alloy. The ratio u^*/a_0 was calculated by using the SEM and analysis software (Quartz PCI, Quartz Imaging Corp., Vancouver, BC) to measure the radius and extent of protrusion of failed Al bridges from images of crack profiles and fracture surfaces of specimens fractured at each temperature.

Equation 4.10 considers a composite with inclusions of uniform size, a_0, representing a certain volume fraction, V_f, but the BE- and SA-MCCs present a non-ideal situation with varying amounts of irregularly-shaped inclusions of different sizes. To account for this, a midpoint Riemann Sum was calculated using the incremental pore volume fraction versus pore diameter data for the BE- and SA-SiC (Figure 3.2), and this was added to the toughness of the porous SiC (1.25 MPa·m½ and 1.36 MPa·m½ for the BE- and SA-SiC, respectively (Kaul *et al.* 2006)) to calculate the total toughness of the composites,

$$K_{IC} = E\left[C\frac{\sigma_y}{E}\right]^{1/2} \cdot \sum\left[V_f a_0\right]^{1/2} + K_{IC,SiC} \tag{4.12}$$

where $K_{IC,SiC}$ is the toughness of the porous SiC.

The predictions of the modified Ashby model are plotted in Figure 4.11 together with the experimental results, and they are in relatively good agreement. It is important to note that the model predicts a higher toughness for the SA-MCCs due to the larger pore radius and this is confirmed by the experimental results at all but 200°C. The application of Equation 4.12 can be easily extended to SiC derived from other wood types. In addition to beech and sapele, Kaul *et al.* also measured the toughness of red oak (RO), mahogany (MA), and poplar (PO) SiC materials (Kaul *et al.* 2006). Micrographs and pore size distributions of these materials are shown in Figure 4.17, and Table 4.3 lists the porosity and toughness of each of the porous SiC materials.

Table 4.3. The porosity of wood-derived silicon carbide measured with mercury porosimetry and the fracture toughness of the porous SiC from Kaul *et al.* (2006).

Wood Precursor	SiC Porosity (vol. %)	Fracture Toughness ($MPa \cdot m^{1/2}$)
Beech	50	1.25
Mahogany	61	0.97
Poplar	70	0.88
Red Oak	56	1.35
Sapele	51	1.36

The Ashby model predictions, shown in Figure 4.18 for all five woods, can be used to make several comparisons. While poplar and beech have similar pore size distributions, a PO-MCC is predicted to be tougher due to the higher PO-SiC porosity, which would result in the infiltration of more aluminum. The RO-SiC and SA-SiC have similar porosities and

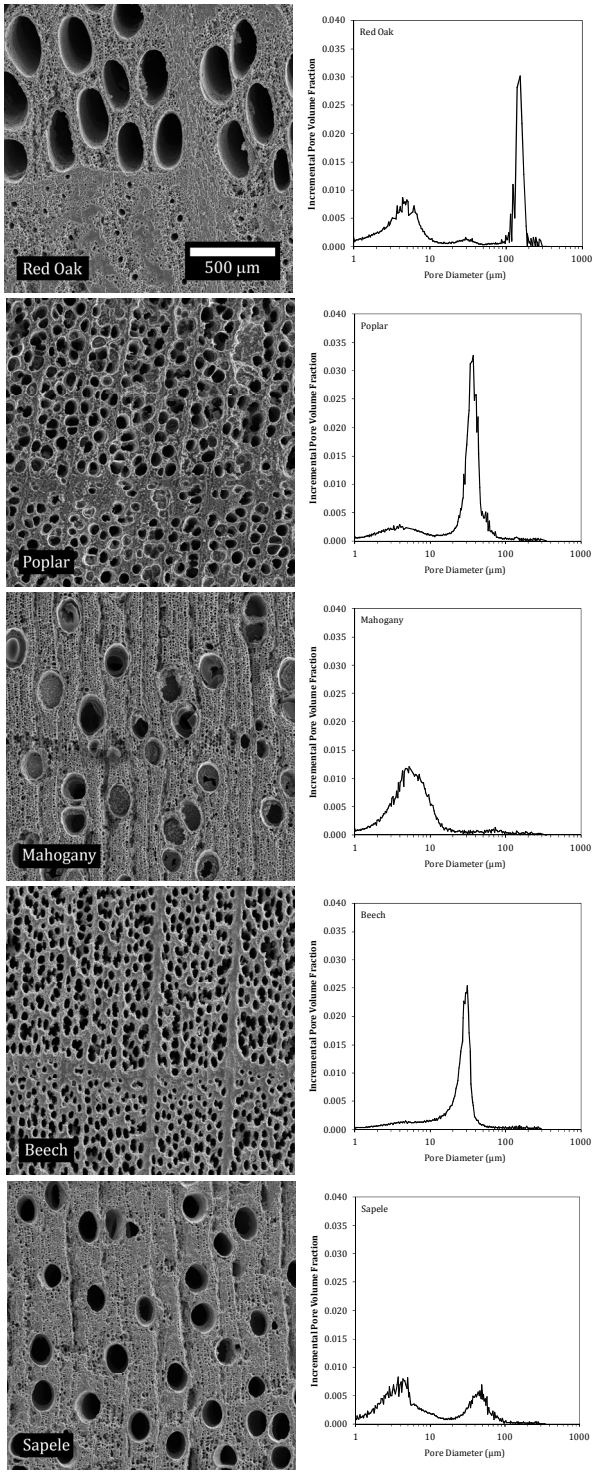

Figure 4.17. SEM micrographs and incremental pore size distributions of SiC derived from red oak, poplar, mahogany, beech, and sapele.

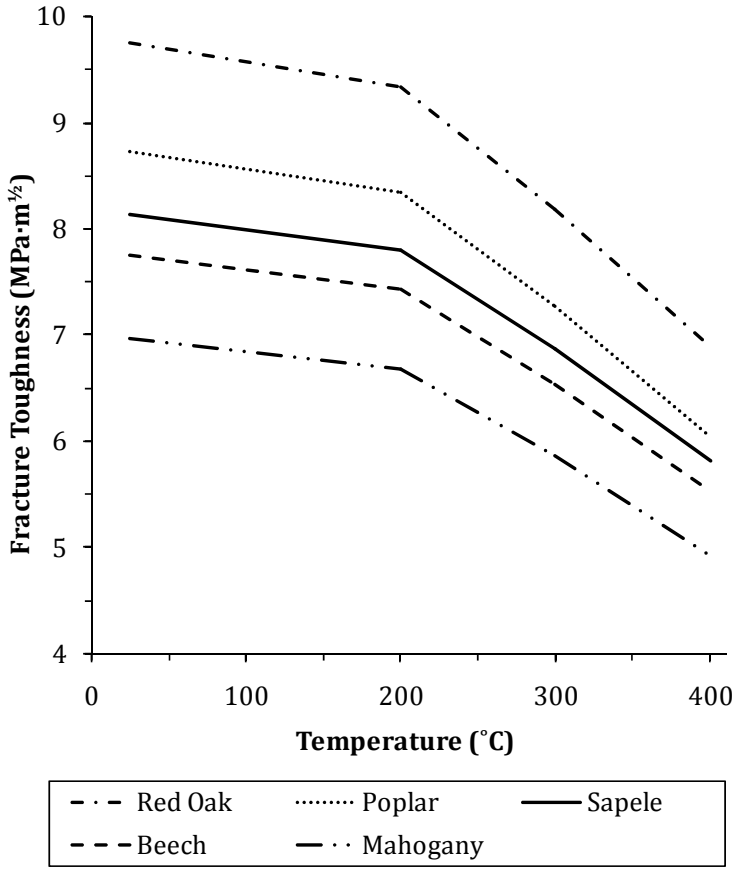

Figure 4.18. Predictions of fracture toughness versus temperature for five different wood-derived SiC MMCs based on the Ashby *et al.* (1989) model.

toughnesses, but the large pores in the RO-SiC would result in a greater toughness. Despite a porosity of ≈ 60% and a microstructure similar to that of sapele, the predicted toughness of a composite made from the MA-SiC is less that of the other composites because the majority of porosity is accounted for by small-diameter pores. The apparent discrepancy between the pore size distribution and the microstructure is due to necks in the large diameter pores. The necks increase the pressure required to force the mercury into the pores and results in an underestimation of the porosity contribution from the large-diameter pores.

The Ashby model also lends insight into ways to further increase the toughness of the composites. With regards to the SiC preforms, greater amounts of porosity and larger-diameter pores will increase the toughness of the composites, i.e. the toughness increases as the magnitude of $\sum[V_f a_0]^{1/2}$ increases. The toughness could also be improved by increasing the Al alloy yield strength, σ_y, which could be accomplished by solutionizing and aging the Si and Mg_2Si precipitates (Meyers *et al.* 1984; Clyne *et al.* 1993).

4.5. Summary

The mechanical properties of the Al/SiC MCCs were investigated by measuring the compressive strength, flexural properties, ultrasonic modulus, and load partitioning. The modulus, strength and toughness in the longitudinal direction were similar to those reported in metal-ceramic composites with equivalent volume fractions of both phases. The corresponding properties in the transverse direction were lower and this behavior reproduced the differences observed in the properties of the porous SiC. Overall, the room

temperature strength and toughness were maintained up to 200°C and then decreased with increasing temperatures.

The analysis of the experimental results showed that the deformation of the composites in the longitudinal direction was controlled by the rigid SiC skeleton, leading to brittle behavior throughout the entire temperature range. Although load transfer from the Al to the SiC was evident, the longitudinal composite stiffness was below that predicted by Halpin-Tsai due to the non-ideal microstructure. The stiffness of the TR1 and TR2 MCCs were closer to the Halpin-Tsai model for the transverse stiffness of a uniaxial composite. Moreover, the increase in longitudinal toughness due to the Al followed the predictions of Ashby's model for toughening ceramics by incorporating ductile inclusions.

5. Copper/Carbon Composites

5.1. Introduction

Technological advances, such as the progressive miniaturization of electronics, result in greater heat fluxes and the need to transport that heat away from critical components. Traditional heat management materials, such as copper and aluminum, have high thermal conductivities (Table 5.1), but also have relatively high coefficients of thermal expansion (CTE).

Table 5.1. Properties of materials commonly used in thermal management applications (Zweben 1992).

Material	Thermal Conductivity (W/m·K)	CTE (10^{-6}/K)	Density (g/cm^3)	Modulus (GPa)
Copper	400	17	8.9	117
Aluminum	230	23	2.7	69
Fe-Ni	17	6	8.3	131
Cu-W	167	7	16.6	248
Cu-Mo	184	7	10.0	282

The high CTEs can lead to mismatch stresses and component failure, especially in electronics applications, for which typical substrates have CTEs of only 4-7 x 10^{-6}/K (Zweben 1998). To reduce the CTE mismatch, an iron-nickel alloy with a CTE of just 6 x 10^{-6} /K, Kovar®, was developed, but the trade-off was a thermal conductivity an order of magnitude lower than that of aluminum. Materials with both a high thermal conductivity and low CTE were made by combining copper with tungsten or molybdenum. While the conductivity of these materials is near that of aluminum, the high density limits the range of practical applications.

The attractiveness of composites for thermal management comes from the ability to make high thermal conductivity materials with low densities and a tailorable CTE. Carbon-reinforced copper composites are of particular interest due to the decreased density and CTE resulting from the incorporation of carbon. Also, the conductivity of some forms of graphite is higher than that of copper, which results in a composite conductivity equal to or even greater than that of the bulk copper. In some applications, where structural properties are also important, composites offer the benefit of improved mechanical properties.

The motivation for the work presented in this chapter was to investigate the feasibility of incorporating copper into the wood-derived carbon. The goal was to use a high-purity copper in order to maintain a high thermal conductivity; however, alloys were attractive because they could improve the poor adhesion at the Cu/C interface, which can affect the mechanical and thermal properties (Chung *et al.* 2000).

5.2. Wood-Derived Carbon

5.2.1. Processing

Two woods were pyrolyzed and used for this work: beech (*Fagus sylvatica*) and pine (*Pinus Strobus L.*), a softwood. The woods were heated at 1°C/minute to 1000°C for one hour in an argon atmosphere and then cooled to room temperature at 10°C/minute. After this heat treatment, some of each wood was reheated to 2400°C in an argon atmosphere for 30 minutes (UCAR Carbon Company, Inc., Parma, OH).

5.2.2. Microstructure

Micrographs of the BE and pine (PI) carbon are shown in Figure 5.1, and the porosities and densities, which were measured by mercury porosimetry, are listed in Table 5.2.

Table 5.2. Apparent porosity and specific gravity of beech- and pine-derived carbon pyrolyzed at either 1000°C or 2400°C.

	Apparent Porosity (%)	Apparent Specific Gravity (g/cm^3)
BE-C-1000	65 ± 4	1.48 ± 0.07
BE-C-2400	60 ± 2	1.50 ± 0.05
PI-C-1000	74 ± 1	1.46 ± 0.08
PI-C-2400	77 ± 1	1.56 ± 0.02

The incremental and cumulative pore volume fractions are plotted versus pore diameter in Figure 5.2. Although not visible in the micrographs in Figure 5.1, the pore size distribution below diameters of 1 μm revealed that the beech used in these experiments was slightly different than the carbon used to produce the SiC (Figure 3.2). The PI-C had a bimodal pore size distribution with peaks located at ≈ 5 μm and ≈ 15 μm, and the beech, which was trimodal, had peaks at ≈ 0.01 μm, ≈ 0.5 μm, and ≈ 25 μm. The pine microstructure was more homogeneous than the beech, but there were still clear distinctions between the late wood, which had thicker pore walls, and early wood, which had thinner pore walls.

For both the BE and PI, the microstructure of the carbon heated to 2400°C was, in general, the same as that heated to only 1000°C. The specific gravity of the 2400°C carbon was slightly greater than the 1000°C carbon due to densification as the carbon became more ordered. A representative X-ray diffraction plot of intensity versus 2θ (Rigaku ATX-G,

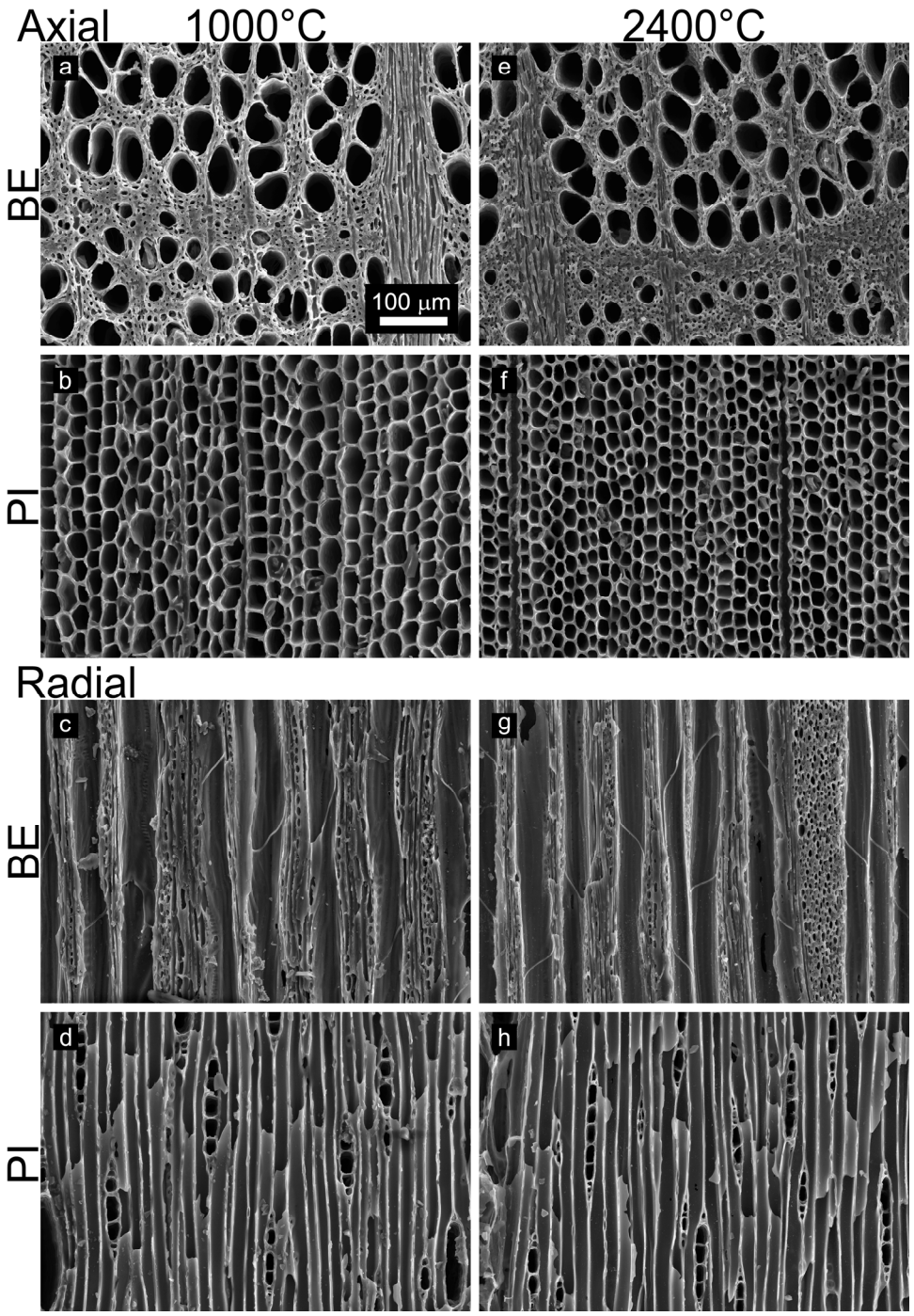

Figure 5.1. SEM micrographs of the beech- and pine-derived carbon. Cross-sections are perpendicular to either the axial direction (top) or radial direction (bottom). Beech and pine micrographs are on the top and bottom of each half, respectively, and the columns depict the carbon pyrolyzed at 1000°C (left) or 2400°C (right).

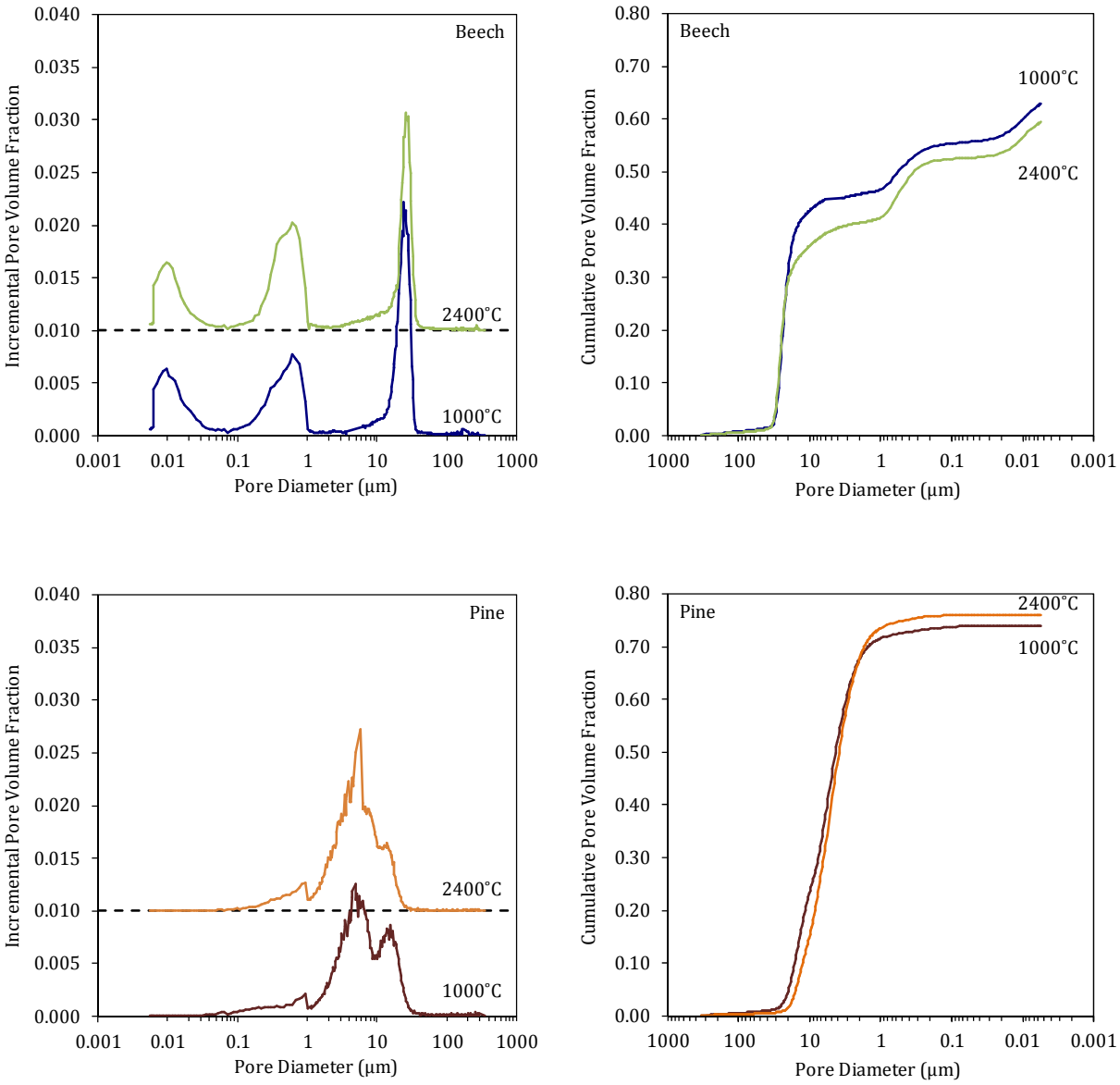

Figure 5.2. Representative plots of the incremental (left) and cumulative (right) pore volume fraction versus pore diameter, measured by mercury intrusion porosimetry, of the beech (top) and pine (bottom) carbon pyrolyzed at 1000°C or 2400°C. For clarity, the incremental 2400°C curves are offset vertically by 0.01.

Tokyo, Japan) for the 2400°C carbon is shown in Figure 5.3 with a representative plot of the 1000°C carbon (Kaul 2007). While the 1000°C pattern was amorphous, a peak was observed in the 2400°C pattern at 25.90° 2θ, which indicated the formation of turbostratic carbon (Oya *et al.* 1982).

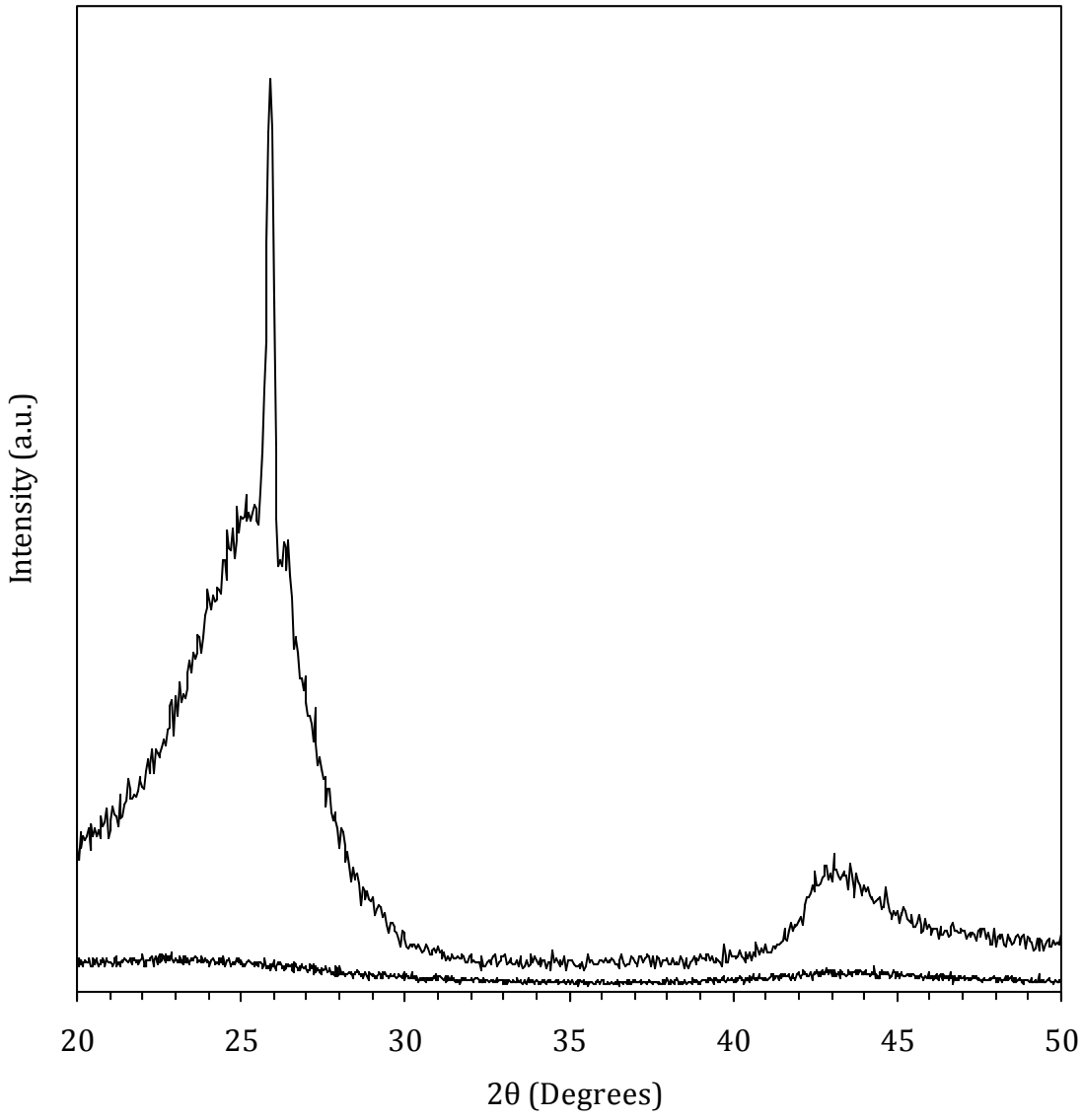

Figure 5.3. Representative X-ray diffraction intensity versus 2θ for the wood pyrolyzed at either 1000°C (Kaul 2007) or 2400°C. The peak in the 2400°C curve, at 25.9° 2θ, indicates the presence of turbostratic carbon.

5.3. Infiltration of Oxygen-Free High-Conductivity Copper (≥ 99.95 wt.% Cu)

5.3.1. Processing & Microstructure

Samples of the BE-C and PI-C were prepared by mechanically grinding the transverse plane (perpendicular to axial direction) with 600 grit SiC paper. After drying, they were infiltrated with oxygen-free high-conductivity copper (OFHC) by MMCC, Inc. (Waltham, MA) using their proprietary Advanced Pressure Infiltration Casting - APIC™ process. Figure 5.4 shows representative transverse sections of the four composite materials. While a majority of the pore space was infiltrated with copper, all four composites had residual porosity. The porosity and specific gravity of the composites, measured using Archimedes' method, are listed in Table 5.3.

Table 5.3. Apparent porosity and specific gravity of OFHC copper/carbon composites.

	Apparent Porosity (%)	Apparent Specific Gravity (g/cm^3)
BE-C-1000	9	4.7
BE-C-2400	11	4.9
PI-C-1000	10	6.4
PI-C-2400	6	6.9

As even some of the smallest diameter pores were infiltrated with copper, the pressure was sufficient for complete infiltration. Therefore, the cause of the residual porosity was most likely due to clogging of the pores during sample preparation. While it was thought that grinding the sample faces to a smooth finish would unblock the pores, it may have actually ground off small pieces of carbon that were then trapped in the smaller-diameter pores.

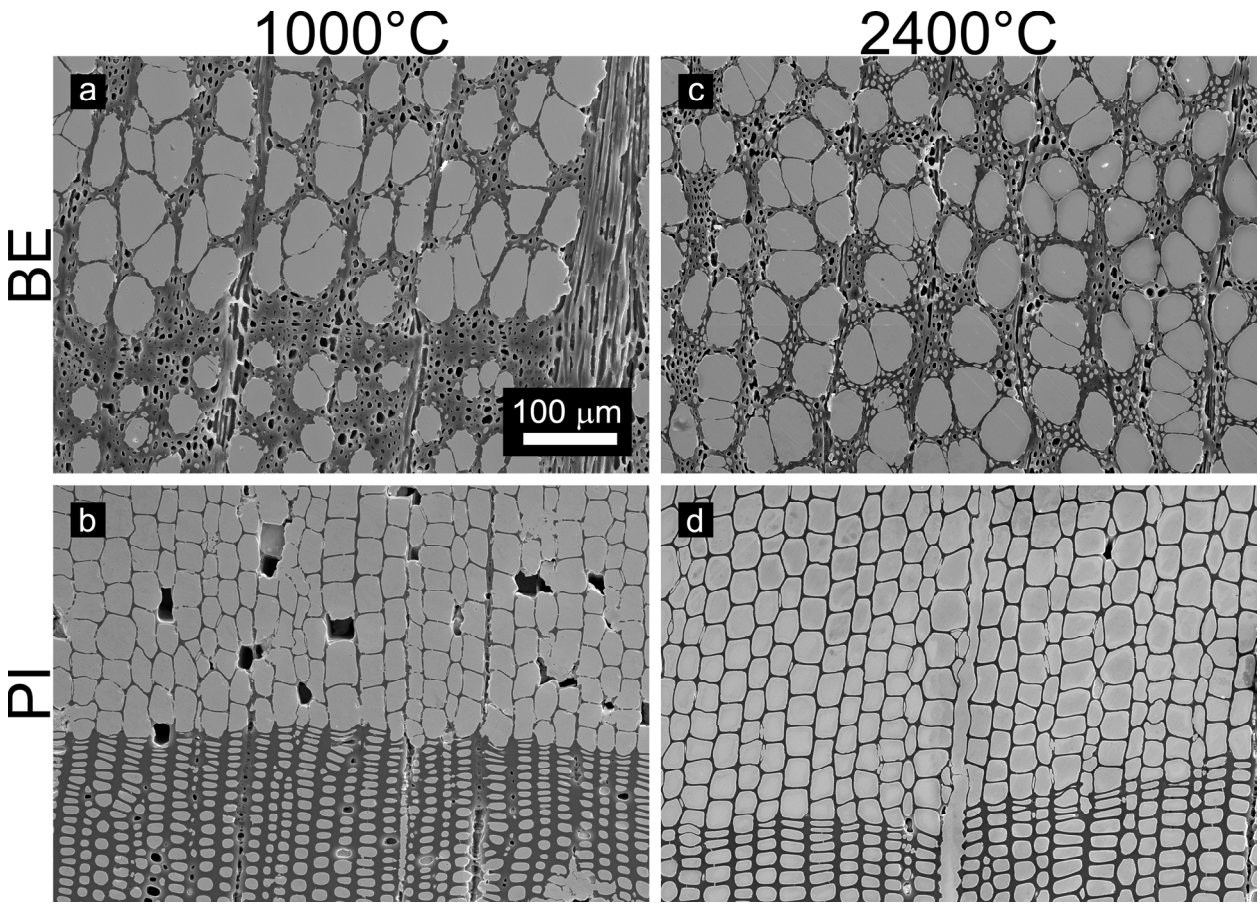

Figure 5.4. SEM micrographs of the beech and pine-derived carbons infiltrated with OFHC Cu. The cross-sections, which are perpendicular to the axial direction, correspond to the beech (top) or pine (bottom) carbon pyrolyzed at 1000°C (left) or 2400°C (right).

Higher magnification microscopy of the composites, shown in Figure 5.5, revealed damage to the carbon performs. Thinner pore-wall sections were fractured and small cracks were visible in some of the thicker carbon regions. Preform damage could be caused by stresses evolved during cooling, due to the thermal mismatch between the OFHC copper ($17x10^{-6}$ /K) and carbon ($2x10^{-6}$ /K). In general, more cracking was observed in pine material, most likely due to the thinner pore-wall material. Fracture of the pore-walls, the thickness of which is characteristic of the wood preform, could be deleterious to mechanical and thermal properties.

Representative longitudinal sections of the composites are shown in Figure 5.6. The poor mechanical bond at the Cu/C interface led to decohesion of the copper. In contrast to sections of the beech samples, which were largely devoid of copper, most of the copper in pine sections remained intact but still deformed from polishing. This is likely due to the greater interconnectivity of copper in the pine composites. These interconnections are also visible in Figure 5.5. The poor Cu/C interface will likely influence the efficiency of load transfer and may impede heat transfer, which will negatively impact the composite properties.

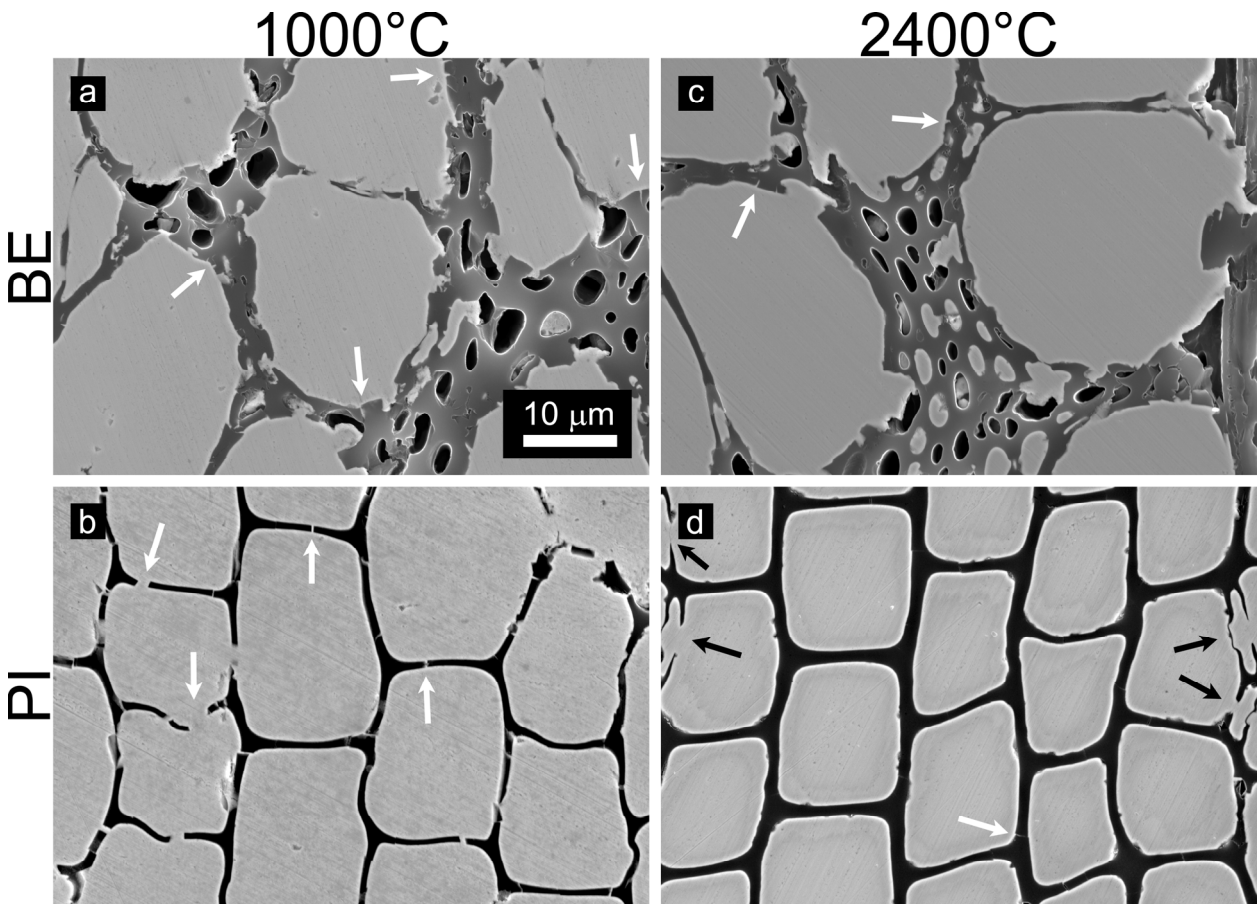

Figure 5.5. SEM micrographs corresponding to the samples in Figure 5.4, but magnified ten-fold. The thin pore walls of the carbon preforms exhibited extensive cracking as indicated by the white arrows. The four black arrows in (d) indicate the locations of transverse interconnections between the Cu-filled pores.

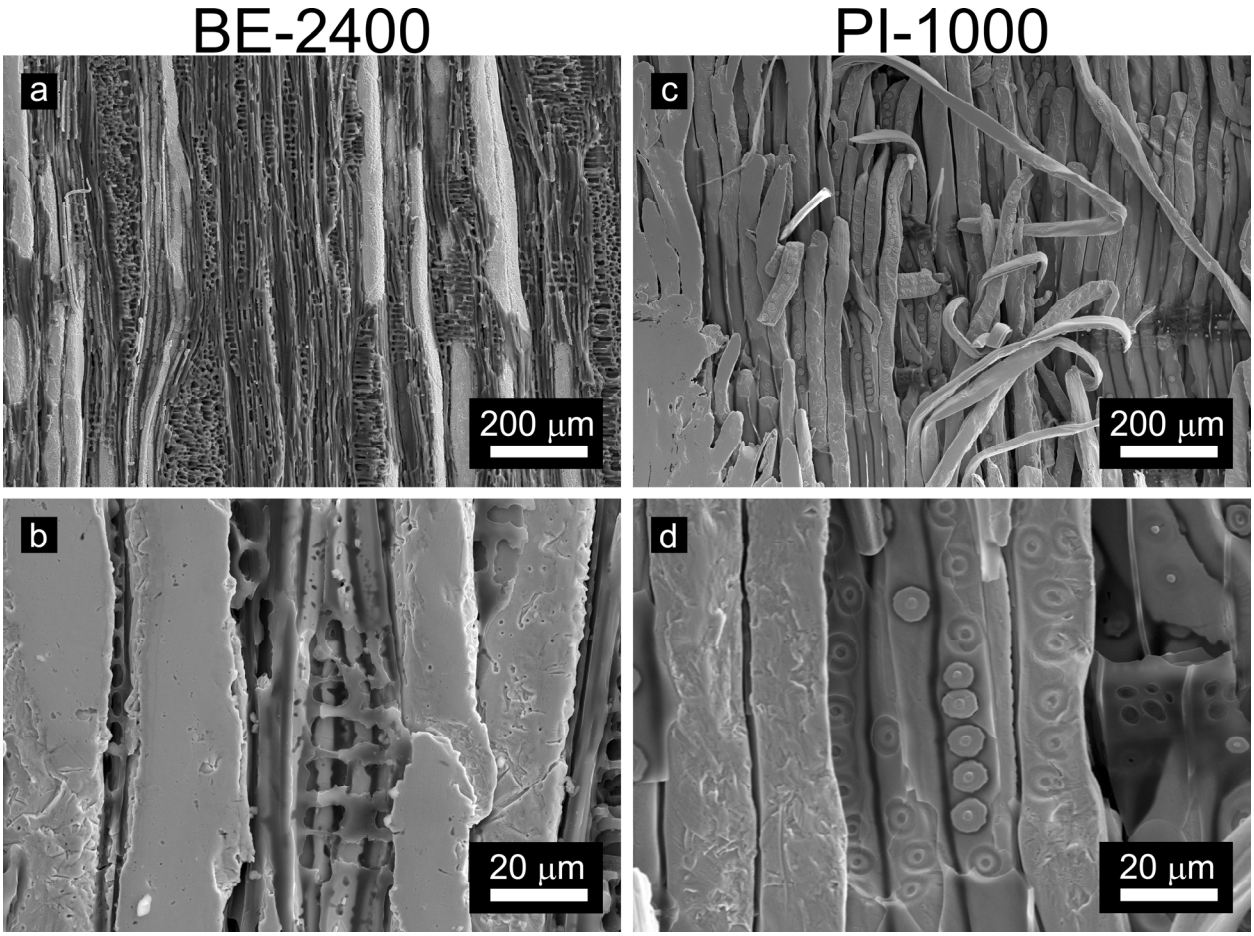

Figure 5.6. Representative SEM micrographs of the OFHC-infiltrated composites. The cross-sections are perpendicular to the radial direction and correspond to composites of either the beech pyrolyzed at 2400°C (a, b) or the pine pyrolyzed at 1000°C (c, d). The poor Cu/C interface resulted in extensive decohesion of the copper. The circular features in (d) correspond to interconnectivity between porosity in the pine-derived carbon.

5.3.2. Theoretical Elastic & Thermal Properties

Theoretical bounds on the axial and transverse mechanical and thermal properties of the composite materials can be calculated using information from Tables 5.4 and the equations in Section 2.1.5. The resulting upper and lower bounds of these calculations for the BE- and PI-1000 carbons, listed in Table 5.5, assume that the Cu-filled pores are continuous and perfectly aligned and that the properties of the copper and carbon do not change with temperature.

Table 5.4. Properties of OFHC copper and amorphous carbon used to predict the composite thermal conductivity, k, coefficient of thermal expansion, α, and elastic modulus, E, of the composites.

	k	α	Poisson	E	Volume Fraction	
	(W/m·K)	(/K)	Ratio	(GPa)	BE-1000	PI-1000
OFHC[a]	385	17×10^{-6}	0.34	117	0.65	0.74
Carbon[b]	2	2×10^{-6}	0.17	29	0.35	0.26

a) OFHC properties from (Davis 2001)
b) Carbon properties from (Kutz 2003; Pappacena *et al.* 2006)

Table 5.5. Predictions of the elastic modulus, E, coefficient of thermal expansion, α, and thermal conductivity, k, for the OFHC Cu and BE- or PI-1000 carbon composites.

E	ROM		Halpin-Tsai
(GPa)	Upper	Lower	Lower
BE-1000	86	57	71
PI-1000	94	65	81

$\alpha \times 10^6$	Schapery		Chamis
(/K)	Upper	Lower	Lower
BE-1000	15	11	8
PI-1000	16	13	10

k	ROM		Halpin-Tsai
(W/m·K)	Upper	Lower	Lower
BE-1000	251	6	149
PI-1000	285	8	189

The different models result in a range of values for the elastic modulus, thermal conductivity and coefficient of thermal expansion. The largest discrepancy occurs for the transverse thermal conductivity calculation: the rule of mixtures predictions are ≈ 25 times less than those calculated with the Halpin-Tsai or Chamis equations. This is due to the large difference in the thermal conductivities of the copper and carbon: as the ratio k_{Cu}/k_C increases, the ratio of the upper to lower ROM bounds also increases at a given carbon volume fraction. It should be noted that these predictions should be used only as a guideline as the predictions of the Al/SiC MCC longitudinal flexural modulus were inaccurate due to the non-ideal microstructure, which will also affect the thermal properties (Pappacena *et al.* 2007).

The specific modulus and thermal conductivity of the OFHC copper, i.e. the respective property normalized by density (ρ_{OFHC} = 8.94 g/cm^3), are 13 GPa/(g/cm^3) and 43

(W/m·K)/(g/cm^3), respectively. The upper bound predictions for the specific properties of the composites are greater than the OFHC. Using the specific gravities listed in Table 5.3, the predicted specific moduli for the BE and PI composites are 18 GPa/(g/cm^3) and 15 GPa/(g/cm^3), respectively. The specific conductivities are 53 (W/m·K)/(g/cm^3) and 45 (W/m·K)/(g/cm^3) for the BE and PI, respectively. Despite the large absolute decreases in stiffness and conductivity, the low density of the carbon results in improvements of the normalized properties. The specific lower bound predictions, however, are less than the OFHC specific properties except in the case of the Halpin-Tsai modulus calculation. For the lower ROM bound, the moduli are 12 GPa/(g/cm^3) and 10 GPa/(g/cm^3) for the BE and PI, and the Halpin-Tsai lower bound predicts specific moduli of 15 GPa/(g/cm^3) and 13 GPa/(g/cm^3). The Chamis and Halpin-Tsai lower bounds result in specific conductivities of 34 (W/m·K)/(g/cm^3) and 32 (W/m·K)/(g/cm^3) for the BE and 30 (W/m·K)/(g/cm^3) and 30 (W/m·K)/(g/cm^3) for the PI, respectively.

As previously mentioned, the preform damage and poor Cu/C interface will also affect these properties. The poor interface can lead to debonding during thermal cycling and generate a thermal contact resistance that decreases the thermal conductivity (Mayerhofer *et al.* 2002). One way to improve both the stiffness and conductivity would be to incorporate a strong interface between the Cu and C. As discussed in Section 2.1.3, this could be accomplished with an alloy containing a carbide-forming element.

5.4. Infiltration of Cu-Cr (Cu - 1 wt.% Cr)

A copper-chromium alloy was of particular interest because Cr is known to form chromium carbide, Cr_3C_2, which has a relatively high thermal conductivity, 190 W/m·K, and elastic modulus of 373 GPa (Silvain *et al.* 2000).

5.4.1. Experimental Methods

Wetting experiments, similar to those of Silvain *et al.*, were conducted with the wood-derived carbon (Silvain *et al.* 2000). Both Cu (>99 wt.%) and a Cu-1 wt.% Cr alloy were tested. Buttons of the metals weighing approximately 10 g were melted in an arc melter (Edmund Bühler, Germany). Similar to the pressureless infiltration experiments described in Sections 3.3 and 3.4, the buttons were placed on top of pieces of carbon inside an alumina crucible. The samples were heated in argon at 10°C/minute to 1150°C for two hours and then cooled to room temperature at 10°C/minute.

5.4.2. Results & Discussion

As expected, the unalloyed copper did not wet or infiltrate the carbon preforms. However, the Cu-Cr infiltrated into both the BE- and PI-C samples, as shown in Figure 5.7. At the top surface of the carbon preforms, all of the carbon had reacted and formed Cr_3C_2, and the carbide thickness decreased with increasing depth into the pores. Small micrometer-sized porosity was observed within the carbide layer. This observation corresponds to other C/Cr reactivity studies (Mortimer *et al.* 1970; Devincent *et al.* 1993), and could result from the 17% volume reduction associated with the $C \rightarrow Cr_3C_2$ reaction.

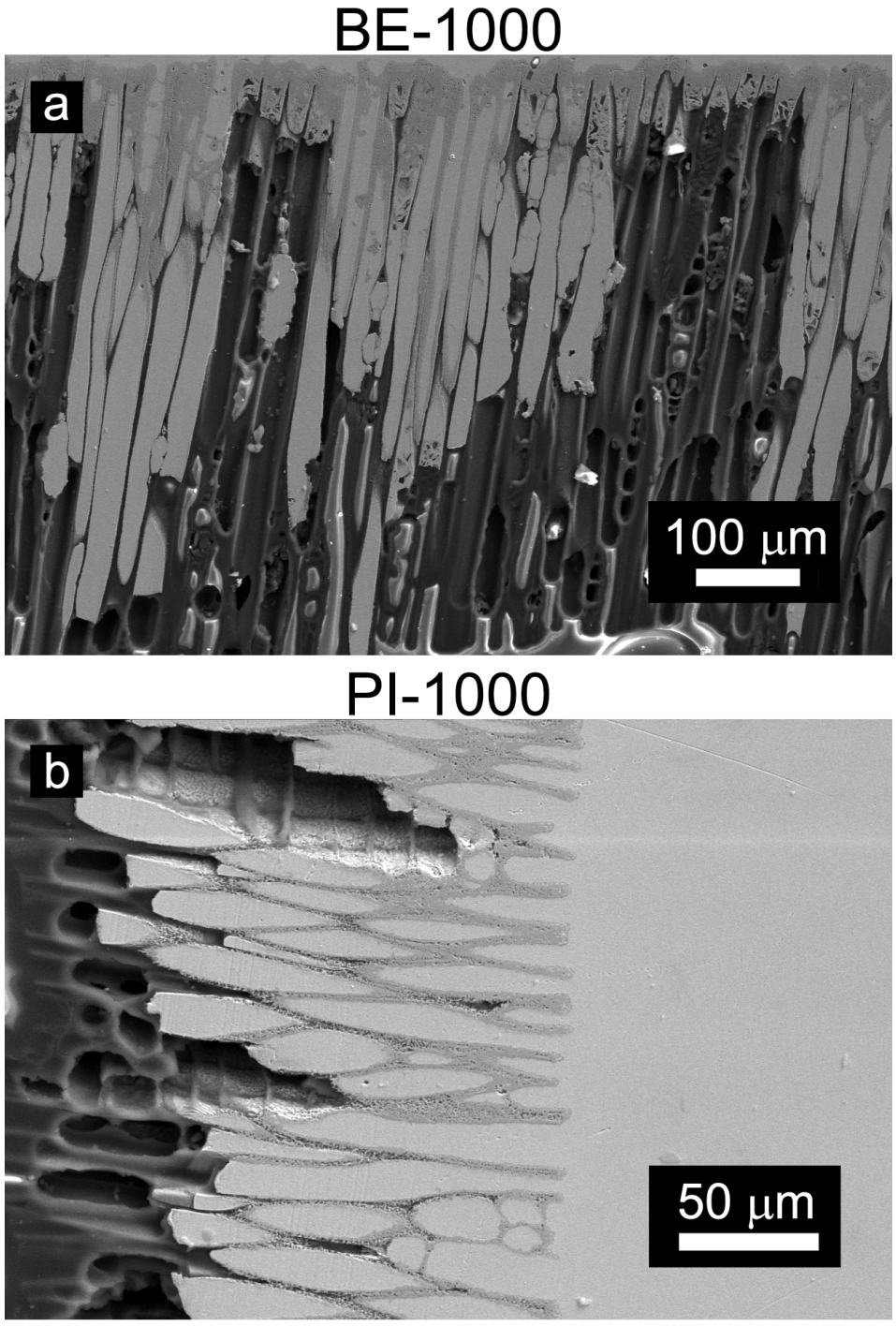

Figure 5.7. SEM micrographs of longitudinal cross-sections of beech- and pine-derived (1000°C) carbon samples infiltrated with the Cu-Cr alloy without applied pressure. The three grayscale levels correspond, from dark to light, to the carbon, Cr_3C_2 and copper, respectively.

Infiltration occurred only where the Cr reacted with the carbon to form Cr_3C_2. If the hold-time were increased beyond two hours, the infiltration would have continued. Complete infiltration would occur in the extreme case where the carbon preform was the limiting reagent, but the resulting composite would be Cu/Cr_3C_2 and not Cu/C.

While complete Cr_3C_2 conversion was undesirable, Figure 5.7 distinctly shows an advantage of the carbide formation: the infiltrated copper is well-adhered to the pore walls. A thin carbide layer would be ideal because Cr_3C_2 is brittle and a thick layer could decrease mechanical properties and would result in more of the observed micron-size porosity. Also, if the wood-derived carbon were converted into high-conductivity graphite, the carbide layer would act to decrease the composite thermal conductivity.

5.5. Infiltration of C18150 (Cu - 1 wt.% Cr - 0.1 wt.% Zr)

A thin carbide reaction layer could be formed by using pressurized-infiltration to quickly infiltrate molten copper into the carbon preform and then quenching the system to stop the C→Cr_3C_2 reaction. For the following experiments, a Cu-Cr-Zr alloy (C18150, E = 130 GPa, k = 324 W/m·K) was used because it was commercially available and would have a homogeneous Cr distribution as opposed to the arc-melted Cu-Cr alloy (Davis 2001). Also, this alloy is similar to alloys used in the commercial production of Cu/C composites (Cornie *et al.* 2003).

5.5.1. Experimental Methods

An ultrasonic drill press (Branson Ultrasonics Corp, Danbury, CT) was used to make cylinders of the BE- and PI-C measuring 12 mm in diameter and ≈ 20 mm in length. Flat-bottom quartz tubes (National Scientific Co., Quakertown, PA) with an inner diameter of 13 mm and length of 150 mm were used as crucibles. An alumina disc measuring 11 mm in diameter by ≈ 3 mm thick was placed on top of the carbon preform to prevent premature contact and reaction with the C18150 alloy, which measured 12.4 mm in diameter by 70 mm in length (National Bronze and Metals, Inc., Houston, TX). In order to prevent the alumina disc from floating, coarse tungsten powder (250 μm ≤ d ≤ 1.68 mm), in an amount sufficient (≈ 7 g) to offset the alumina disc's buoyancy force, was placed between the alumina and C18150.

A custom box-furnace equipped with an alumina tube and vacuum pump (DeFouw 2007) was used to heat the sample under vacuum (≤ 1.3×10^{-9} MPa) to 1250°C. After a 1.5 hour hold, argon was used to pressurize the system to slightly below ambient pressure (≈ 0.07 MPa); positive pressures could not be applied to the alumina tube. The system was then either cooled slowly to room temperature, or, after 30 seconds, the crucible was removed from the furnace and quenched in water.

5.5.2. Results & Discussion

Neither the pine nor beech preforms were fully infiltrated with C18150, and the carbon pyrolyzed at either 2400°C or 1000°C exhibited the same behavior. Representative micrographs of the quenched PI-C-1000 and BE-C-2400 are shown in Figure 5.8. Only the

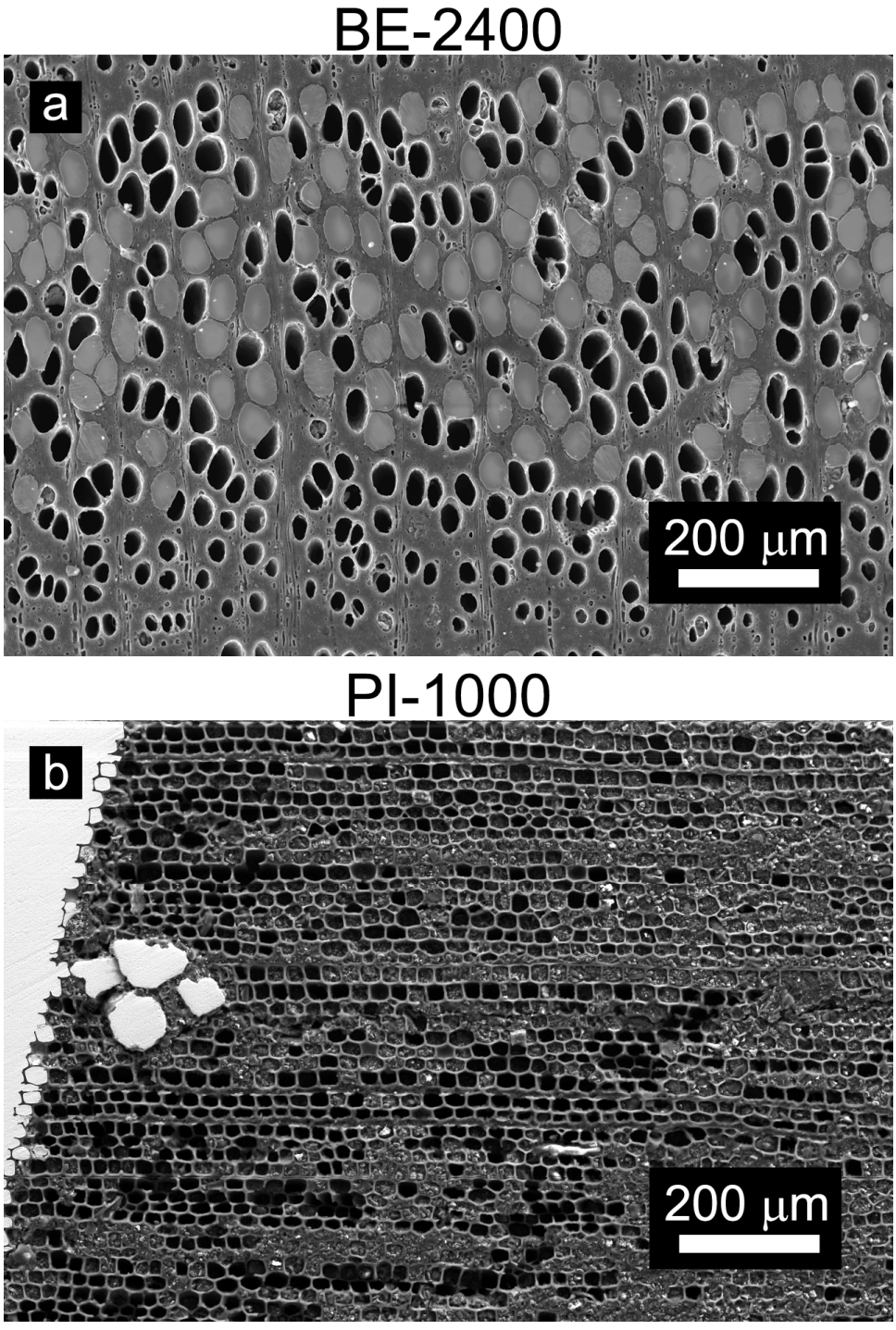

Figure 5.8. Representative SEM micrographs of the C18150-infiltrated beech- and pine-derived carbon. The pressure change, ≈ 0.07 MPa, was insufficient to infiltrate the smaller-diameter porosity in the beech and pine preforms.

large pores were infiltrated in the PI-C sample, while the larger-diameter early wood porosity was infiltrated in the BE-C. The presence of a reaction layer was visible only at higher magnifications. A thin, discontinuous, layer was visible (Figure 5.9) between the Cu and C in the infiltrated pores.

Samples that were slowly cooled to room temperature after infiltration exhibited the same characteristics seen with the Cu-Cr wetting experiments (Section 5.4). Representative transverse and longitudinal cross sections, shown in Figure 5.10, indicated an infiltration depth of ≈ 1 mm and a Cr_3C_2 layer thickness gradient similar to that seen in Figure 5.7. The thick carbide reaction layer, which led to the infiltration of the smaller diameter pores, was due to diffusion of excess Cr in the C18150 rod during the slow cool-down of the furnace.

While neither sample was fully-infiltrated, the distribution of pore diameters in the BE-C can be used along with Equations 2.7 and 2.12 to calculate the required infiltration pressure change as a function of pore diameter. The average diameter of the smallest infiltrated pores in the BE-C sample was ≈ 40 μm, and the applied ΔP was ≈ 0.07 MPa. Using these values, the work of immersion, W_i, can be calculated as 0.7 MPa·μm (0.7 N/m); therefore, the pressure in MPa required to infiltrate a cylindrical pore with diameter, d, in micrometers is 2.8 (MPa·μm)/d. Consequently, a pressure change in excess of 2.8 MPa would be needed to infiltrate the submicron diameter pores in the BE-C.

In general, the thickness of the carbide interface in the quenched samples was ≤ 1 μm, which corresponds to experiments and calculations by Devincent *et al.* (1993). While microscopy indicated a discontinuous layer of Cr_3C_2 particles, energy dispersive X-ray

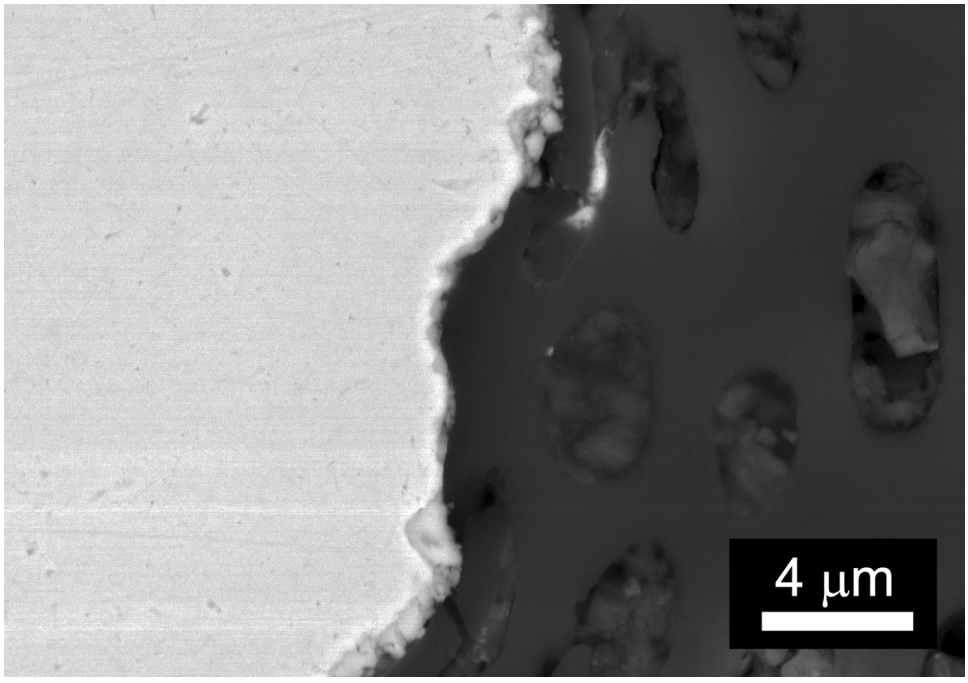

Figure 5.9. High-magnification SEM micrograph of the Cu/C interface in a BE-2400 preform pressure-infiltrated with C18150 and subsequently quenched. A thin and discontinuous Cr_3C_2 layer is visible at the interface.

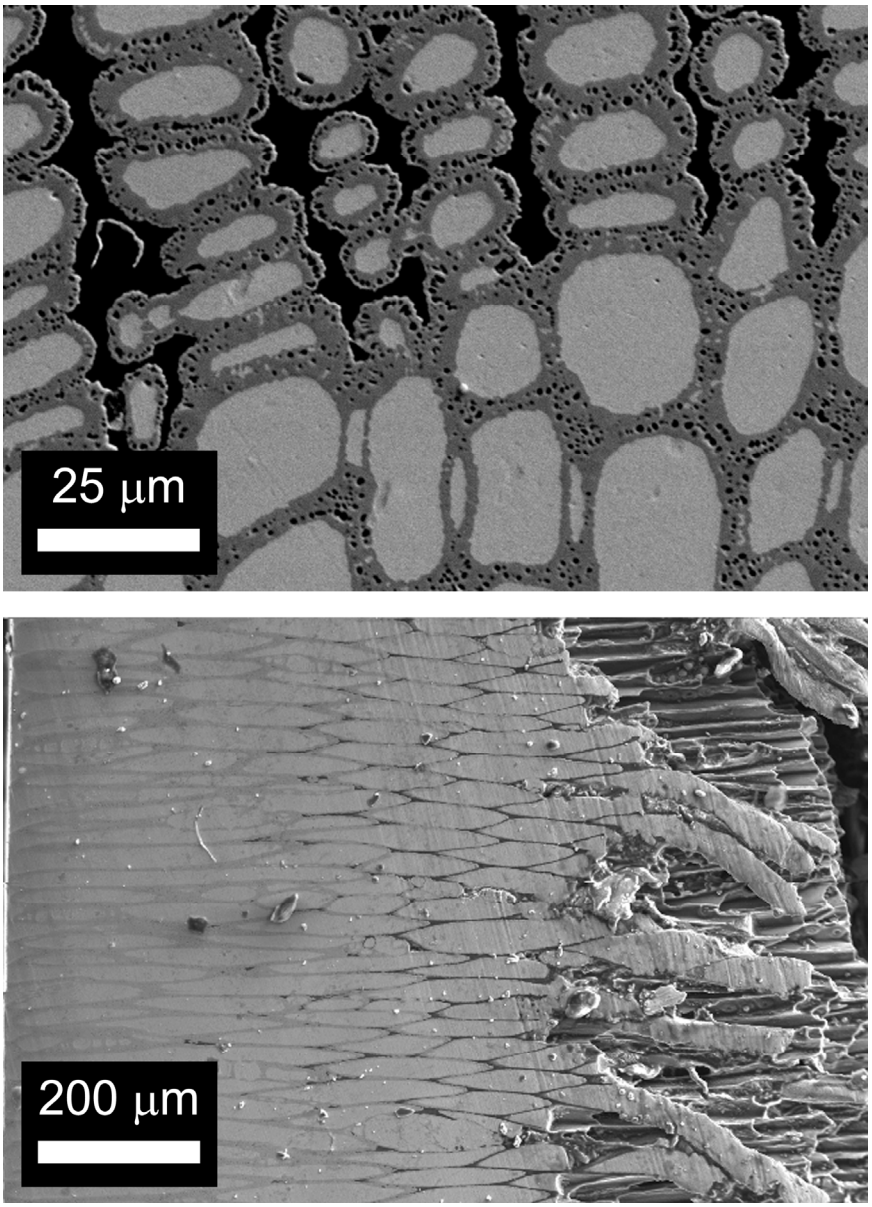

Figure 5.10. SEM micrographs of transverse (top) and longitudinal (bottom) sections of a pine-derived carbon sample pressure-infiltrated with C18150 and slowly-cooled to room temperature. Carbon (black) at the top of the preform (top) had almost completely reacted to form Cr_3C_2 (dark gray). The left edge of the bottom micrograph is the interface between the preform and the C18150 billet. The Cr_3C_2 layer thickness decreases with increasing depth into the preform.

spectroscopy revealed a continuous concentration of Cr along the Cu/C interface (Figure 5.11). Reaction times longer than 30 seconds could be used to create a continuous carbide layer.

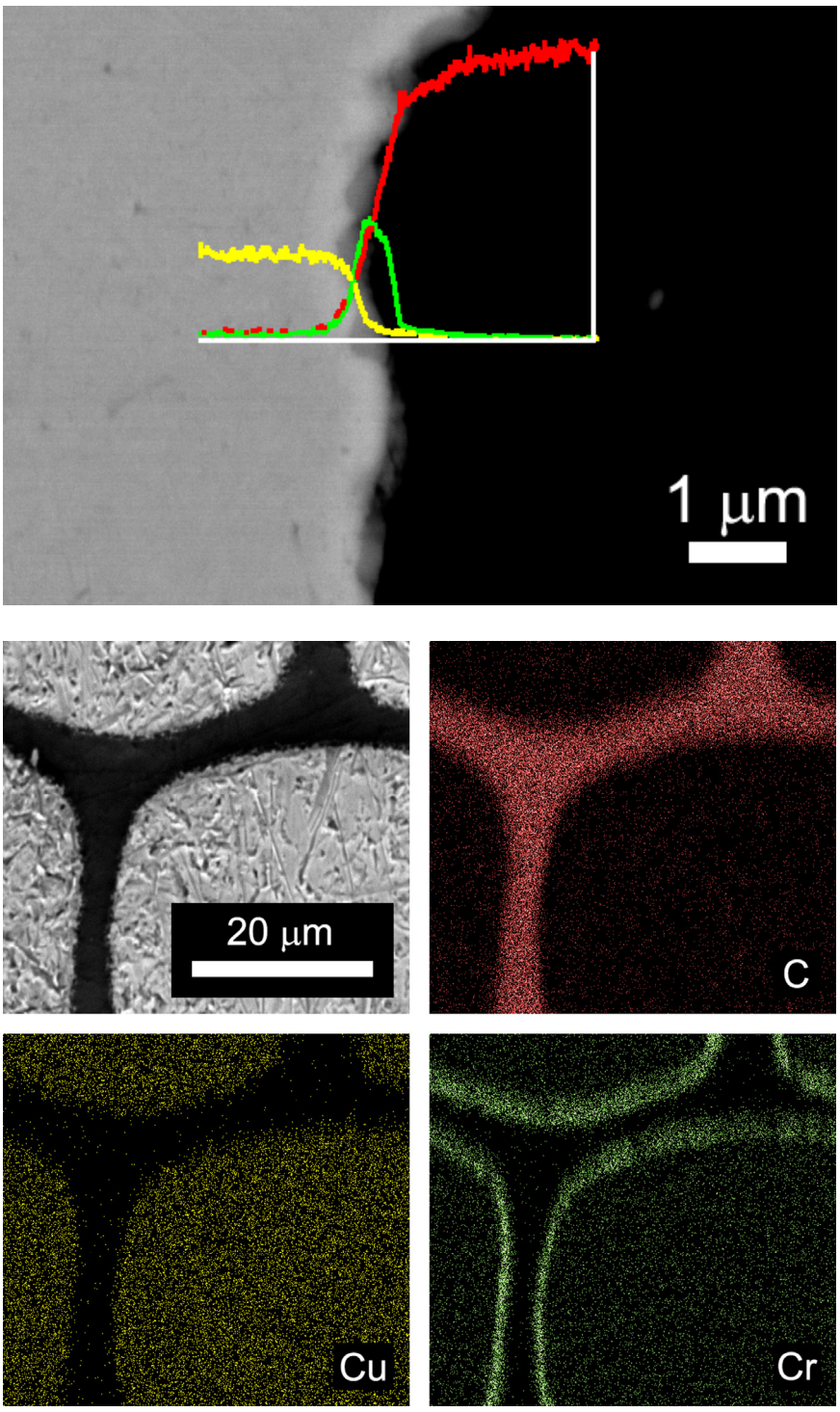

Figure 5.11. A line scan across the $Cu/Cr_3C_2/C$ interface shown in Figure 5.9 and an element map (PI-1000 pressure-infiltrated with C18150 and quenched); both measured with energy dispersive X-ray spectroscopy.

5.6. Summary

Two woods, pine and beech, were pyrolyzed at both 1000°C and 2400°C. The resulting carbon materials retained the microstructure of the starting wood. According to X-ray diffraction, the two pyrolysis temperatures resulted in carbon that was either amorphous or turbostratic. Compared to bulk copper, infiltration of OFHC copper into the carbon preforms resulted in materials with decreased specific density, but the composites contained 5-10% porosity and damaged carbon cell walls were observed. Theoretical predictions indicated anisotropic mechanical and thermal conductivity behavior, including a reduced CTE and large reduction in thermal conductivity. In general, the calculated specific modulus and specific thermal conductivity of the composites in the longitudinal direction were greater than those of OFHC Cu, but the specific transverse composite properties were less than those of OFHC Cu.

Congruent to results in the literature, copper alloys containing chromium resulted in the formation of Cr_3C_2 at the Cu/C interface. The reaction layer was relatively thick in the case of experiments that were slowly cooled to room temperature. The carbon preforms completely reacted into the carbide at the interface of the sample and the Cu-Cr billet, and the reaction layer thickness decreased with increasing depth into the sample. Quickly quenching the composite about 30 seconds after pressurized infiltration resulted in a thin and discontinuous carbide layer that, on average, was ≤ 1 μm in thickness. According to calculations based on perfectly straight and cylindrical porosity, the pressure (MPa) needed to infiltrate the C18150 alloy into the carbon preforms is equal to 2.8 (MPa·μm)/d, where d is the pore diameter in micrometers. Therefore, while making Cu/C composites

with the wood-derived carbon is feasible, the following factors should be addressed: the relatively weak Cu/C interface, the simultaneous need for infiltration temperatures and pressures of at least 1150°C and 3 MPa, respectively, and damage sustained by the carbon preforms during processing.

6. Summary & Conclusions

6.1. Summary

Natural materials have become increasingly inspiring in the design of advanced materials. Wood-derived ceramic materials have gained interest due to the range of possible microstructures and ceramic materials that can be made from the wide variety of wood species. The anisotropic porous materials retain the microstructure of the starting wood precursor and are being considered for a broad array of applications. The purpose of this work was to investigate the use of wood-derived ceramics in metal/ceramic composite materials.

The processing, microstructure, and properties of aluminum/silicon carbide (Al/SiC) composites were investigated. Beech and sapele wood were converted into porous SiC by pyrolyzing the wood, infiltrating molten silicon into the carbon and finally etching away the excess silicon. The SiC materials contained small amounts of closed porosity and residual carbon. A volume expansion occurring during the conversion of carbon to SiC eliminated most of the small-diameter porosity (≤ 1 μm) that was observed in the carbon. The composites were made by infiltrating molten aluminum into the SiC. Infiltration experiments with the A356 alloy resulted in only partial infiltration of the preforms. An aluminum alloy containing both silicon and magnesium was then used to avoid formation of aluminum carbide and improve wetting of the SiC preform. Pressurized infiltration of the Al-Si-Mg alloy was successful when the alloy was prepared in an inert environment. The metal in the composites contained both Si and Mg_2Si precipitates due to the large amounts of Si and Mg.

The composite microstructure consisted of interconnected SiC surrounding Al-alloy fibers. The mechanical properties of the MCCs were investigated by measuring the compressive strength, flexural properties, ultrasonic modulus, and load partitioning. The modulus, strength and toughness in the longitudinal direction were similar to those reported in metal-ceramic composites with equivalent volume fractions of both phases. The properties in the transverse direction were lower than those in the longitudinal direction, which reproduced the differences observed in the properties of the porous SiC. In general, the room temperature strength, stiffness and toughness were maintained up to 200°C and then decreased at higher temperatures. The longitudinal composite stiffness was less than that predicted by the Halpin-Tsai model due to the non-ideal microstructure. The increase in longitudinal toughness due to the Al followed the predictions of Ashby's model for toughening ceramics by incorporating constrained ductile inclusions.

The wood-derived carbon material was also used as a precursor to copper/carbon composites. Pine and beech were pyrolyzed at both 1000°C and 2400°C and resulted in carbon that was amorphous and turbostratic, respectively. Infiltration of OFHC copper into the carbon preforms resulted in materials with 5-10% porosity and damage of the carbon was observed. Theoretical predictions indicated anisotropic mechanical and thermal conductivity behavior. In general, the longitudinal specific modulus and thermal conductivity were greater than those of OFHC Cu, but the specific transverse properties were less than those of OFHC Cu.

Copper alloys containing chromium resulted in the formation of Cr_3C_2 at the Cu/C interface. The reaction layer was relatively thick in the case of specimens that were slowly

cooled to room temperature. Quickly quenching composites about 30 seconds after pressurized infiltration resulted in a thin and discontinuous carbide layer that, on average, was ≤ 1 μm in thickness. The pressure in megapascals needed to infiltrate the C18150 alloy into the carbon preforms was calculated, assuming perfectly straight and cylindrical pores, as 2.8 (MPa·μm)/d where d is the pore diameter in micrometers.

6.2. Conclusions

6.2.1. Aluminum/Silicon Carbide Composites

Melt-infiltration of an aluminum alloy into porous wood-derived SiC is an effective means to manufacture metal-ceramic composites. The resulting material consists of interconnected SiC with Al fibers oriented in the axial and radial directions of the precursor wood. X-ray microtomography is a valuable technique that can be used to non-destructively investigate the microstructure of materials. The ability to process a large volume of data and the high-resolution of the data revealed microstructural details such as the interconnectivity of the wood, the rough nature of the SiC preforms and the variability of the pore diameters. Deriving SiC from wood precursors uses relatively low processing temperatures, yields a unique near-net-shape microstructure and does not require the use of binders or sintering when used as a composite preform.

The modulus, strength and toughness in the longitudinal direction were similar to those reported in metal-ceramic composites with equivalent volume fractions of both phases. The corresponding properties in the transverse direction were lower than the longitudinal properties, and this behavior reproduced the differences observed in the properties of the

porous SiC. Overall, the room temperature strength and toughness were maintained up to 200°C and then decreased due to the marked reduction of the flow stress of the Al alloy above this temperature. The microstructure of the precursor wood had little influence on the stiffness and strength of the MCCs, as opposed to the behavior found in the porous SiC.

The analysis of the experimental results showed that the deformation of the composites in the longitudinal direction was controlled by the rigid SiC skeleton, leading to brittle behavior throughout the entire temperature range. The longitudinal composite stiffness was below that predicted by Halpin-Tsai due to the non-ideal microstructure: nonparallel and nonlinear Al-filled pores. Moreover, the increase in toughness due to the Al followed the predictions of Ashby's model for toughening ceramics by incorporating ductile inclusions. MCCs made from woods with larger diameter pores are tougher than those with the same volume fraction of smaller diameter metal inclusions.

In the transverse orientation, the Al alloy played a more important role, as is demonstrated by the extent of the non-linear deformation of the BE-TR2 MCC at 500°C. The stiffness of the TR1 and TR2 MCCs were closer to the Halpin-Tsai model for the transverse stiffness of a uniaxial composite indicating that the load transfer from the Al to the SiC in the transverse direction was less efficient, leading to a lower modulus, strength and toughness.

6.2.2. Copper/Carbon Composites

Manufacturing Cu/C composites with wood-derived carbon was feasible, but several concerns were raised in the present study. The greatest of these concerns was the

amorphous nature of the carbon, which essentially acted as porosity due to its low thermal conductivity and drastically reduced the thermal conductivity of the Cu/C composites. The large CTE difference between the OFHC copper and amorphous carbon resulted in damage to the carbon preforms during processing. This, and the poor Cu/C interface, could affect both the mechanical and thermal properties of the composites. A copper alloy containing chromium was found to improve the interface due to the formation of chromium carbide. Quenching composites after pressurized infiltration stopped the reaction between Cr and C and resulted in a thin and discontinuous carbide interface rather than the thick layer observed in experiments where reaction times were significantly longer.

6.3. Suggestions for Future Work

Based on the completed work, there are several areas where additional work could improve the composite materials themselves or the understanding of the processing-microstructure-property relationships. The suggestions for future work are divided into sections for each material studied.

6.3.1. Aluminum/Silicon Carbide Composites

A disadvantage of the composites studied was the brittle nature of the aluminum alloy at room temperature. The ductility of the alloy could be improved by reducing the Si and Mg content, but this would impair the ability to process the composites. Therefore, other methods to improve the Al/SiC wettability should be investigated, including the use of higher infiltration pressures. Improvements in the composites could also be made by

decreasing the amount of residual carbon and porosity in the preforms. Higher processing temperatures and longer silicon-infiltration times would likely lead to full reaction of the carbon into SiC, but closed porosity would most likely still be present.

Investigating other SiC processing methods, such as gas-phase infiltration and sol-gel synthesis, could result in materials free of carbon and closed porosity. The effect of the carbon and closed porosity on mechanical properties may be minimal, but it would also be interesting to see the effect of the different SiC pore wall structures on the properties of the composite materials. The pore-wall structure may affect the Al/SiC mechanical bond, which would affect the stiffness and toughness of the composites due to changes in load transfer behavior and the constraint of the Al in the pores. In addition to mechanical properties, studying the thermal properties of the composites would also be valuable as Al/SiC composites are also used in thermal management applications (Zweben 1992).

More extensive high-energy X-ray studies would also be beneficial. More load partitioning experiments, including studies of samples in different orientations, different wood precursors and multiple loading/unloading cycles would lead to a deeper understanding of the composite mechanical behavior. Also, images could be captured during *in-situ* loading to connect the numerical data to observed fracture phenomena. Microtomography of composites based on different precursor woods may reveal more details about microstructural changes occurring during processing. Also, the three-dimensional data from μCT experiments could be used with OOF3, a version of the object-oriented finite element software, OOF, currently being developed by NIST (Langer *et al.* 2001).

6.3.2. Copper/Carbon Composites

As for the Cu/C composites, a study dedicated to the graphitization of the amorphous carbon would be particularly useful. As wood is a non-graphitizable carbon (Cheng *et al.* 1999), a catalyst may be required to initiate graphitization (Oya *et al.* 1979). Copper has been shown to catalyze the graphitization of non-graphitizable carbons (Yokokawa *et al.* 1966, 1967). In terms of Cu/C composites, using Cu as a catalyst would be ideal as any residual catalyst could be incorporated into the composite. Also, the graphitization temperature used by Yokokawa *et al.*, only 1500°C, is easily achieved with a conventional high-temperature furnace. A brief experiment to test the catalytic effect of CuO on wood-based carbon was performed with two grams of pine that had been pyrolyzed at 1000°C and crushed with a mortar and pestle to pass through a 250 μm mesh. The pine was crushed to eliminate the difficulty of graphitizing the 3-D porous macrostructure and adhere as closely as possible to the Yokokawa *et al.* experiment. The carbon powder was mixed with 5 wt.% CuO, heated at a rate of 5°C/minute to 1550°C for one hour in an ultra-high purity nitrogen atmosphere. X-ray diffraction of the carbon indicated a crystalline peak in only the catalyzed carbon pattern, but the peak (at 43° 2θ) corresponded to the Cu (111) reflection, which indicated the presence of residual catalyst.

In the above experiment, there were three deviations from the experimental procedures of Yokokawa *et al.* that could have contributed to the lack of graphitization of the pine-derived carbon. First, the initial heat treatment temperatures (HTT) of the carbons were different (800°C versus 1000°C). The slightly higher HTT of the PI-C could have created a more cross-linked and randomly-oriented structure, which would make

graphitization less likely (Franklin 1951b). Second, the initial heat treatment atmosphere was different (nitrogen versus argon), which can affect the carbon structure (Noda *et al.* 1964). Finally, Yokokawa *et al.* did not specify the catalyst particle size, which has been shown to affect the degree of graphitization (Oya *et al.* 1976).

In the future, the effect of the initial heat treatment temperature should be studied by pyrolyzing the wood at various temperatures. The effect of the pyrolysis atmosphere should also be investigated. In particular, it has been suggested by Franklin that a reducing atmosphere may lead to a less cross-linked carbon structure, which would be easier to graphitize (Franklin 1951a). Also, different catalysts should be investigated: a recent study by Sevilla *et al.* indicates that nickel and iron may be effective catalysts for wood materials (Sevilla *et al.* 2007).

Once a suitable catalyst is ultimately found, the problem of graphitizing the 3-D wood structure must be addressed. The goal should be to achieve a homogeneous distribution of the catalyst throughout the structure, and two processes have shown promise in this respect. Sol-gel processing results in an even coating and can be applied to either the wood or pyrolyzed carbon, and, therefore, could be used independent of the optimum initial heat treatment temperature. Electroplating should also be investigated, and has already been shown to be an effective way to coat both the wood-derived carbon and SiC (Pappacena *et al.* 2008).

Finally, the thermal properties, including the CTE and conductivity of the composites should be measured as a function of both orientation and temperature. The effects of a

Cr_3C_2 interface, and its thickness, along with the effects of using different wood precursors should also be investigated.

References

Ashby, M. F., Blunt, F. J. and Bannister, M. (1989). "Flow characteristics of highly constrained metal wires." *Acta Metallurgica* **37**(7): 1847-1857.

ASTM (1988). ASTM C373-88: Standard test method for water absorption, bulk density, apparent porosity, and apparent specific gravity of fired whiteware products. West Conshohocken, PA, ASTM International.

ASTM (2002). ASTM C1421-01b: Standard test method for determination of fracture toughness of advanced ceramics at ambient temperature. West Conshohocken, PA, ASTM International.

ASTM (2003). ASTM C1161-02c: Standard test method for flexural strength of advanced ceramics at ambient temperature. West Conshohocken, PA, ASTM International.

ASTM (2004). ASTM E8: Standard test methods for tension testing of metallic materials. West Conshohocken, PA, ASTM International.

Balch, D. K. and Dunand, D. C. (2006). "Load partitioning in aluminum syntactic foams containing ceramic microspheres." *Acta Materialia* **54**(6): 1501-1511.

Bannister, M., Shercliff, H., Bao, G., Zok, F. and Ashby, M. F. (1992). "Toughening in brittle systems by ductile bridging ligaments." *Acta Metallurgica et Materialia* **40**(7): 1531-1537.

Barthel, K. U. (2006). Volume Viewer plugin for ImageJ, http://rsb.info.nih.gov/ij/plugins/volume-viewer.html.

Beckwith, S. and Greenwood, M. (2006). "Don't overlook composite FRP pipe." *Chemical Engineering* **113**(5): 42-48.

Blucher, J. T. (1992). "Discussion of a liquid-metal pressure infiltration process to produce metal matrix composites." *Journal of Materials Processing Technology* **30**(3): 381-390.

Bond, G. M., Richman, R. H. and McNaughton, W. P. (1995). "Mimicry of natural material designs and processes." *Journal of Materials Engineering and Performance* **4**(3): 334-345.

Byrne, C. E. and Nagle, D. C. (1997a). "Carbonization of wood for advanced materials applications." *Carbon* **35**(2): 259-266.

Byrne, C. E. and Nagle, D. C. (1997b). "Carbonized wood monoliths - characterization." *Carbon* **35**(2): 267-273.

Cao, J., Rambo, C. R. and Sieber, H. (2004a). "Preparation of porous Al_2O_3 ceramics by biotemplating of wood." *Journal of Porous Materials* **11**(3): 163-172.

Cao, J., Rusina, O. and Sieber, H. (2004b). "Processing of porous TiO_2 ceramics from biological preforms." *Ceramics International* **30**(7): 1971-1974.

Chawla, K. K. (1998). Composite Materials: Science and Engineering. New York, Springer.

Cheng, H. M., Endo, H., Okabe, T., Saito, K. and Zheng, G. B. (1999). "Graphitization behavior of wood ceramics and bamboo ceramics as determined by X-ray diffraction." *Journal of Porous Materials* **6**(3): 233-237.

Chu, Y. S., Liu, C., Mancini, D. C., De Carlo, F., Macrander, A. T., Lai, B. and Shu, D. (2002). "Performance of a double-multilayer monochromator at beamline 2-BM at the Advanced Photon Source." *Review of Scientific Instruments* **73**(3): 1485-1487.

Chung, D. D. L. and Zweben, C. (2000). Composites for Electronic Packaging and Thermal Management. Comprehensive Composite Materials. Kelly, A. and Zweben, C. Oxford, Pergamon**:** 701.

Clarke, D. R. (1992). "Interpenetrating phase composites." *Journal of the American Ceramic Society* **75**(4): 739-759.

Clausen, B. (1997). Characterisation of Polycrystal Deformation by Numerical Modelling and Neutron Diffraction Measurements. Roskilde, Denmark, Riso National Laboratory. **Ph.D. Thesis**.

Clyne, T. W. and Withers, P. J. (1993). An Introduction to Metal Matrix Composites. Cambridge, Cambridge University Press.

Colombo, P. (2006). "Conventional and novel processing methods for cellular ceramics." *Philosophical Transactions of the Royal Society A - Mathematical Physical and Engineering Sciences* **364**(1838): 109-124.

Conners, T. E. (2001). Wood: Ultrastructure. Encyclopedia of Materials: Science and Technology. Jürgen Buschow, K. H., Cahn, R. W., Flemings, M. C., Ilschner, B., Kramer, E. J. and Mahajan, S. New York, Elsevier**:** 9751-9759.

Cornie, J. A., Ryals, M. A. and Cornie, S. S. (2003). Discontinuous carbon fiber reinforced metal matrix composite, Metal Matrix Cast Composites, Inc.**:** U.S. Patent 2003/0164206.

Creber, D. K., Poste, S. D., Aghajanian, M. K. and Claar, T. D. (1988). "AlN composite growth by nitridation of aluminum alloys." *Ceramic Engineering and Science Proceedings* **9**(7-8): 975-982.

Cullity, B. D. and Stock, S. R. (2001). Elements of X-ray Diffraction. Upper Saddle River, N.J., Prentice Hall.

Daniel, I. M. and Ishai, O. (1994). Engineering Mechanics of Composite Materials. New York, Oxford University Press.

Davis, J. R. (2001). Copper and Copper Alloys. Materials Park, OH, ASM International.

de Arellano-López, A. R., Martinez-Fernandez, J., Gonzalez, P., Dominguez, C., Fernandez-Quero, V. and Singh, M. (2004). "Biomorphic SiC: A new engineering ceramic material." *International Journal of Applied Ceramic Technology* **1**(1): 56-67.

DeFouw, J. D. (2007). Processing of Superconducting Metal/Magnesium Diboride Composites, Northwestern University. **Ph.D. Thesis**.

Devincent, S. M. and Michal, G. M. (1993). "Reaction layer formation at the graphite copper-chromium alloy interface." *Metallurgical Transactions A - Physical Metallurgy and Materials Science* **24**(1): 53-60.

Dinwoodie, J. M. (1989). Wood: Nature's Cellular, Polymeric, Fibre-Composite. London ; Brookfield, VT, USA, Institute of Metals.

Eliasson, J. and Sandström, R. (1995). "Applications of aluminium matrix composites." *Key Engineering Materials* **104-107**: 3-36.

Faber, K. T. and Evans, A. G. (1983). "Intergranular crack-deflection toughening in silicon-carbide." *Journal of the American Ceramic Society* **66**(6): C94-C96.

Fan, T. X., Li, X. F., Liu, Z. T., Gu, J. J., Zhang, D. and Guo, Q. X. (2006). "Microstructure and infrared absorption of biomorphic chromium oxides templated by wood tissues." *Journal of the American Ceramic Society* **89**(11): 3511-3515.

Franklin, R. (1951a). "The structure of graphitic carbons." *Acta Crystallographica* **4**(3): 253-261.

Franklin, R. E. (1951b). "Crystallite growth in graphitizing and non-graphitizing carbons." *Proceedings of the Royal Society of London A - Mathematical and Physical Sciences* **209**(1097): 196.

Garcia-Cordovilla, C., Louis, E. and Narciso, J. (1999). "Pressure infiltration of packed ceramic particulates by liquid metals." *Acta Materialia* **47**(18): 4461-4479.

Ghanem, H., Kormann, M., Gerhard, H. and Popovska, N. (2007). "Processing of biomorphic porous TiO_2 ceramics by chemical vapor infiltration and reaction (CVI-R) technique." *Journal of the European Ceramic Society* **27**(12): 3433-3438.

Gibson, L. J. and Ashby, M. F. (1997). Cellular Solids: Structure and Properties. Cambridge, Cambridge University Press.

Greil, P. (2001). "Biomorphous ceramics from lignocellulosics." *Journal of the European Ceramic Society* **21**(2): 105-118.

Greil, P., Lifka, T. and Kaindl, A. (1998a). "Biomorphic cellular silicon carbide ceramics from wood I: processing and microstructure." *Journal of the European Ceramic Society* **18**(14): 1961-1973.

Greil, P., Lifka, T. and Kaindl, A. (1998b). "Biomorphic cellular silicon carbide ceramics from wood II: mechanical properties." *Journal of the European Ceramic Society* **18**(14): 1975-1983.

Greil, P., Vogli, E., Fey, T., Bezold, A., Popovska, N., Gerhard, H. and Sieber, H. (2002). "Effect of microstructure on the fracture behavior of biomorphous silicon carbide ceramics." *Journal of the European Ceramic Society* **22**(14-15): 2697-2707.

Greiner, C., Oppenheimer, S. M. and Dunand, D. C. (2005). "High strength, low stiffness, porous NiTi with superelastic properties." *Acta Biomaterialia* **1**(6): 705-716.

Guinea, G. V., Pastor, J. Y., Planas, J. and Elices, M. (1998). "Stress intensity factor, compliance and CMOD for a general three-point-bend beam." *International Journal of Fracture* **89**(2): 103-116.

Hahn, G. T. and Rosenfield, A. R. (1975). "Metallurgical factors affecting fracture toughness of aluminum-alloys." *Metallurgical Transactions A - Physical Metallurgy and Materials Science* **6**(4): 653-668.

Halpin, J. C., Finlayson, K. M. and Ashton, J. E. (1992). Primer on Composite Materials Analysis. Lancaster, Pa., Technomic Pub. Co.

Halpin, J. C. and Kardos, J. L. (1976). "Halpin-Tsai equations - review." *Polymer Engineering and Science* **16**(5): 344-352.

Han, D. S., Jones, H. and Atkinson, H. V. (1993). "The wettability of silicon-carbide by liquid aluminum - the effect of free silicon in the carbide and of magnesium, silicon and copper alloy additions to the aluminum." *Journal of Materials Science* **28**(10): 2654-2658.

Hauk, V. and Behnken, H. (1997). Structural and Residual Stress Analysis by Nondestructive Methods: Evaluation, Application, Assessment. Amsterdam ; New York, Elsevier.

He, B. B. and Smith, K. L. (1998). Fundamental equation of strain and stress measurement using 2D detectors. SEM Spring Conference on Experimental and Applied Mechanics, Houston, TX.

Hellwege, K. H., Ed. (1979). Elastic, Piezoelectric and Related Constants of Crystals. Berlin-Heidelberg, Germany, Springer-Verlag.

Herzog, A., Vogt, U., Kaczmarek, O., Klingner, R., Richter, K. and Thoemen, H. (2006a). "Porous SiC ceramics derived from tailored wood-based fiberboards." *Journal of the American Ceramic Society* **89**(5): 1499-1503.

Herzog, A., Vogt, U. F., Siegmann, S. and Beffort, O. (2006b). "Aluminium metal matrix composites based on biomorphic silicon carbide." *Advanced Engineering Materials* **8**(10): 980-983.

Heuer, A. H., Fink, D. J., Laraia, V. J., Arias, J. L., Calvert, P. D., Kendall, K., Messing, G. L., Blackwell, J., Rieke, P. C., Thompson, D. H., Wheeler, A. P., Veis, A. and Caplan, A. I. (1992). "Innovative materials processing strategies - a biomimetic approach." *Science* **255**(5048): 1098-1105.

Hillig, W. B. (1994). "Making ceramic composites by melt infiltration." *American Ceramic Society Bulletin* **73**(4): 56-62.

Holliday, L. (1963). "Complex and heterophase materials." *Chemistry & Industry* (20): 794-798.

Holliday, L. (1966). Composite Materials. Amsterdam, New York,, Elsevier Pub. Co.

Hou, G. Y., Jin, Z. H. and Qian, J. M. (2006). "Effect of starting Si contents on the properties and structure of biomorphic SiC ceramics." *Journal of Materials Processing Technology* **182**(1-3): 34-38.

Hou, G. Y., Jin, Z. H. and Qian, J. M. (2007). "Effect of holding time on the basic properties of biomorphic SiC ceramic derived from beech wood." *Materials Science and Engineering A - Structural Materials: Properties, Microstructure and Processing* **452**: 278-283.

Hubbel, J. H. and Seltzer, S. M. (2008). "Tables of X-ray Mass Attenuation Coefficients and Mass Energy-Absorption Coefficients." from http://physics.nist.gov/PhysRefData/XrayMassCoef/cover.html.

Hull, D. and Clyne, T. W. (1981). An Introduction to Composite Materials. Cambridge, Cambridge University Press.

Hunt, M. and Baxter, D., ed. (2005). Composite fuselage section completed for Boeing 7E7. Advanced Materials & Processes. **163:** 66-66.

Jun, I. K., Kong, Y. M., Lee, S. H., Kim, H. E., Kim, H. W. and Goretta, K. C. (2006). "Reinforcement of a reticulated porous ceramic by a novel infiltration technique." *Journal of the American Ceramic Society* **89**(7): 2317-2319.

Kaul, V. S. (2007). Structure-Mechanical Property Relationships in Porous SiC Derived from Wood, Northwestern University. **Ph.D. Thesis**.

Kaul, V. S. and Faber, K. T. (2005). "Synthetic crossed-lamellar microstructures in oxide ceramics." *Journal of Ceramic Processing Research* **6**(3): 218-222.

Kaul, V. S. and Faber, K. T. (2008). "Nanoindentation analysis of the elastic properties of porous SiC derived from wood." *Scripta Materialia* **58**(10): 886.

Kaul, V. S., Faber, K. T., Sepulveda, R., de Arellano-López, A. R. and Martinez-Fernandez, J. (2006). "Precursor selection and its role in the mechanical properties of porous SiC derived from wood." *Materials Science and Engineering A - Structural Materials: Properties, Microstructure and Processing* **428**(1-2): 225-232.

Kutz, M. (2003). Standard Handbook of Biomedical Engineering and Design. New York, McGraw-Hill.

Langer, S. A., Fuller, E. and Carter, W. C. (2001). "OOF: An image-based finite-element analysis of material microstructures." *Computing in Science & Engineering* **3**(3): 15-23.

Lawn, B. R. (1993). Fracture of Brittle Solids. Cambridge, Cambridge University Press.

Ledbetter, H. M. and Read, D. T. (1977). "Orthorhombic elastic-constants of an NbTi-Cu composite superconductor." *Journal of Applied Physics* **48**(5): 1874-1879.

Li, X. F., Fan, T. X., Liu, Z. T., Ding, J., Guo, Q. X. and Zhang, D. (2006). "Synthesis and hierarchical pore structure of biomorphic manganese oxide derived from woods." *Journal of the European Ceramic Society* **26**(16): 3657-3664.

Liu, H., Shinoda, T., Mishima, Y. and Suzuki, T. (1989). "Effects of alloying on the wettability of copper to carbon-fibers." *ISIJ International* **29**(7): 568-575.

Lu, W. J., Zhang, D., Zhang, X. N., Wu, R. J., Sakata, T. and Mori, H. (2001). "Creep rupture life of *in situ* synthesized (TiB plus TiC)/Ti matrix composites." *Scripta Materialia* **44**(10): 2449-2455.

Mabee, W. E. and Roy, D. N. (2001). Wood: Chemicals. Encyclopedia of Materials: Science and Technology. Jürgen Buschow, K. H., Cahn, R. W., Flemings, M. C., Ilschner, B., Kramer, E. J. and Mahajan, S. New York, Elsevier**:** 9606-9609.

Martinez-Fernandez, J., Valera-Feria, F. M. and Singh, M. (2000). "High temperature compressive mechanical behavior of biomorphic silicon carbide ceramics." *Scripta Materialia* **43**(9): 813-818.

Mayerhofer, K. E., Neubauer, E., Eisenmenger-Sittner, C. and Hutter, H. (2002). "Adhesion promotion of Cu on C by Cr intermediate layers investigated by the SIMS method." *Analytical and Bioanalytical Chemistry* **374**(4): 602-607.

McCartney, D. G. and Hunt, J. D. (1981). "Measurements of cell and primary dendrite arm spacings in directionally solidified aluminum-alloys." *Acta Metallurgica* **29**(11): 1851-1863.

McDonald, A. G. (2001). Constituents of Wood. Encyclopedia of Materials: Science and Technology. Jürgen Buschow, K. H., Cahn, R. W., Flemings, M. C., Ilschner, B., Kramer, E. J. and Mahajan, S. New York, Elsevier**:** 9612-9616.

McGonnagle, W. J. (1968). Nondestructive Testing. Philadelphia, Gordon and Breach Science Publishers.

Meyers, M. A. and Chawla, K. K. (1984). Mechanical Metallurgy : Principles and Applications. Englewood Cliffs, N.J., Prentice-Hall.

Mortensen, A. (2000). Melt Infiltration of Metal Matrix Composites. Comprehensive Composite Materials. Kelly, A. and Zweben, C. Oxford, Pergamon**:** 521.

Mortensen, A. and Jin, I. (1992). "Solidification processing of metal matrix composites." *International Materials Reviews* **37**(3): 101-128.

Mortensen, A., Michaud, V. J. and Flemings, M. C. (1993). "Pressure-infiltration processing of reinforced aluminum." *JOM-Journal of the Minerals Metals & Materials Society* **45**(1): 36-43.

Mortensen, A. and Wong, T. (1990). "Infiltration of fibrous preforms by a pure metal 3: capillary phenomena." *Metallurgical Transactions A - Physical Metallurgy And Materials Science* **21**(8): 2257-2263.

Mortimer, D. A. and Nicholas, M. (1970). "Wetting of carbon by copper and copper alloys." *Journal of Materials Science* **5**(2): 149-&.

Musgrave, M. J. P. (1970). Crystal Acoustics: Introduction to the Study of Elastic Waves and Vibrations in Crystals. San Francisco,, Holden-Day.

Newkirk, M. S., Urquhart, A. W., Zwicker, H. R. and Breval, E. (1986). "Formation of Lanxide ceramic composite materials." *Journal of Materials Research* **1**(1): 81-89.

Newnham, R. E., Skinner, D. P. and Cross, L. E. (1978). "Connectivity and piezoelectric-pyroelectric composites." *Materials Research Bulletin* **13**(5): 525-536.

Noda, T. and Inagaki, M. (1964). "Effect of gas phase on graphitization of carbon." *Carbon* **2**(2): 127-130.

Noyan, I. C. and Cohen, J. B. (1987). Residual Stress : Measurement by Diffraction and Interpretation. New York, Springer-Verlag.

Ohzawa, Y., Hoshino, H., Fujikawa, M., Nakane, K. and Sugiyama, K. (1998). "Preparation of high-temperature filter by pressure-pulsed chemical vapour infiltration of SiC into carbonized paper-fibre preforms." *Journal of Materials Science* **33**(21): 5259-5264.

Ota, T., Imaeda, M., Takase, H., Kobayashi, M., Kinoshita, N., Hirashita, T., Miyazaki, H. and Hikichi, Y. (2000). "Porous titania ceramic prepared by mimicking silicified wood." *Journal Of The American Ceramic Society* **83**(6): 1521-1523.

Ota, T., Takahashi, M., Hibi, T., Ozawa, M., Suzuki, S., Hikichi, Y. and Suzuki, H. (1995). "Biomimetic process for producing SiC "wood"." *Journal of the American Ceramic Society* **78**(12): 3409-3411.

Oya, A. and Marsh, H. (1982). "Phenomena of catalytic graphitization." *Journal of Materials Science* **17**(2): 309-322.

Oya, A. and Otani, S. (1976). "The effects of aluminum on structural development of a carbon derived from phenolic resin." *Carbon* **14**(4): 191.

Oya, A. and Otani, S. (1979). "Catalytic graphitization of carbons by various metals." *Carbon* **17**(2): 131-137.

Pappacena, K. E. and Faber, K. T. (2006). Unpublished research, Northwestern University.

Pappacena, K. E., Faber, K. T., Wang, H. and Porter, W. D. (2007). "Thermal conductivity of porous silicon carbide derived from wood precursors." *Journal Of The American Ceramic Society* **90**(9): 2855-2862.

Pappacena, K. E., Johnson, M. T. and Faber, K. T. (2008). Unpublished research, Northwestern University.

Pech-Canul, M. I., Katz, R. N. and Makhlouf, M. M. (2000a). "Optimum parameters for wetting silicon carbide by aluminum alloys." *Metallurgical and Materials Transactions A-Physical Metallurgy and Materials Science* **31**(2): 565-573.

Pech-Canul, M. I. and Makhlouf, M. M. (2000b). "Processing of Al-SiC_p metal matrix composites by pressureless infiltration of SiC_p preforms." *Journal of Materials Synthesis and Processing* **8**(1): 35-53.

Popovska, N., Streitwieser, D. A., Xu, C. and Gerhard, H. (2005). "Paper derived biomorphic porous titanium carbide and titanium oxide ceramics produced by chemical vapor

infiltration and reaction (CVI-R)." *Journal of the European Ceramic Society* **25**(6): 829-836.

Presas, M., Pastor, J. Y., Llorca, J., de Arellano-Lopez, A. R., Martinez-Fernandez, J. and Sepulveda, R. E. (2005). "Mechanical behavior of biomorphic Si/SiC porous composites." *Scripta Materialia* **53**(10): 1175-1180.

Price, A. T. (1928). "A Mathematical Discussion on the Structure of Wood in Relation to Its Elastic Properties." *Philisophical Transactions* **228**: 1-62.

Qiao, G. J., Ma, R., Cai, N., Zhang, C. G. and Jin, Z. H. (2002). "Mechanical properties and microstructure of Si/SiC materials derived from native wood." *Materials Science and Engineering A - Structural Materials: Properties, Microstructure and Processing* **323**(1-2): 301-305.

Rajan, T. P. D., Pillai, R. M. and Pai, B. C. (1998). "Reinforcement coatings and interfaces in aluminium metal matrix composites." *Journal of Materials Science* **33**(14): 3491-3503.

Rambo, C. R., Cao, J., Rusina, O. and Sieber, H. (2005). "Manufacturing of biomorphic (Si, Ti, Zr)-carbide ceramics by sol-gel processing." *Carbon* **43**(6): 1174-1183.

Rambo, C. R., Cao, J. and Sieber, H. (2004). "Preparation and properties of highly porous, biomorphic YSZ ceramics." *Materials Chemistry and Physics* **87**(2-3): 345-352.

Ramqvist, L. (1965). "Wetting of metallic carbides by liquid copper, nickel, cobalt and iron." *International Journal of Powder Metallurgy* **1**(4): 2-21.

Rasband, W. S. (2007). ImageJ, U. S. National Institutes of Health, Bethesda, Maryland, USA, http://rsb.info.nih.gov/ij/.

Rodriguez, F. (1996). Principles of Polymer Systems. Washington, DC, Taylor & Francis.

San Marchi, C., Kouzeli, M., Rao, R., Lewis, J. A. and Dunand, D. C. (2003). "Alumina-aluminum interpenetrating-phase composites with three-dimensional periodic architecture." *Scripta Materialia* **49**(9): 861-866.

Scala, E. P. (1996). "A brief history of composites in the US - The dream and the success." *JOM-Journal of the Minerals Metals & Materials Society* **48**(2): 45-48.

Scheidegger, A. E. (1974). The Physics of Flow Through Porous Media. Toronto, University of Toronto Press.

Schiroky, G. H., Miller, D. V., Aghajanian, M. K. and Fareed, A. S. (1997). "Fabrication of CMCs and MMCs using novel processes." *CMMC 1996 - Proceedings of the First International Conference on Ceramic and Metal Matrix Composites* **127-131**: 141-152.

Schoch, W., Heller, I., Schweingruber, F. H. and Kienast, F. (2004). "Wood anatomy of central European species." www.woodanatony.ch.

Schwartz, M. M. (1997). Composite Materials. Upper Saddle River, N.J., Prentice Hall PTR.

Sevilla, M., Sanchis, C., Valdes-Solis, T., Morallon, E. and Fuertes, A. B. (2007). "Synthesis of graphitic carbon nanostructures from sawdust and their application as electrocatalyst supports." *Journal of Physical Chemistry C* **111**(27): 9749-9756.

Shin, Y. S., Liu, J., Chang, J. H., Nie, Z. M. and Exarhos, G. (2001). "Hierarchically ordered ceramics through surfactant-templated sol-gel mineralization of biological cellular structures." *Advanced Materials* **13**(10): 728-732.

Sieber, H. (2005). "Biomimetic synthesis of ceramics and ceramic composites." *Materials Science and Engineering A - Structural Materials: Properties, Microstructure and Processing* **412**(1-2): 43-47.

Sieber, H., Vogli, E., Mullier, F., Greil, P., Popovska, N. and Gerhard, H. (2002). CVI-R gas phase processing of porous, biomorphic SiC-ceramics. Euro Ceramics VII, Pts. 1-3. **206-2:** 2013-2016.

Sigl, L. S., Mataga, P. A., Dalgleish, B. J., McMeeking, R. M. and Evans, A. G. (1988). "On the toughness of brittle materials reinforced with a ductile phase." *Acta Metallurgica* **36**(4): 945-953.

Silvain, J. F., Coupard, D., Le Petitcorps, Y., Lahaye, M., Onillon, M. and Goni, X. (2000). "Interface characterisation and wettability properties of carbon particle reinforced copper alloy." *Journal of Materials Chemistry* **10**(9): 2213-2218.

Singh, M. and Salem, J. A. (2002). "Mechanical properties and microstructure of biomorphic silicon carbide ceramics fabricated from wood precursors." *Journal of the European Ceramic Society* **22**(14-15): 2709-2717.

Skibo, M. D. and Schuster, D. M. (1988). Process for production of metal matrix composites by casting and composite therefrom. Patent, U. S., Dural Aluminum Composites Corp.**:** U.S. Patent: 4,759,995.

Stock, S. R. (1999). "X-ray microtomography of materials." *International Materials Reviews* **44**(4): 141-164.

Stock, S. R., Ignatiev, K. I., Dahl, T., Veis, A. and De Carlo, F. (2003). "Three-dimensional microarchitecture of the plates (primary, secondary, and carinar process) in the developing tooth of Lytechinus variegatus revealed by synchrotron X-ray absorption microtomography (microCT)." *Journal of Structural Biology* **144**(3): 282-300.

Stock, S. R., Vieira, A. E. M., Delbem, A. C. B., Cannon, M. L., Xiao, X. and Carlo, F. (2008). "Synchrotron microcomputed tomography of the mature bovine dentinoenamel junction." *Journal of Structural Biology* **161**(2): 162-171.

Streitwieser, D. A., Popovska, N., Gerhard, H. and Emig, G. (2005). "Application of the chemical vapor infiltration and reaction (M-R) technique for the preparation of highly porous biomorphic SiC ceramics derived from paper." *Journal of the European Ceramic Society* **25**(6): 817-828.

Studart, A. R., Gonzenbach, U. T., Tervoort, E. and Gauckler, L. J. (2006). "Processing routes to macroporous ceramics: a review." *Journal of the American Ceramic Society* **89**(6): 1771-1789.

Sun, B. H., Fan, T. X., Xu, J. Q. and Zhang, D. (2005). "Biomorphic synthesis of SnO_2 microtubules on cotton fibers." *Materials Letters* **59**(18): 2325-2328.

Sun, B. H., Fan, T. X., Zhang, D. and Okabe, T. (2004). "The synthesis and microstructure of morph-genetic TiC/C ceramics." *Carbon* **42**(1): 177-182.

Varela-Feria, F. M., Martinez-Fernandez, J., de Arellano-Lopez, A. R. and Singh, M. (2002). "Low density biomorphic silicon carbide: microstructure and mechanical properties." *Journal of the European Ceramic Society* **22**(14-15): 2719-2725.

Varela-Feria, F. M., Ramirez-Rico, J., de Arellano-López, A. R., Martinez-Fernandez, J. and Singh, M. (2008). "Reaction-formation mechanisms and microstructure evolution of biomorphic SiC." *Journal of Materials Science* **43**(3): 933-941.

Wainwright, S. A. (1976). Mechanical Design in Organisms. New York, Wiley.

Wang, Q. G. and Davidson, C. J. (2001a). "Solidification and precipitation behaviour of Al-Si-Mg casting alloys." *Journal of Materials Science* **36**(3): 739-750.

Wang, Y. X., De Carlo, F., Mancini, D. C., McNulty, I., Tieman, B., Bresnahan, J., Foster, I., Insley, J., Lane, P., von Laszewski, G., Kesselman, C., Su, M. H. and Thiebaux, M. (2001b). "A high-throughput X-ray microtomography system at the Advanced Photon Source." *Review of Scientific Instruments* **72**(4): 2062-2068.

Wang, Y. X., Tan, S. H. and Jiang, D. L. (2004). "The effect of porous carbon preform and the infiltration process on the properties of reaction-formed SiC." *Carbon* **42**(8-9): 1833-1839.

Wanner, A. and Dunand, D. C. (2000). "Synchrotron X-ray study of bulk lattice strains in externally loaded Cu-Mo composites." *Metallurgical and Materials Transactions A - Physical Metallurgy and Materials Science* **31**(11): 2949-2962.

Washburn, E. W. (1921). "Note on a method of determining the distribution of pore sizes in a porous material." *Proceedings of the National Academy of Sciences of the United States of America* **7**(4): 115.

Wegner, L. D. and Gibson, L. J. (2000a). "The mechanical behaviour of interpenetrating phase composites I - modelling." *International Journal of Mechanical Sciences* **42**(5): 925-942.

Wegner, L. D. and Gibson, L. J. (2000b). "The mechanical behaviour of interpenetrating phase composites II - a case study of a three-dimensionally printed material." *International Journal of Mechanical Sciences* **42**(5): 943-964.

Wegner, L. D. and Gibson, L. J. (2001). "The mechanical behaviour of interpenetrating phase composites III - resin-impregnated porous stainless steel." *International Journal of Mechanical Sciences* **43**(4): 1061-1072.

Wheeler, E. (2001). Wood: Macroscopic Anatomy. Encyclopedia of Materials: Science and Technology. Jürgen Buschow, K. H., Cahn, R. W., Flemings, M. C., Ilschner, B., Kramer, E. J. and Mahajan, S. New York, Elsevier**:** 9653-9658.

White, A. E. S. and Blakeley, T. H. (1962). "The improvement of ceramics by incorporation of metals, exemplified by nickel-magnesia." *Chemistry & Industry* (40): 1740-1743.

White, D. R., Urquhart, A. W., Aghajanian, M. W. and Creber, D. K. (1989). Metal Matrix Composites, Lanxide Technology Company, LP**:** U.S. Patent 4,828,008.

Wilkes, T. E., Pastor, J. Y., Llorca, J. and Faber, K. T. (2008). "Mechanical properties of wood-derived silicon carbide aluminum-alloy composites as a function of temperature." *Journal of Materials Research* **23**(6): DOI: 10.1557/JMR.2008.0197.

Yokokawa, C., Hosokawa, K. and Takegami, Y. (1966). "Low temperature catalytic graphitization of hard carbon." *Carbon* **4**: 459-465.

Yokokawa, C., Hosokawa, K. and Takegami, Y. (1967). "A kinetic study of catalytic graphitization of hard carbon." *Carbon* **5**: 475-480.

Young, M. L. (2006). Strain Measurements and Imaging of Metal Matrix Composites Using High-Energy X-rays, Northwestern University. **Ph.D. Thesis**.

Young, M. L., Almer, J. D., Daymond, M. R., Haeffner, D. R. and Dunand, D. C. (2007a). "Load partitioning between ferrite and cementite during elasto-plastic deformation of an ultrahigh-carbon steel." *Acta Materialia* **55**(6): 1999-2011.

Young, M. L., DeFouw, J., Almer, J. D. and Dunand, D. C. (2007b). "Load partitioning during compressive loading of a Mg/MgB_2 composite." *Acta Materialia* **55**(10): 3467-3478.

Zgrablich, G., Mendioroz, S., Daza, L., Pajares, J., Mayagoitia, V., Rojas, F. and Conner, W. C. (1991). "Effect of porous structure on the determination of pore-size distribution by mercury porosimetry and nitrogen sorption." *Langmuir* **7**(4): 779-785.

Zollfrank, C. and Sieber, H. (2005). "Microstructure evolution and reaction mechanism of biomorphous SiSiC ceramics." *Journal of the American Ceramic Society* **88**(1): 51-58.

Zulfia, A. and Hand, R. J. (2002). "The production of Al-Mg alloy/SiC metal matrix composites by pressureless infiltration." *Journal of Materials Science* **37**(5): 955-961.

Zweben, C. (1992). "Metal-matrix composites for electronic packaging." *JOM-Journal of the Minerals Metals & Materials Society* **44**(7): 15-23.

Zweben, C. (1998). "Advances in composite materials for thermal management in electronic packaging." *JOM-Journal of the Minerals Metals & Materials Society* **50**(6): 47-51.

Appendix A: Aluminum/Silicon Carbide Composites: Internal Friction

Background

The ability of a material to dissipate, or dampen, strain energy is quantified as the material's internal friction (McGonnagle 1968). Several mechanisms can contribute to internal friction including the motion of point defects and dislocations. A common way of measuring the internal friction of a material is to measure the attenuation of ultrasonic waves. The energy of a vibration in an oscillating system, E_v, is proportional to the square of the amplitude of the wave, A.

$$E_v \propto A^2 \tag{A.1}$$

As a material dampens the energy, due to internal friction mechanisms, the fractional energy loss per cycle is

$$\frac{\Delta E_v}{E_v} = \frac{A_2^2 - A_1^2}{A_1^2} \tag{A.2}$$

where A_1 and A_2 are two successive vibration amplitudes. This is commonly referred to as the specific damping capacity of a material. A more commonly reported measure of internal friction is the logarithmic decrement, δ, which is the natural logarithm of the ratio of successive amplitudes of oscillatory vibrations,

$$\delta = \ln \frac{A_1}{A_2} \tag{A.3}$$

which, for small amounts of damping is half of the specific damping capacity.

Internal friction represents the anelasticity of a material, i.e. it is the imaginary and time-dependent component of a material's elastic stiffness. When a stress is suddenly

applied to a material, the elastic strain component develops instantaneously, but the anelastic component lags behind. In an oscillating system, the tangent of the phase angle, α, by which the strain lags behind the stress is an indication of the energy loss and is related to the internal friction of the system:

$$\tan\alpha = \frac{1}{\pi}\ln\frac{A_1}{A_2} = \frac{\delta}{\pi} = Q^{-1} \tag{A.4}$$

where Q^{-1} is the internal friction.

Dynamic tests are the most widely used techniques for measuring internal friction. In one method, a composite oscillator is used to measure the energy loss in a specimen that is subjected to an alternating stress, which is produced by the piezoelectric excitation of longitudinal waves. The structure of a typical composite oscillator is shown in Figure A.1 (Kustov *et al.* 2006). The specimen, usually a rectangular bar, is attached to two quartz transducers that serve to either excite the system to a resonance frequency or gauge the elastic strain of the system. The combination of the two transducers and a feedback loop is used to maintain continuous resonant oscillations. The internal friction, Q^{-1}, of the composite oscillator and the value of the strain amplitude of the i^{th} element, $\varepsilon_{11}^{max}(i)$ can be calculated based on the voltages across the drive and gauge transducers, U_d and U_g, respectively,

$$Q^{-1} = K_\delta \frac{U_d}{U_g} \tag{A.5i}$$

$$\varepsilon_{11}^{max}(i)\lambda(i) = K_\varepsilon U_g \tag{A.5ii}$$

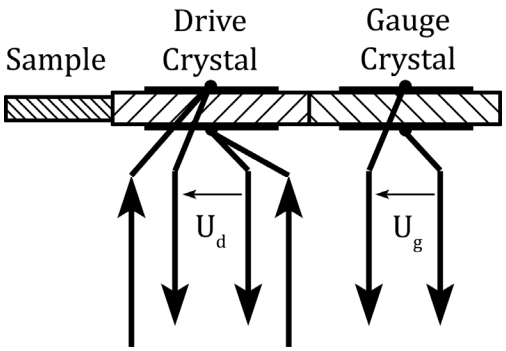

Figure A.1. Schematic of a three-component composite oscillator used to measure the internal friction of materials. The two quartz transducers are used to drive and gauge the resonance frequency and elastic strain of the system (after Kustov *et al.* 2006).

where $\lambda(i)$ is the wavelength in component i, and K_δ and K_ε are coefficients depending on the geometry and fundamental characteristics (elastic compliance and piezoelectric modulus) of the transducers and the impedance of the electrical circuit.

The internal friction and resonant frequency of the specimen can be deconvoluted based on previous knowledge of the mass, resonant frequency and Q^{-1} of the transducers:

$$m(t)\omega(t)^2 = \sum_i m(i)\omega(i)^2 \tag{A.6i}$$

$$m(t)Q^{-1}(t) = \sum_i m(i)Q^{-1}(i) \tag{A.6ii}$$

where $m(t)$ and $\omega(t)$ are the total mass and angular resonant frequency of the composite oscillator, and $m(i)$, $\omega(i)$ and $Q^{-1}(i)$ are the mass, resonant frequency, and internal friction of the i^{th} component. The resonant frequency of the specimen can be used to calculate the elastic modulus, E, according to

$$E = \frac{\rho\omega^2 l^2}{\pi} \tag{A.7}$$

where ρ and l are the sample density and length, respectively. The internal friction is typically measured as a function of the energy introduced into the material via changes in temperature or strain amplitude.

In the case of metal/ceramic composite materials, Q^{-1} is affected by the microstructure at the metal/ceramic interface, where dislocations can originate due to thermal mismatch (Durieux *et al.* 1997; Calhoun *et al.* 2000). The increased dislocation density, when compared to the constituent materials, can result in a greater internal friction. As such, this makes composite materials suitable for applications where mechanical vibrations can cause structural instabilities and where energy absorbers are currently used (Lavernia *et*

al. 1995). In addition to the effects of temperature (Girard et al. 1993; Vincent et al. 1993) and strain amplitude (Kustov et al. 1997; Kustov et al. 1999), the internal friction of a composite material can also be affected by the morphology (Ledbetter *et al.* 1986; Couteau *et al.* 2004) and volume fraction (Parrini *et al.* 1996a, 1996b) of the reinforcement phase.

Experimental Methods

The logarithmic decrement, δ, and elastic modulus, E, of the Al-Si-Mg alloy, and the beech and sapele Al/SiC MCCs were measured by Tatiana S. Orlova and colleagues at the A.F. Ioffe Physico-Technical Institute (St. Petersburg, Russia) using the composite oscillator technique on LO and TR specimens measuring 3.0 x 3.0 x 35 mm^3 (Kustov et al. 2006). Longitudinal vibrations were excited along the length of the bars at a frequency of ≈ 100 kHz at room temperature, and δ and E were measured as a function of increasing and decreasing strain amplitude ($\varepsilon \approx 10^{-6}$ to 10^{-4}). One sample of each material was tested, and one amplitude cycle was measured for each experiment.

Results

Figures A2 through A6 plot the modulus, E, and logarithmic decrement, δ, of the Al-Si-Mg alloy, BE-LO, BE-TR, SA-LO, and SA-TR samples, respectively, and arrows in the figures indicate the sequence of increasing and then decreasing strain amplitude. The moduli of the materials were in general agreement with those reported in Chapter 4, except for the BE-LO specimen, which was significantly stiffer than the samples measured in flexure. A wide range of the vibration strain amplitude was studied and results indicated both linear

(amplitude independent) and non-linear (microplastic) regions in the plots of δ versus ε. The logarithmic decrement of the transverse MCCs was greater than that of the LO-MCCs and exhibited more hysteresis in the amplitude cycle.

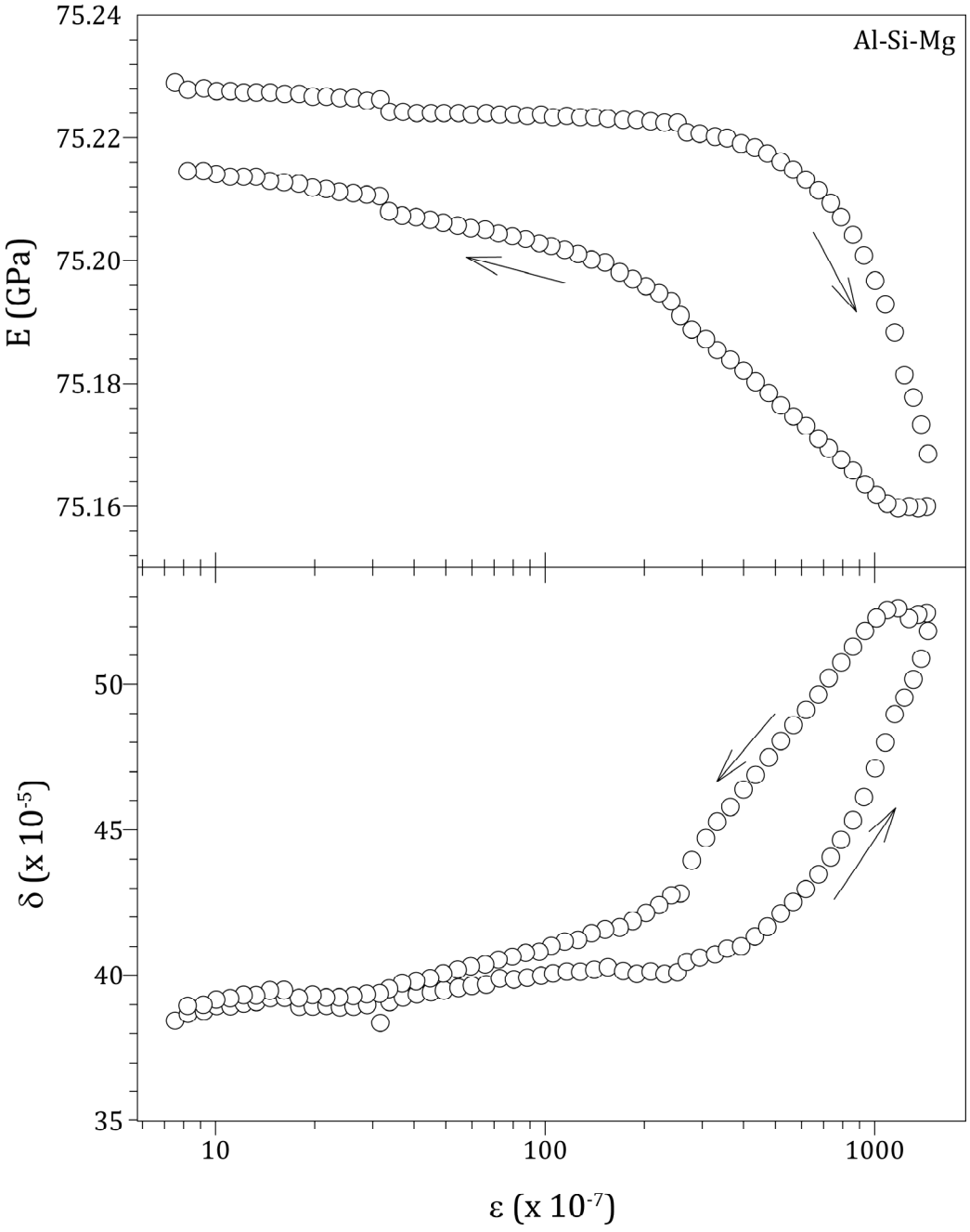

Figure A.2. Elastic modulus, E, and logarithmic decrement, δ, of the Al-Si-Mg bulk alloy versus strain amplitude, ε. The arrows indicate the increasing and then decreasing sequence in ε.

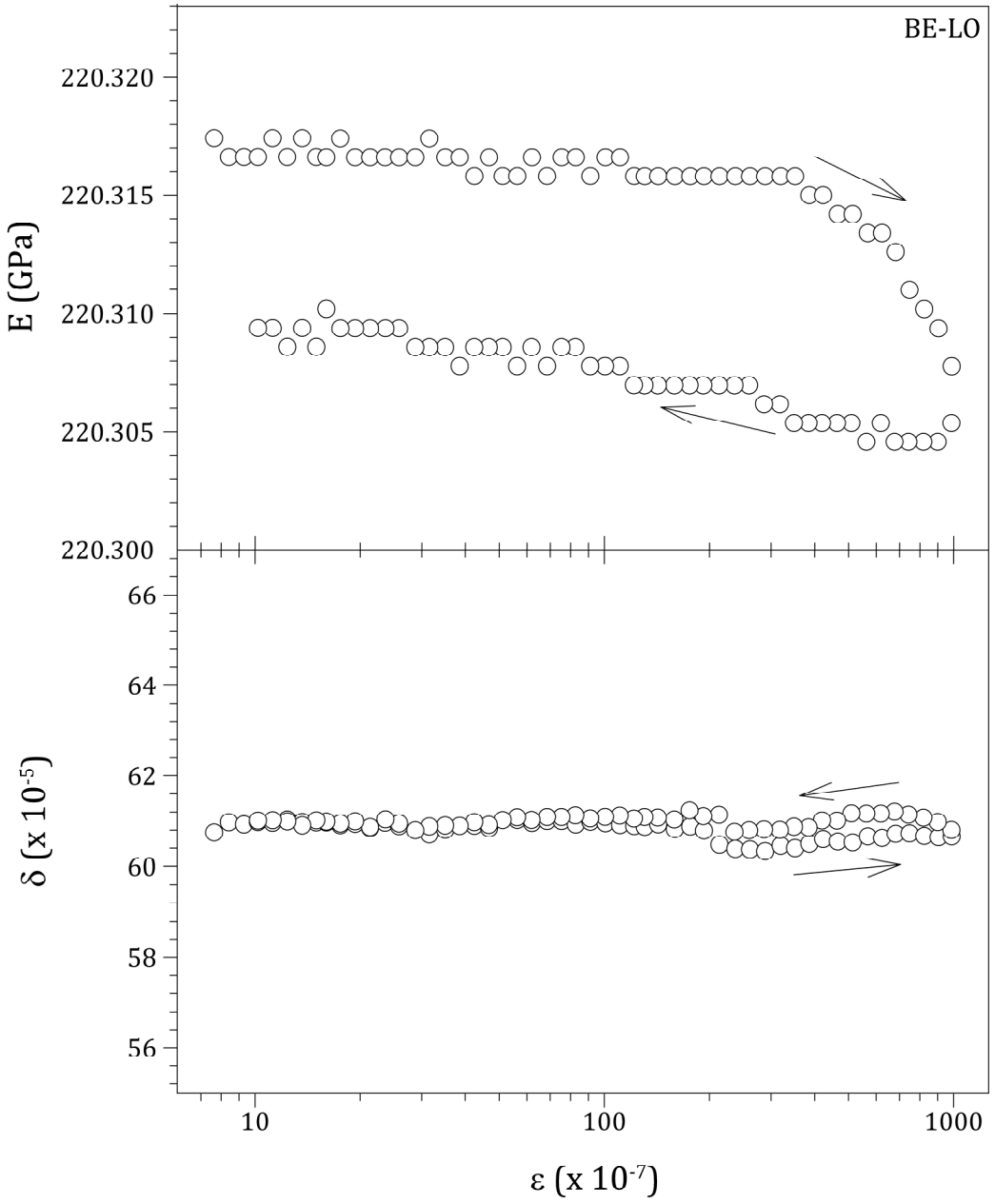

Figure A.3. Elastic modulus, E, and logarithmic decrement, δ, of the BE-LO composite versus strain amplitude, ε. The arrows indicate the increasing and then decreasing sequence in ε.

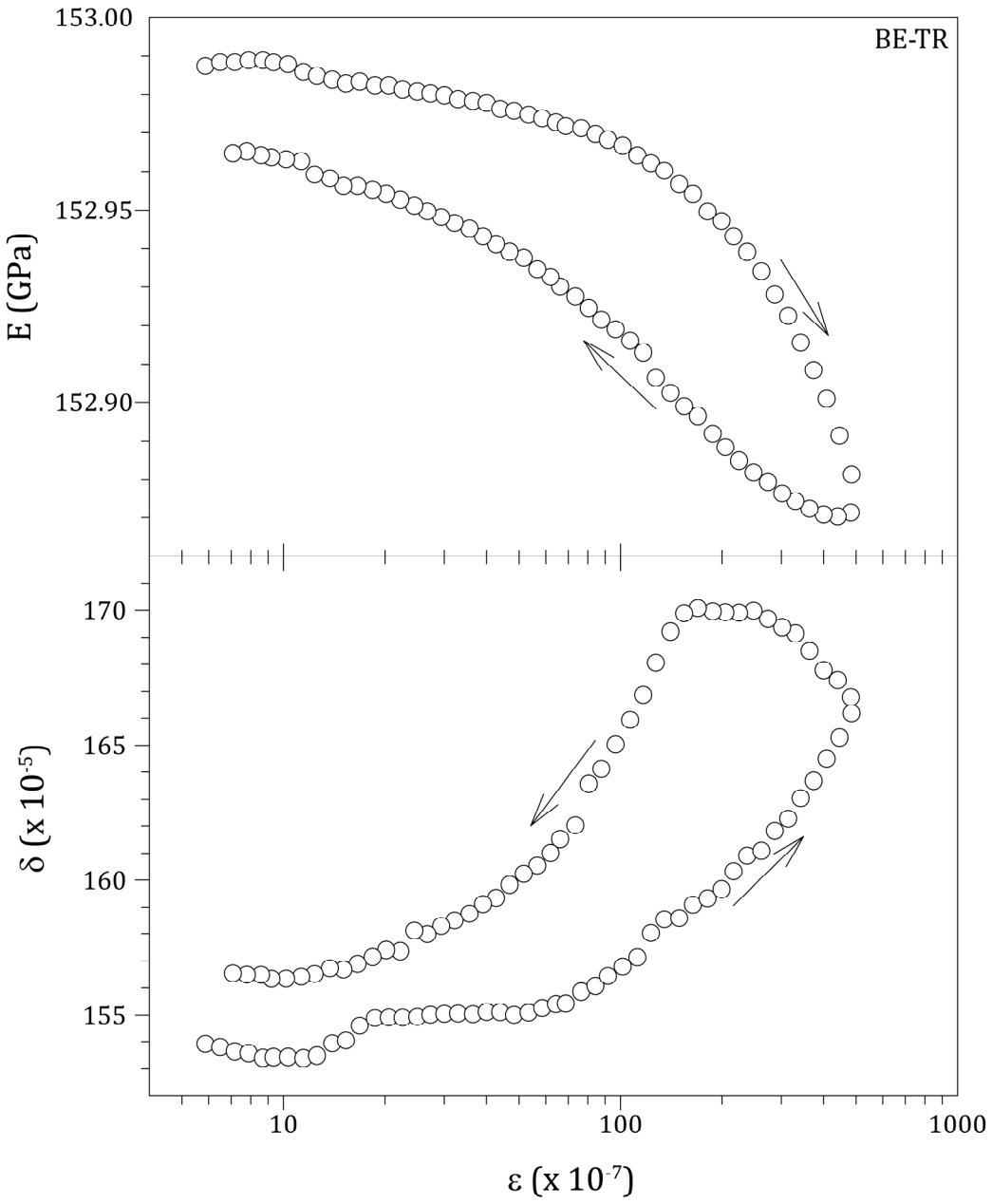

Figure A.4. Elastic modulus, E, and logarithmic decrement, δ, of the BE-TR composite versus strain amplitude, ε. The arrows indicate the increasing and then decreasing sequence in ε.

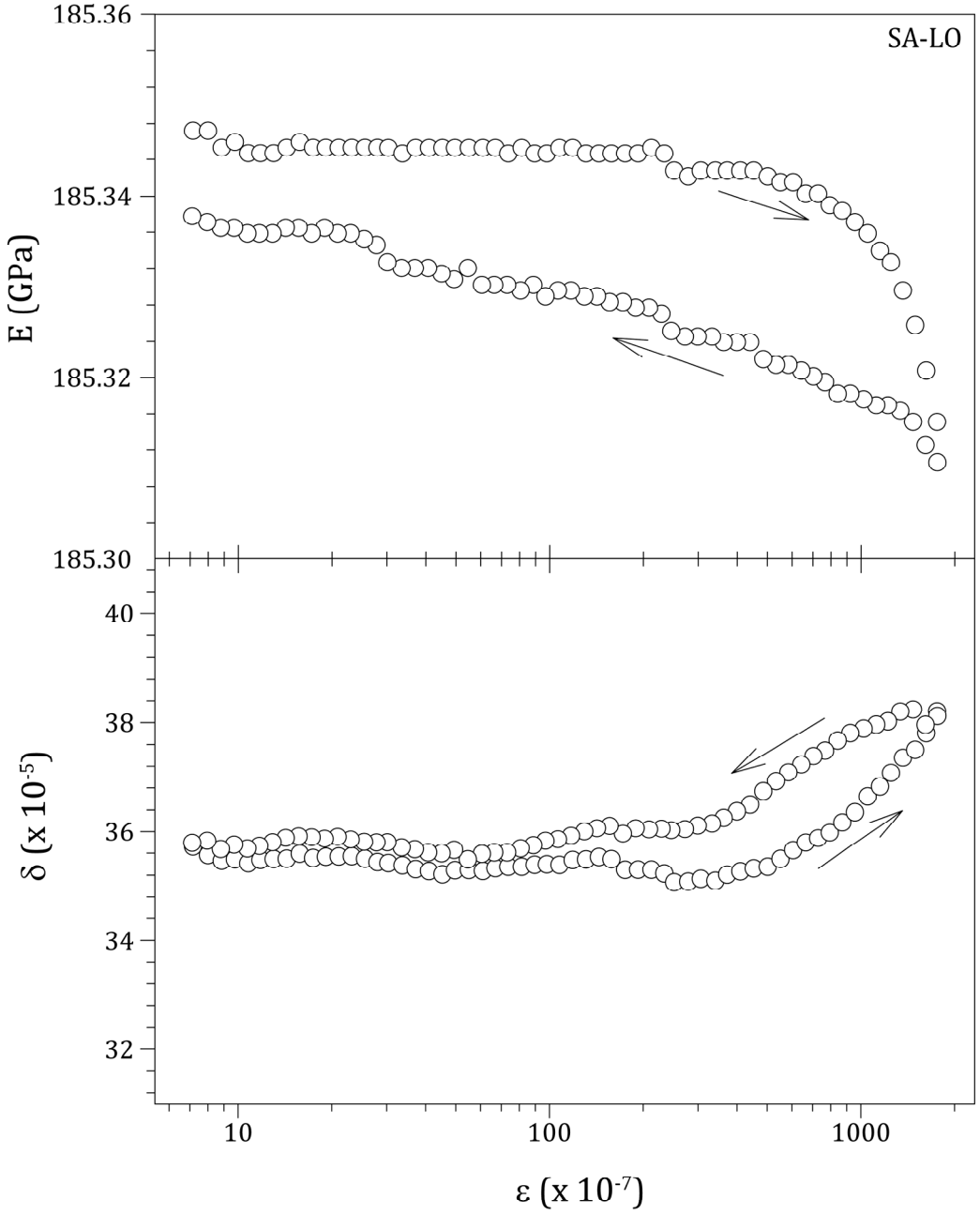

Figure A.5. Elastic modulus, E, and logarithmic decrement, δ, of the SA-LO composite versus strain amplitude, ε. The arrows indicate the increasing and then decreasing sequence in ε.

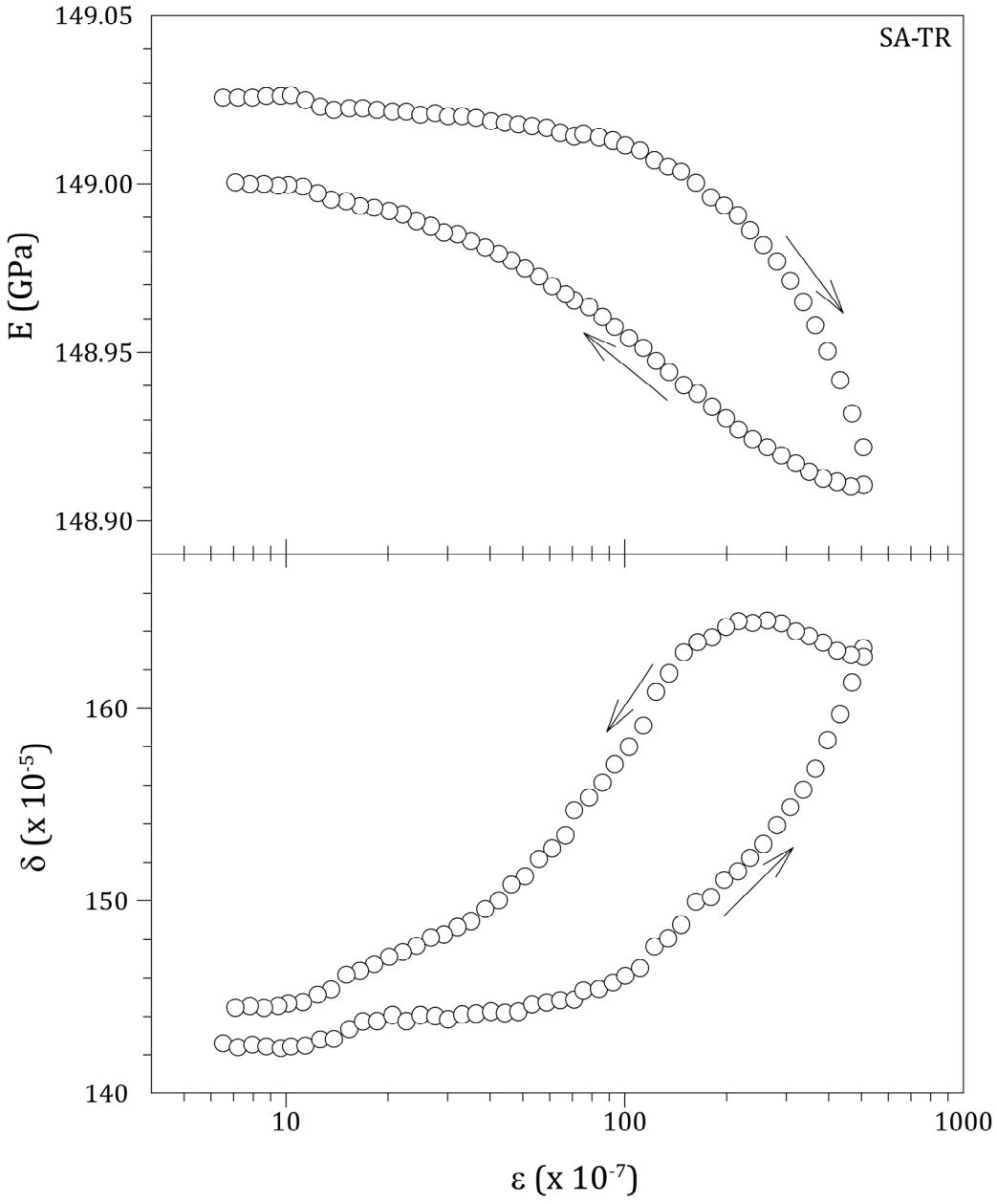

Figure A.6. Elastic modulus, E, and logarithmic decrement, δ, of the SA-TR composite versus strain amplitude, ε. The arrows indicate the increasing and then decreasing sequence in ε.

Discussion

There is a clear dependence of δ on orientation as both TR samples dampen the ultrasonic oscillations more so than the LO samples. This is due to greater dislocation activity when the induced strain is acting in the transverse orientation (Couteau *et al.* 2004), which results in more dislocation mobility. While increases in δ indicate dislocation mobility, the hysteresis in Figure A2, A4 and A6 indicates dislocation multiplication (Kustov *et al.* 1999). The near-constant nature of δ in Figures A3 and A5 indicate a lack of dislocation mobility parallel to the Al/SiC interface. This could result from dislocation tangles, which are often found in metal/ceramic composites with irregularly-shaped reinforcements (Calhoun *et al.* 2000), e.g. the rough polycrystalline wood-derived SiC.

The damping capacity of the beech samples was greater than that of the SA-MCCs in each orientation. The size of the microplastic region in metal/ceramic composites is a function of the reinforcement size (Taya *et al.* 1987). For equiaxed SiC particles in Al, the size of the plastic zone, according to Taya and Mori, will be ≈ 2-3 times the particle radius and will decrease with increasing reinforcement aspect ratio. In the BE- and SA-MCCs, the SiC pore walls resemble agglomerations of SiC particles with radii ranging from about 1 μm to 5 μm, which would result in any Al-filled pores less than 30 μm in diameter having a homogeneous distribution of dislocation tangles. This would effectively eliminate dislocation motion contributions to the internal friction from approximately 50% and 70% of the Al-filled porosity in the BE- and SA-MCCs (Figure 3.2), respectively, and result in lower decrements for the SA-MCCs.

Curiously, the BE-LO sample had a higher damping capacity than the Al-Si-Mg alloy, while the SA-LO damping capacity was lower than the Al-alloy. Unfortunately, a direct comparison of the internal friction is difficult as the microstructure of the aluminum alloy, most notably the Si and Mg_2Si precipitate structure, can also affect the internal friction (Do Lee 2005). The larger precipitates in the bulk Al-alloy (Figure 3.9) and the presumably lower dislocation density (due to the absence of the SiC reinforcement) will lead to a different damping behavior when compared to the composite materials, which have a greater number-density of smaller precipitates and a larger dislocation density.

Summary & Future Work

The internal friction and elastic moduli of the composite materials and bulk Al-alloy were measured using a dynamic composite oscillator. In general, the moduli agreed with those measured in flexure, the damping capacity of the composites was greater in the transverse orientation, and the damping capacity of the BE-MCCs was greater than the SA-MCCs.

Future studies should repeat the current work to verify the above results. In addition, the internal friction should be measured as a function of temperature. Also, transmission electron microscopy, or other dislocation observation techniques, should be used to study the dislocation density and size of the microplastic zone in both the bulk Al-Si-Mg alloy and the composites.

References

Calhoun, R. B. and Dunand, D. C. (2000). Dislocations in Metal Matrix Composites. Comprehensive Composite Materials. Oxford, Pergamon.

Couteau, O. and Schaller, R. (2004). "Effect of the fiber orientation on the transient damping in metal matrix composites." *Materials Science and Engineering A - Structural Materials: Properties, Microstructure and Processing* **387-89**: 862-866.

Do Lee, C. (2005). "Damping properties on age hardening of Al-7Si-0.3Mg alloy during T6 treatment." *Materials Science and Engineering A - Structural Materials: Properties, Microstructure and Processing* **394**(1-2): 112-116.

Durieux, S., Esnouf, C., Maire, E., Fondere, J. P., Fougeres, R., Lormand, G. and Vincent, A. (1997). "On internal damping in metal matrix composites: role of particle-matrix interfacial region." *Scripta Materialia* **36**(2): 189-193.

Kustov, S., Golyandin, S., Ichino, A. and Gremaud, G. (2006). "A new design of automated piezoelectric composite oscillator technique." *Materials Science and Engineering A - Structural Materials: Properties, Microstructure and Processing* **442**(1-2): 532-537.

Kustov, S., Gremaud, G., Benoit, W., Golyandin, S., Sapozhnikov, K., Nishino, Y. and Asano, S. (1999). "Strain amplitude-dependent anelasticity in Cu-Ni solid solution due to thermally activated and athermal dislocation-point obstacle interactions." *Journal of Applied Physics* **85**(3): 1444-1459.

Lavernia, E. J., Zhang, J. and Perez, R. J. (1995). "Damping behavior and mechanisms in particulate reinforced metal matrix composites processed using spray atomization and deposition." *Key Engineering Materials* **104-107**: 691-728.

Ledbetter, H. M., Lei, M. and Austin, M. W. (1986). "Young modulus and internal friction of a fiber-reinforced composite." *Journal of Applied Physics* **59**(6): 1972-1976.

McGonnagle, W. J. (1968). Nondestructive Testing. Philadelphia, Gordon and Breach Science Publishers.

Parrini, L. and Schaller, R. (1996a). "Characterization of mechanical stresses in metal matrix composites by internal friction." *Acta Materialia* **44**(10): 3895-3903.

Parrini, L. and Schaller, R. (1996b). "Thermal stresses in metal matrix composites studied by internal friction." *Acta Materialia* **44**(12): 4881-4888.

Taya, M. and Mori, T. (1987). "Dislocations punched-out around a short fiber in a short fiber metal matrix composite subjected to uniform temperature change." *Acta Metallurgica* **35**(1): 155-162.